이학박사학위논문

Study of Double Spin Asymmetries in Inclusive ep Scattering at Jefferson Lab

제퍼슨 연구소에서의 포괄적 전자-양성자 산란을 이용한 이중 스핀 비대칭성 연구

2014년 8월

서울대학교 대학원

물리천문학부

강 호 영

Study of Double Spin Asymmetries in Inclusive ep Scattering at Jefferson Lab

제퍼슨 연구소에서의 포괄적 전자-양성자 산란을 이용한 이중 스핀 비대칭성 연구

지도교수 최 선 호

이 논문을 이학박사학위논문으로 제출함
2014년 8월

서울대학교 대학원
물리천문학부
강 호 영

강호영의 이학박사학위논문을 인준함
2014년 8월

위 원 장	김 수 봉	(인)
부 위 원 장	최 선 호	(인)
위 원	김 형 도	(인)
위 원	양 운 기	(인)
위 원	천 명 기	(인)

Study of Double Spin Asymmetries in Inclusive ep Scattering at Jefferson Lab

by

Hoyoung Kang

Supervised by

Seonho Choi

A Dissertation Submitted to the Faculty of
Seoul National University
in Partial Fulfillment of the Requirements for
the Degree of Doctor of Philosophy

August 2014

Department of Physics and Astronomy
Graduate School
Seoul National University

Abstract

Study of Double Spin Asymmetries in Inclusive ep Scattering at Jefferson Lab

Hoyoung Kang
Department of Physics and Astronomy
The Graduate School
Seoul National University

The spin structure of the proton has been investigated in the high Bjorken x and low momentum transfer Q^2 region. We used Jefferson Lab's polarized electron beam, a polarized target, and a spectrometer to get both the parallel and perpendicular spin asymmetries $A_{\parallel}$ and $A_{\perp}$. These asymmetries produced the physics asymmetries A_1 and A_2 and spin structure functions g_1 and g_2. We found Q^2 dependences of the asymmetries at resonance region and higher-twist effects. Our result increases the available data on the proton spin structure, especially at resonance region with low Q^2. Moreover, A_2 and g_2 data show clear Q^2 evolution, comparing with RSS and SANE-BETA. Negative resonance in A_2 data needs to be examined by theory. It can be an indication of very negative transverse-longitudinal interference contribution at $W \approx 1.3GeV$. Higher twist

effect appears at the low Q^2 of $1.9GeV^2$, although it is less significant than lower Q^2 data of RSS. Twist-3 matrix element d_2 was calculated using our asymmetry fits evaluated at $Q^2 = 1.9GeV^2$. $\bar{d_2} = -0.0087 \pm 0.0014$ was obtained by integrating $0.47 \leq x \leq 0.87$.

Keywords : Double Spin Asymmetry, Proton Spin Structure, Operator Product Expansion, Nucleon Resonance, Electron-Proton Scattering, Jefferson Lab
Student Number : 2006-20313

Contents

List of Figures

List of Tables

Chapter 1

Introduction

Since our quest of the universe has begun in ancient Greek, the understanding of fundamental particles of the universe has been the main focus of this quest. Although the atom, as its name's origin of atomism of Democritus at the 5th century BC, was once regarded as the fundamental particle, it has been found that atom consists of electrons and nucleus. And the nucleus can also be decomposed into protons and neutrons. Lord Rutherford's discovery of the nucleus made the scattering experiment one of the most profound way to probe basic particles. Many scientists followed this way, and theories and experiments together have built firm understanding of the nucleus.

The Standard Model of particle physics is the main victory of this journey. It classifies the fundamental particles into quarks, leptons, gauge bosons, and Higgs boson. Especially, quarks and gluons, gauge bosons governing strong interaction, form protons and neutrons, and every other mesons and baryons. All the ordinary matters around us consists of electrons, protons, and neutrons. Since they are very stable, proton and neutron can be easy material to investigate the interaction of quarks and gluons. Although the confinement prevents

the observation of the individual quarks, they can be studied via scattering experiments. Experiments at the Stanford linear accelerator (SLAC) in the late 1960s have shown strong evidence of hard point-like particles in the nucleons. They measured the scattering cross section of electrons scatterd off proton and deuterium, and found a structure functions, which rule this deep inelastic scattering (DIS). In 1969, James Bjorken predicted the scaling behaviour of the structure functions. It was Richard Feynman who made the insightful picture of quark-parton model, to understand this scaling behaviour. These efforts have established theory of quarks and their behaviour inside nucleons. And lepton-nucleon scattering has become a key tool to investigate the structure of nucleon.

One of the interesting intrinsic properties is the spin of a particle. Although the naïve parton model suggested that valence quarks should carry most of the proton's spin, EMC experiments found that most of the proton's spin is not carried by them [26]. It sparked an intensive study of nucleon spin structure [20, 27–29].

The experiment studied in this thesis is also a lepton-nucleon scattering experiment. The experiment, TJNAF E07-003, carried out an inclusive electron-proton scattering experiment, at Thomas Jefferson National Accelerator Facility, or Jefferson Lab (JLab). It is named SANE - Spin Asymmetries of the Nucleon Experiment. As its name stands for, it investigates the spin structure of the nucleon, especially using proton and electron. This is another effort to understand the proton's spin structure. The experiment measured the ep scattering cross sections for various spin configurations of the beam and target, which can be quantitatively described by spin asymmetries. Spin structure functions can be deduced from the spin asymmetries. In this thesis, the motivations, the experimental apparatus, and the results of SANE will be explained.

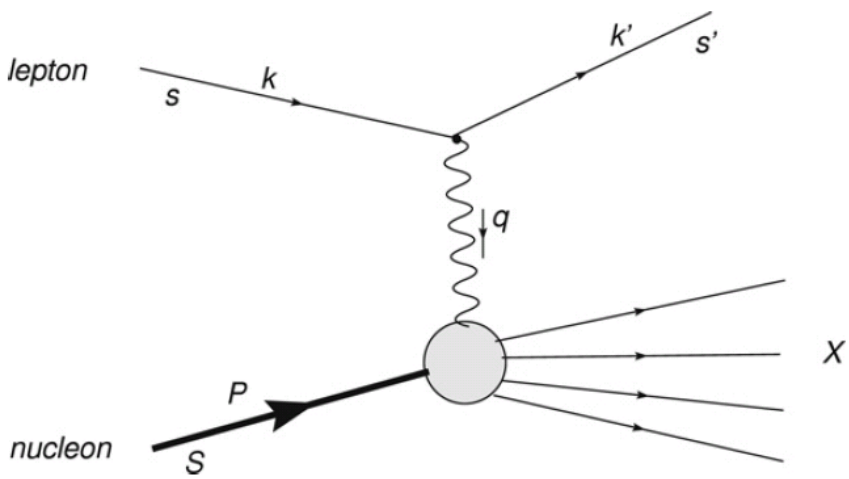

Figure 1.1: Feynman diagram of inelastic lepton-nucleon scattering [1]

1.1 Structure Functions and Asymmetries

High energy lepton-nucleon scattering can be described by the quark-parton model. General formalism can be found in standard textbooks and reviews. In this thesis, Anselmino, Efremov, and Leader's review [24] is used as a standard formalism. The inelastic scattering of polarized leptons off polarized nucleons can be described in the framework as in Fig. 1.1. We denote by m the lepton's mass, k (k') the initial (final) lepton's 4-momentum, s (s') the initial (final) its spin 4-vector, and $q = k - k'$ as the 4-momentum transfer of lepton on nucleon. P and S are initial nucleon's 4-momentum and spin 4-vector respectively. And X describes recoiled system, which is not measured directly in inclusive exper-

iments. In laboratory frame, $P = (M, \mathbf{0})$, $k = (E, \boldsymbol{k})$, $k' = (E', \boldsymbol{k'})$, as proton of rest mass M recoils by the lepton of mass m. If we assume one photon exchange, or Born level approach, the differential cross section for detecting the final lepton in the solid angle $d\Omega$ and in the energy range of $(E', E' + dE')$ can be written as:

$$\frac{d^2\sigma}{d\Omega E'} = \frac{\alpha^2}{2Mq^4}\frac{E'}{E}L_{\mu\nu}W^{\mu\nu}, \tag{1.1}$$

where α is the fine structure constant, $L_{\mu\nu}$ the leptonic tensor, and $W_{\mu\nu}$ the hadronic tensor. In Eq. (1.1), the leptonic tensor, if we sum over unobserved final lepton spin, can be written as

$$L_{\mu\nu}(k, s; k') = \sum_{s'}[\bar{u}(k', s')\gamma_\mu u(k, s)]^*[\bar{u}(k', s')\gamma_\nu u(k, s)], \tag{1.2}$$

and it can be split into symmetric $L^{(S)}_{\mu\nu}(k; k')$ and antisymmetric $L^{(A)}_{\mu\nu}(k, s; k')$ parts, i.e. $L_{\mu\nu} = 2\{L^{(S)}_{\mu\nu} + iL^{(A)}_{\mu\nu}\}$, where

$$L^{(S)}_{\mu\nu}(k; k') = k_\mu k'_\nu + k'_\mu k_\nu - g_{\mu\nu}(k \cdot k' - m^2) \tag{1.3}$$

$$L^{(A)}_{\mu\nu}(k, s; k') = m\epsilon_{\mu\nu\alpha\beta}s^\alpha q^\beta. \tag{1.4}$$

The hadronic tensor, which describes the interaction between the virtual photon and the nucleon, can be described by four structure functions. The structure functions are the unknown parts of this interaction. They are the unpolarized structure functions F_1 and F_2 and polarized ones g_1 and g_2. They can be measured experimentally or studied theoretically, as they are governed by quantum chromodynamics (QCD). With the similar method as the leptonic tensor, the hadronic tensor can be expressed by symmetric and antisymmetric parts:

$$W_{\mu\nu}(q; P, S) = W^{(S)}_{\mu\nu}(q; P) + iW^{(A)}_{\mu\nu}(q; P, S). \tag{1.5}$$

It is a usual way to define the structure functions as scalar coefficients of the hadronic tensor:

$$\begin{aligned} W_{\mu\nu}^{(S)}(q;P) &= 2[\frac{q_\mu q_\nu}{q^2} - g_{\mu\nu}]F_1(x,Q^2) \\ &+ \frac{2}{M\nu}[P_\mu - \frac{P\cdot q}{q^2}q_\mu][P_\nu - \frac{P\cdot q}{q^2}q_\nu]F_2(x,Q^2) \end{aligned} \tag{1.6}$$

$$\begin{aligned} W_{\mu\nu}^{(A)}(q;P,S) &= \frac{2M}{P\cdot q}\epsilon_{\mu\nu\alpha\beta}q^\alpha \\ &\{S^\beta g_1(x,Q^2) + [S^\beta - \frac{(S\cdot q)P^\beta}{P\cdot q}]g_2(x,Q^2)\}, \end{aligned} \tag{1.7}$$

where $Q^2 \equiv -q^2$, $\nu \equiv E - E'$, and x is Bjorken x, such that $x \equiv \frac{Q^2}{2q\cdot P} = \frac{Q^2}{2M\nu}$. In this sense, the differential cross section can be expressed by four structure functions. The unpolarized cross section is proportional to $L_{\mu\nu}^{(S)}W^{\mu\nu(S)}$, so F_1 and F_2 rule it. And differences of cross sections with opposite nucleon spins are proportional to $L_{\mu\nu}^{(A)}W^{\mu\nu(A)}$, so g_1 and g_2 drives it.

Although measuring spin dependent cross section produces better results than just measuring asymmetry, as polarized structure functions have measured and established well, it is sometimes convenient to divide the polarized cross section difference by the unpolarized cross section, to produce spin asymmetry. The reason is that experimental results can reduce systematic uncertainties, and that it is easier to get the asymmetries than the cross section directly. According to the relative directions of lepton and nucleon spins, parallel and perpendicular asymmetries can be defined. When $\rightarrow$ is the lepton spin direction and $\Rightarrow$ the nucleon spin direction, their relative directions can be either parallel and anti-parallel, or right-handed and left-handed perpendicular:

$$A_\parallel = \frac{d\sigma^{\rightarrow\Rightarrow} - d\sigma^{\rightarrow\Leftarrow}}{2d\sigma_{unpolarized}} \tag{1.8}$$

$$A_\perp = \frac{d\sigma^{\rightarrow\Uparrow} - d\sigma^{\rightarrow\Downarrow}}{2d\sigma_{unpolarized}}. \tag{1.9}$$

It is useful to introduce virtual photon absorption asymmetries A_1 and A_2. They are sometimes called physics asymmetries. Relation between (g_1, g_2) and (A_1, A_2) is straightforward,

$$A_1 = \frac{g_1 - \gamma^2 g_2}{F_1} \tag{1.10}$$

$$A_2 = \gamma \frac{g_1 + g_2}{F_1}, \tag{1.11}$$

where

$$\gamma = \frac{2Mx}{\sqrt{Q^2}}. \tag{1.12}$$

The physics asymmetries can be related to $A_\parallel$ and $A_\perp$ with some kinematic factors:

$$A_\parallel = D(A_1 + \eta A_2) \tag{1.13}$$

$$A_\perp = d(A_2 - \zeta A_1) \tag{1.14}$$

where

$$D = \frac{1 - E'\epsilon/E}{1 + \epsilon R} \tag{1.15}$$

$$\eta = \frac{\epsilon\sqrt{Q^2}}{E - E'\epsilon} \tag{1.16}$$

$$d = D\sqrt{\frac{2\epsilon}{1+\epsilon}} \tag{1.17}$$

$$\zeta = \frac{\eta(1+\epsilon)}{2\epsilon}, \tag{1.18}$$

and

$$R(x, Q^2) = (1 + \gamma^2)\frac{F_2(x, Q^2)}{2xF_1(x, Q^2)} - 1 \tag{1.19}$$

$$\epsilon = \frac{1}{1 + 2[1 + \gamma^{-2}]\tan^2(\theta/2)}. \tag{1.20}$$

Of course, it is also possible to make reverse formulae:

$$A_1 = \frac{1}{1+\eta\zeta}(\frac{1}{D}A_{\parallel} - \frac{\eta}{d}A_{\perp}) \tag{1.21}$$

$$A_2 = \frac{1}{1+\eta}(\frac{\zeta}{D}A_{\parallel} + \frac{1}{d}A_{\perp}). \tag{1.22}$$

For the polarized cross section can have any lepton spin direction, two variables g_1 and g_2 can be measured by any two independent observables. But the perpendicular asymmetry is generally smaller than parallel one, because of kinematic factors. So, many experiments focused on parallel asymmetry measurement. This practical approach is justified by restrictive bound on A_2 [1, 30]:

$$|A_2| \leq \sqrt{R(1+A_1)/2}. \tag{1.23}$$

Solving g_2 in terms of g_1 and A_2 in (1.10) and (1.11) and putting it into (1.13),

$$\frac{A_{\parallel}}{D} = A_1 + \eta A_2 = \frac{g_1}{F_1} - \gamma^2\frac{g_2}{F_1} + \eta A_2 \tag{1.24}$$

Because ηA_2 and $\gamma^2 g_2$ are typically small, a practical approximation is given by

$$A_1 + \eta A_2 \approx \frac{A_{\parallel}}{D} \approx \frac{g_1}{F_1}. \tag{1.25}$$

However, if we want to know g_2 and A_2 information, the above approximation is not enough. This experiment SANE is concentrated on g_2 and A_2, by measuring both parallel and perpendicular asymmetries (near-perpendicular asymmetry is chosen for practical reason). They are expected to show higher twist effects, at low Q^2 region.

1.2 Spin Structure

In DIS, the interaction between photon and quark (parton) can be illustrated as in Fig. 1.2. The lepton-nucleon interaction in DIS is interpreted as lepton-quark

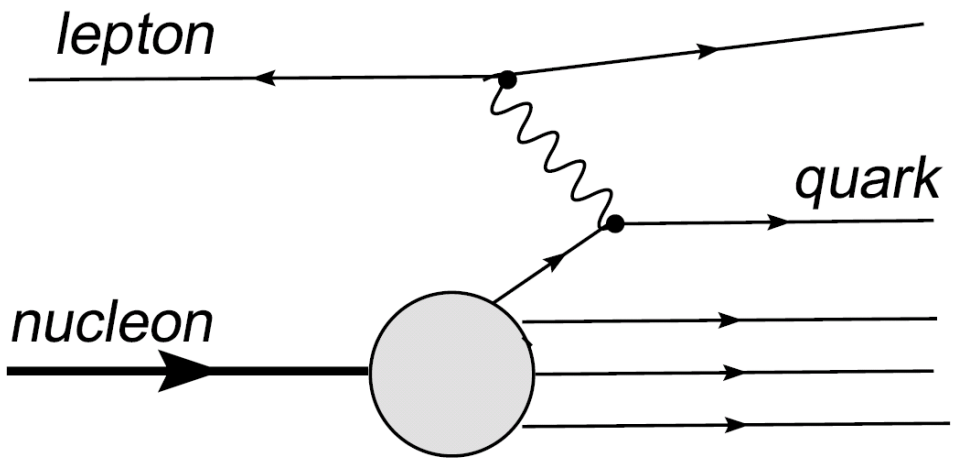

Figure 1.2: Parton model description of deep inelastic scattering [1]

scattering, which is described by the structure functions. If the final quark is on mass shell, or $(p+q)^2 = 0$, Bjorken x means the the struck quark's portion of the momentum, such that the quark has momentum of xP.

When we follow naïve quark-parton model, that the nucleon is composed of quarks without orbital angular momentum and that the gluon has no polarization, the unpolarized structure function F_1 and polarized g_1 can be interpreted as

$$F_1(x) = \frac{1}{2}\sum_i e_i^2[q_i^{\uparrow}(x) + q_i^{\downarrow}(x)] \tag{1.26}$$

$$g_1(x) = \frac{1}{2}\sum_i e_i^2[q_i^{\uparrow}(x) - q_i^{\downarrow}(x)] = \frac{1}{2}\sum_i e_i^2 \Delta q_i(x), \tag{1.27}$$

where e_i^2 is the charge of each (flavoured) quark, $q_i^{\uparrow(\downarrow)}(x)$ is the quark (including anti-quark) momentum distribution with quark helicities parallel ($\uparrow$) and anti-parallel ($\downarrow$) to the longitudinally polarized ($\Uparrow$) nucleon. So, structure functions

can be interpreted as the charge square weighted momentum distribution of quarks. In this notation, $\int_0^1 \Delta q_i(x)dx = \Delta q(x)$, which is the total helicity of quark flavor i in the nucleon. And $\Delta\Sigma = \sum_i \Delta q_i = \Delta u + \Delta d + \Delta s$ is the net helicity of quarks. If we believe the assumption of naïve parton model, $\frac{1}{2}\Delta\Sigma$ should be $\frac{1}{2}$, which is the total spin of the nucleon. As EMC experiment has shown that it is not true [26], this interpretation has been modified.

g_2 is rather hard to understand. Historically, Feynman related $g_T(x) = g_1(x) + g_2(x) = A_2 F_1/\gamma$ to the distribution of quarks with transversely polarized nucleon.

$$g_T(x) = \sum_i e_i^2 \frac{m_q}{2xM}[k_i^{\uparrow}(x) - k_i^{\downarrow}(x)], \tag{1.28}$$

where m_q is the quark mass, and $k_i^{\uparrow(\downarrow)}(x)$ is momentum distribution of quark polarized parallel ($\uparrow$) and anti-parallel ($\downarrow$) to transversely polarized proton [31, 32]. But Eq. (1.28) has been turned out to be incorrect, and actually right hand side of this equation represents the twist-2 structure function h_T [33]. For the naïve parton model does not include transverse momentum, quark-gluon correlation, or Q^2 dependence, g_2 needs more advanced theoretical interpretation.

Twist-2 (leading-twist) contribution of the g_2 structure function can be derived by g_1 with Wandzura-Wilczek relation [34],

$$g_2^{WW}(x, Q^2) = -g_1(x, Q^2) + \int_x^1 \frac{g_1(x', Q^2)}{x'} dx', \tag{1.29}$$

where g_2^{WW} is the leading-twist approximation. If twist-2 contribution can fully explain g_2, only measurement of g_1 is needed to get full information of the spin structure of the nucleon. And, Burkhardt-Cottingham sum rule [35],

$$\int_0^1 g_2(x)dx = 0 \tag{1.30}$$

should be valid naturally as integration of g_2^{WW} over $0 \leq x \leq 1$ is identically zero. As it turned out from the measurement that the higher twist part of $\bar{g}_2 =$

$g_2 - g_2^{WW}$ can not be easily ignored. The higher twist part can be interpreted as increased quark-gluon correlation. Since each order of twist adds $1/\sqrt{Q^2}$ term, the study on $\bar{g}_2$ should be done at low Q^2 region.

Recent study of $\bar{g}_2$ shows that g_2 contains three components up to twist-3. A light-cone parton model [36] and an operator product expansion (OPE) [31] studies can express g_2 as follows:

$$g_2(x,Q^2) = g_2^{WW}(x,Q^2) - \int_x^1 \frac{\partial}{\partial x'}[\frac{m_q}{M} h_T(x',Q^2) + \xi(x',Q^2)]\frac{dx'}{x'}, \quad (1.31)$$

where $h_T(x,Q^2)$ is twist-2 quark transverse polarization distribution as explained above, and $\xi(x,Q^2)$ is a twist-3 part indicating quark-gluon interactions. As m_q/M suppresses h_T part, $\bar{g}_2$ is generally regarded as a twist-3 contribution. SANE can directly access this twist-3 information, for it measured both $A_{\parallel}$ and $A_{\perp}$, at kinematic regions of low Q^2 and high x.

It is noteworthy to mention twist-3 matrix element d_2. The OPE regards d_2 as the representation of quark-gluon correlation [7, 37]. It is the third moments of g_1 and g_2,

$$d_2 = 3\int_0^1 x^2(g_2 - g_2^{WW})dx = \int_0^1 x^2(2g_1 + 3g_2)dx. \quad (1.32)$$

It allows comparison with lattice QCD calculations and other QCD models. Interpretations of higher twist effect in OPE framework can be found in standard textbooks like Refs. [38–41].

Another motivation of SANE comes from nucleon resonance depending on spin. The most experiments measured spin structure on the DIS region, but recent experiments started to collect data in resonance region. The virtual photon absorption asymmetries in Eqs. (1.10) and (1.11) are related to helicity amplitudes according to the final state helicity of the resonance. They are $A_{3/2}$, $A_{1/2}$, and $S_{1/2}$. $A_{3/2(1/2)}$ is the amplitude of transverse photon for the final

state of helicity 3/2(1/2). For it is virtual photon, it can also have longitudinal photon amplitude $S_{1/2}$. These amplitudes build up physics asymmetries:

$$A_1 = \frac{|A_{1/2}|^2 - |A_{3/2}|^2}{|A_{1/2}|^2 + |A_{3/2}|^2} \tag{1.33}$$

$$A_2 = \sqrt{2}\frac{Q}{q^*}\frac{S^*_{1/2}A_{1/2}}{|A_{1/2}|^2 + |A_{3/2}|^2}, \tag{1.34}$$

where q^* is the (virtual) photon 3-momentum in the rest frame of the resonance. For example, ideally $A_1 = 1$ if the electromagnetic excitation of spin-1/2 resonance only contributes at the kinematics. On the other hand, A_2 represents interference term of transverse and longitudinal amplitudes.

When the resonances are studied, it is convenient to use the recoiled system's invariant mass W instead of Bjorken x. The W of the system X in Fig. 1.1 is given by

$$W^2 = (P+q)^2 = M^2 + 2M\nu - Q^2. \tag{1.35}$$

So, in this thesis, physics asymmetries are usually plotted along W, to show resonances more clearly.

1.3 World Data

Inelastic lepton-nucleon scattering has long been a powerful tool to investigate the structure of nucleon. Ever since experiments with polarized nucleus and lepton were technically accessible, various experiments have studied the nucleon spin structure. Especially, the EMC experiment has found that valence quarks do not fully build the proton's spin [26]. It was the starting point of intensive study of spin physics. For example, SLAC [27], CERN [28], DESY [29], and JLab [20] experiments have been carried until recently.

Usually g_1 was studied more than g_2, because of technical difficulties and g_2^{WW} approximation in DIS region. Quite large amount of data have been collected for the g_1 structure function already. In Fig. 1.3, $xg_1(x)$ shows consistent result from various experiments in DIS region. The Particle Data Group collected xg_1 of various Q^2 in DIS to see overall feature of $xg_1(x)$ [2]. The $g_1(x, Q^2)$ dependence on Q^2 is on the right panel. Only mild scaling violation is observed at high x and low Q^2 regions. The high x region is of particular interest, for this region is dominated by the valence quark. The measurement in $x \to 1$ limit can be the clean test of nucleon structure. Relativistic constituent quark models [42, 43] should be applied in this region, and perturbative QCD can be also used [44]. Unlike simple $SU(6)$ symmetry prediction of $A_1^p(x) = 5/9$, these models with broken $SU(6)$ symmetry and pQCD predict $A_1^p(x) \to 1$ as $x \to 1$. So we need to improve a global fit by high x region data, to extrapolate A_1 to the limit.

The study of g_2 was focused on higher twist effect, for $g_2(x, Q^2) \approx g_2^{WW}(x, Q^2)$ if g_2 has little higher twist contribution. In this regard, d_2 matrix element is an interesting quantity. Fig. 1.4 is SLAC data of $xg_2(x, Q^2)$ in DIS region. The SLAC E143 and E155 [3, 27, 45] data shows that approximately g_2 is close to g_2^{WW}, but with recognizable discrepancies also. And the matrix element d_2, which is directly related to the discrepancy between g_2 and g_2^{WW}, is reported positive. The SLAC experiments announced $d_2^p = 0.0032 \pm 0.0017$ at an average Q^2 of $5GeV^2$ [3].

The JLab experiment E01-006, or RSS, pioneered the measurement of the proton spin structure in the resonance region. They investigated low Q^2 and high x region, with $1.085GeV < W < 1.910GeV$. The result shows characteristic of resonance region, previously unobserved. Fig. 1.5 shows clear deviation from calculation of DIS extrapolation (curves in the plot). g_2 measurement is the

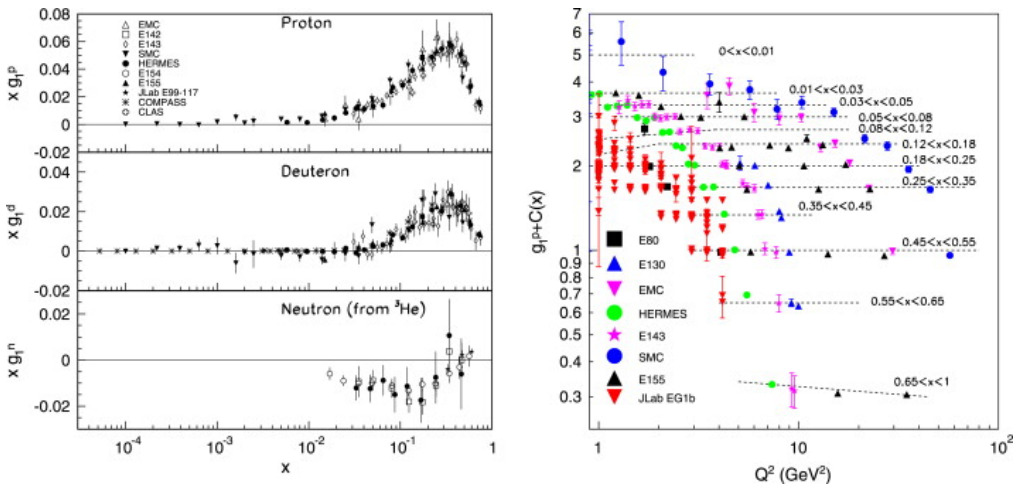

Figure 1.3: $xg_1(x)$ on the left, collected in DIS region ($W > 2GeV$), as compiled by the Particle Data Group [2]. The proton $g_1(x)$ versus Q^2 on the right, separated by several x [1].

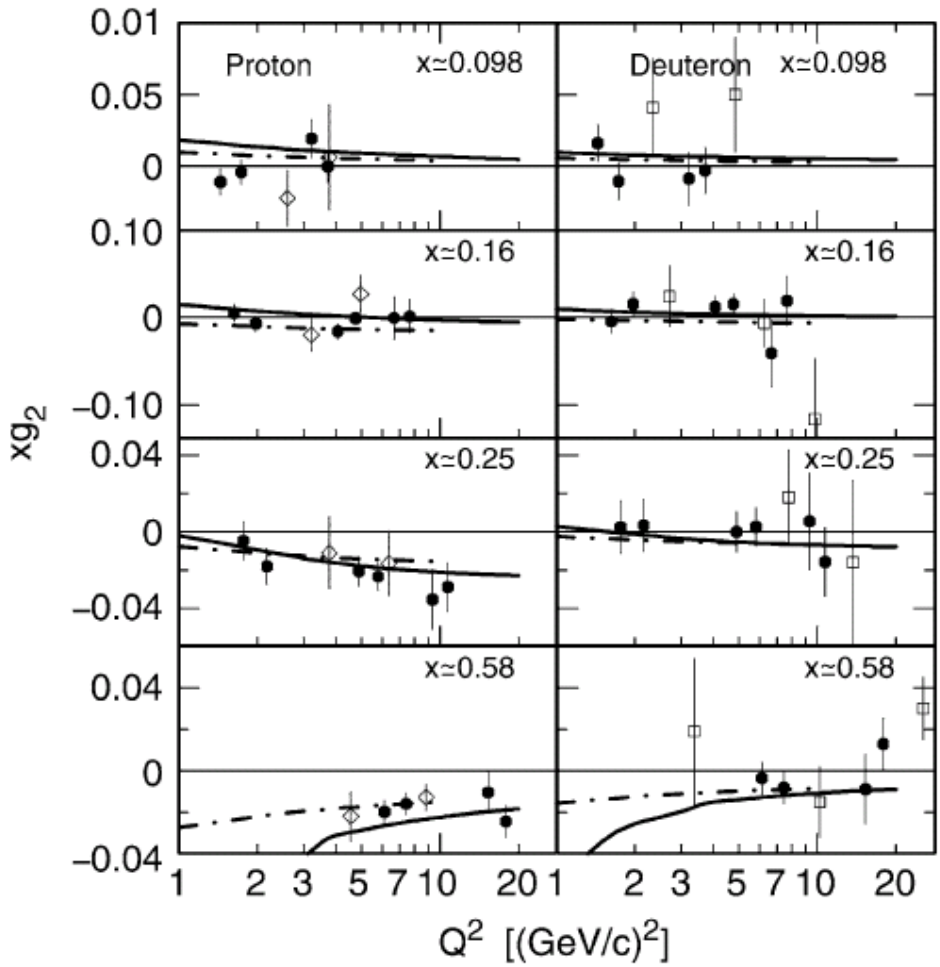

Figure 1.4: SLAC E143 and E155 result of xg_2 for proton and deuteron along Q^2, for selected values of x [3]. The solid curve is xg_2^{WW} and the dash-dot is the bag model calculation of Stratmann [4]

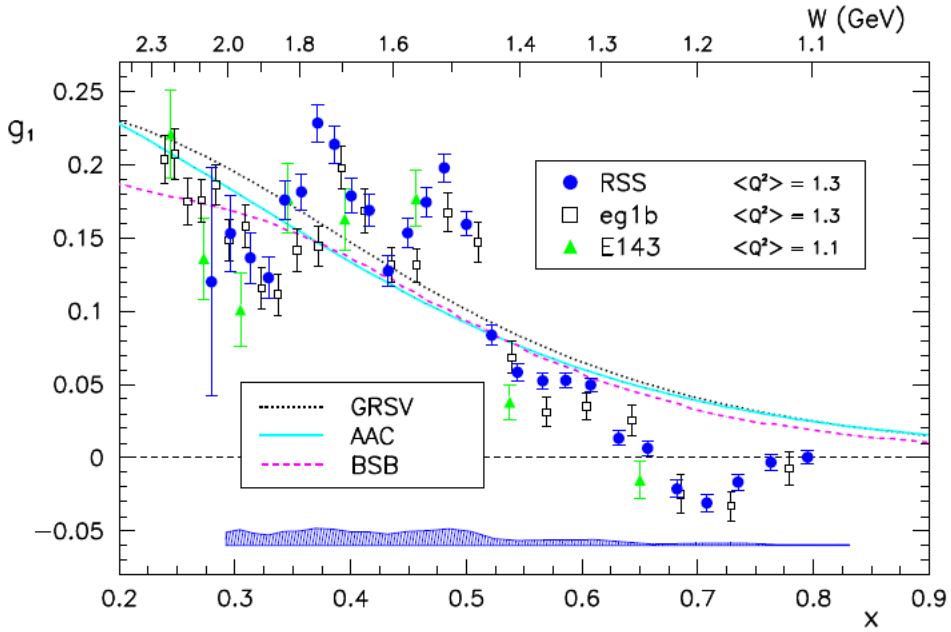

Figure 1.5: JLab RSS experiment g_1 result at $< Q^2 >= 1.3GeV^2$ [5].

main advantage of the experiment. Fig. 1.6 shows clear indication of twist-3 contribution in g_2. RSS presented $\bar{d_2} = 0.0057 \pm 0.0009(stat) \pm 0.0007(syst)$, where $\bar{d_2}$ is the d_2's integration over measured range $0.29 < x < 0.84$. If $1/Q$ dependence is assumed, this value of d_2 is consistent with SLAC's measurement [5].

Even though it is hard to expect A_2 or twist-3 part of g_2 directly, d_2 matrix element has lots of theoretical predictions. Bag models [4, 6, 7], QCD sum rules [8–10], Lattice QCD [11], and Chiral Soliton models [12, 13] have approached the problem. And experimental d_2 measurement was done by series of SLAC experiments [3], RSS [5], and HERMES [14]. Fig. 1.7 shows these theoretical

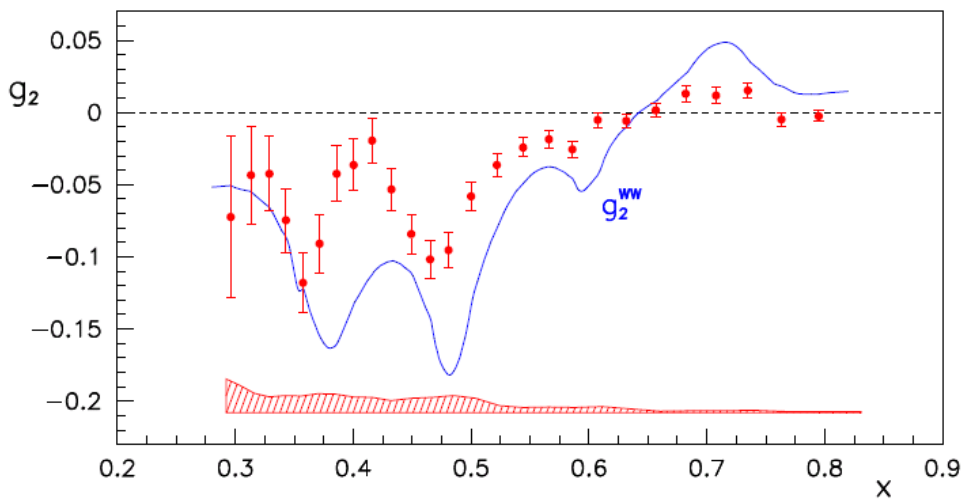

Figure 1.6: JLab RSS experiment g_2 result at $< Q^2 >= 1.3 GeV^2$ [5]. The solid curve is g_2^{WW} approximation from RSS g_1.

predictions and experimental results. All of the previous experiments yielded positive d_2, agreeing each other by assumed Q^2 evolution. The Chiral Soliton model based calculation is in good agreement with the experiments. But Q^2 dependence of d_2 should be examined.

1.4 Motivation of the Experiment

As discussed in previous sections, the study of the spin structure has usually been concentrated on deep inelastic scattering (DIS) region with large momentum transfer, which can be understood by a perturbative QCD. But lower energy regions have received attention recently. In such regions, nucleon resonances can be dominant, and intermediate phenomenons between the asymptotically free and the bounded quarks can be studied. Also, longitudinal polarization experiments were dominant so far. But it can probe only limited knowledge of the spin structure function g_1. In such experiments, g_1 will depend on which models to use for g_2, since transverse polarization configuration is not measured. Actually, the OPE method for QCD has caused new interest in the transverse spin [46, 47].

But up to now, world data of proton spin asymmetries, especially perpendicular asymmetry $A_\perp$, still lacks big kinematic region, except some data points[3, 5, 27, 45]. As the previous JLab experiment E01-006 produced successful results on this higher twist part [5, 48], the upgraded successor E07-003, or SANE, investigated wider kinematic region [15]. The experiment has measured the spin asymmetries of the proton. It was done in Hall C at Thomas Jefferson National Laboratory (JLab). Using a polarized electron beam and a polarized ammonia target, it produced data for parallel and near-perpendicular asymmetries. SANE searched the unexplored zones as indicated in Fig. 1.8.

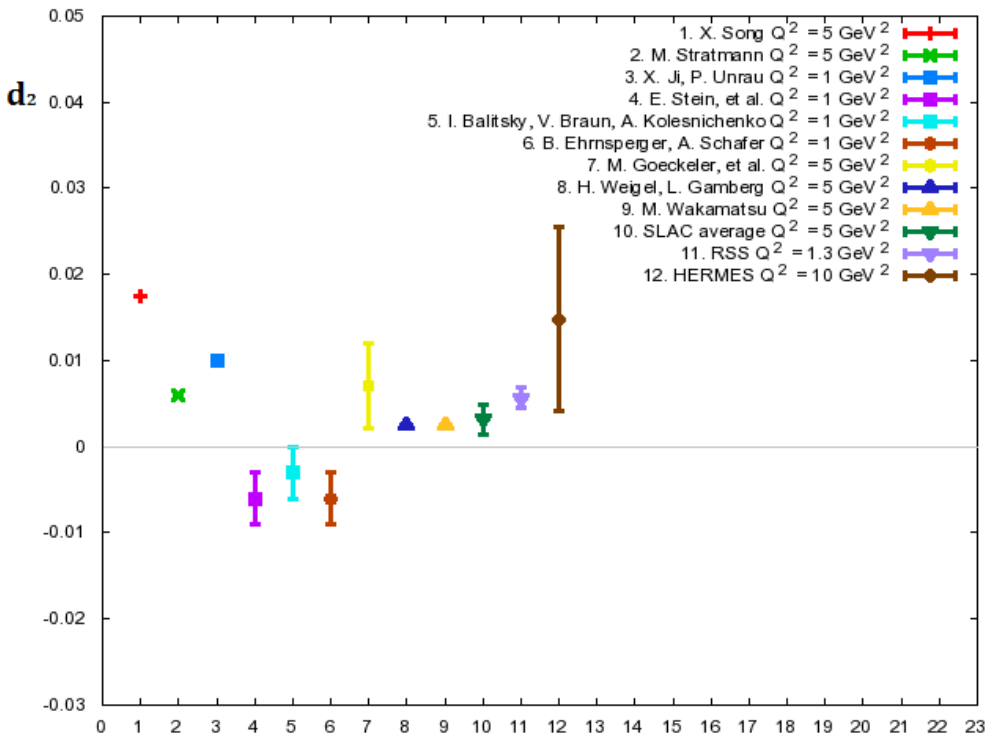

Figure 1.7: Various theories and experiments obtained twist-3 d_2 matrix element of proton. From left to right, following x-axis index, number 1-3 are Bag models [4, 6, 7], 4-6 are QCD sum rules [8–10], 7 is Lattice QCD [11], are 8 and 9 Chiral Soliton models [12, 13]. And 10 is SLAC average [3], 11 is RSS [5], 12 is HERMES [14].

This figure shows that high x and low Q^2 region has only few data points. Especially, the second panel showing $A_\perp$ data has broad unexplored region. SANE is dedicated to these regions.

In Fig. 1.8, SANE-BETA is the main experiment of SANE, using a detector complex named Big Electron Telescope Array (BETA). It covers broad region of $2.5GeV^2 < Q^2 < 6.5GeV^2$ and $0.3 < x < 0.8$. And SANE-HMS is the data from High Momentum Spectrometer (HMS). It is directly related to RSS experiment, using the same spectrometer. The HMS data covers mainly the extended region of RSS and the region of Q^2 evolution at $< Q^2 >= 1.9GeV^2$, which is intermediate region between SANE-BETA and RSS coverage.

SANE's unique feature comes from exploring low Q^2 and high x region, with direct measurement of both parallel and (near-)perpendicular asymmetries, filling the empty region of the world data. The main purpose is to learn everything possible about A_2 and g_2. Twist-3 effect is expected to be observed, especially through d_2 matrix element. Study of x and Q^2 dependency will improve the global fits of the spin structure functions. In this thesis, SANE-HMS data will be mainly discussed. Unexplored A_2 and g_2 of the resonance region will be presented, with the study of Q^2 dependencies of the resonances.

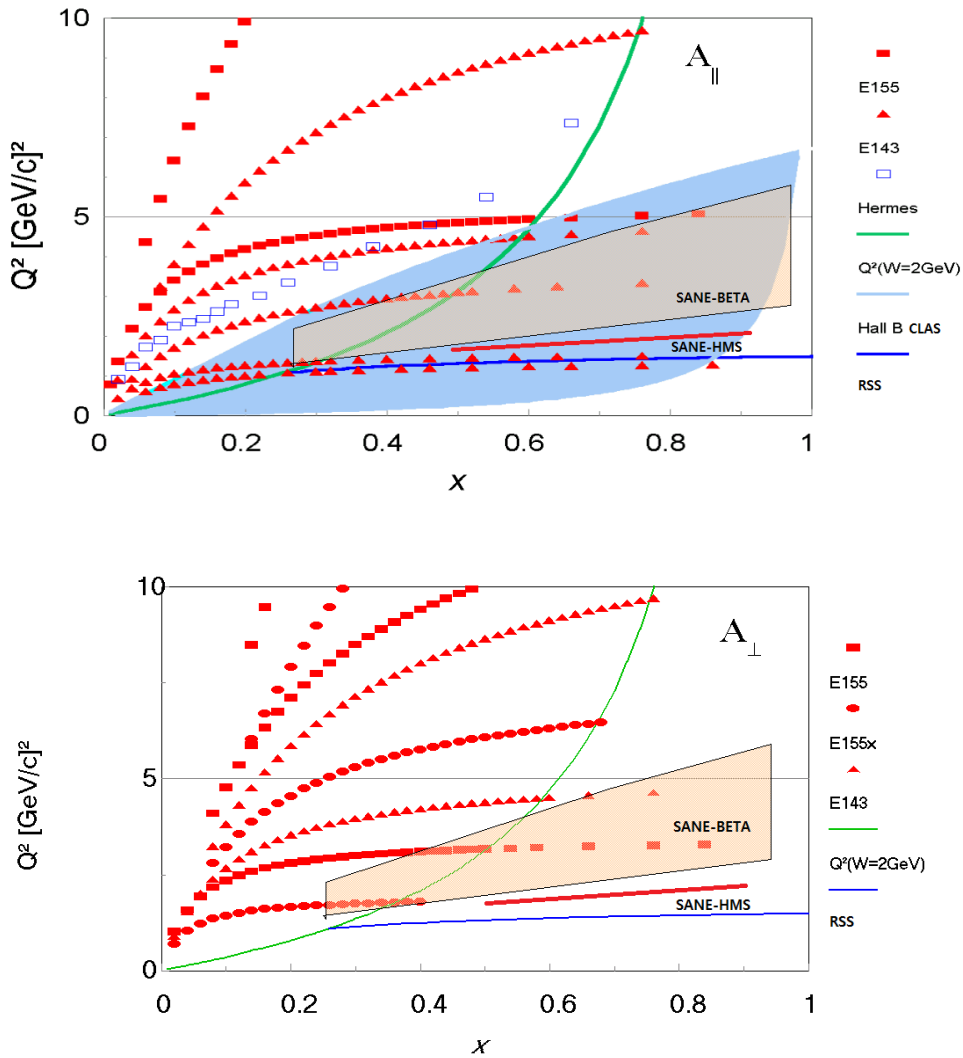

Figure 1.8: The kinematic range of SANE and previous experiments, shaded region indicating SANE-BETA kinematic coverage, and yellow line with label of SANE-HMS is HMS resonance coverage. Plots modified from Ref. [15]

Table 1.1: Kinematic variables of the SANE-HMS data, W(GeV) is the central value of each bin, and E(GeV) is the beam energy, and E'(GeV), and $\theta(^\circ)$ are of the scattered electron measured by HMS, averaged in each W bin. Para.(Perp.) is the parallel(near-perpendicular) data.

	Para.						Perp.					
W(bin)	E	E'	θ	W	Q^2	x	E	E'	θ	W	Q^2	x
1.095	4.736	3.448	20.65	1.096	2.098	0.8678	5.893	4.659	15.50	1.095	1.998	0.8626
1.125	4.736	3.436	20.46	1.126	2.053	0.8416	5.893	4.628	15.52	1.125	1.988	0.8380
1.155	4.736	3.425	20.26	1.156	2.007	0.8153	5.892	4.600	15.50	1.155	1.973	0.8135
1.185	4.736	3.409	20.10	1.186	1.967	0.7895	5.892	4.570	15.50	1.185	1.959	0.7897
1.215	4.736	3.384	20.05	1.215	1.942	0.7653	5.891	4.540	15.49	1.215	1.943	0.7662
1.245	4.736	3.354	20.05	1.245	1.925	0.7421	5.891	4.509	15.48	1.245	1.927	0.7432
1.275	4.736	3.323	20.05	1.275	1.907	0.7193	5.891	4.474	15.50	1.275	1.917	0.7212
1.305	4.736	3.291	20.06	1.305	1.890	0.6969	5.891	4.440	15.51	1.305	1.905	0.6995
1.335	4.736	3.257	20.07	1.335	1.874	0.6753	5.890	4.403	15.53	1.335	1.894	0.6786
1.365	4.736	3.222	20.10	1.365	1.859	0.6543	5.890	4.368	15.53	1.365	1.879	0.6577
1.395	4.736	3.188	20.11	1.395	1.841	0.6335	5.890	4.330	15.55	1.395	1.866	0.6377
1.425	4.736	3.153	20.12	1.425	1.822	0.6132	5.890	4.293	15.55	1.425	1.851	0.6179
1.455	4.736	3.117	20.12	1.455	1.801	0.5930	5.890	4.255	15.56	1.455	1.836	0.5987
1.485	4.736	3.082	20.10	1.485	1.779	0.5732	5.890	4.220	15.53	1.485	1.815	0.5791
1.515	4.736	3.046	20.10	1.515	1.758	0.5542	5.889	4.182	15.52	1.515	1.795	0.5603
1.545	4.736	3.010	20.08	1.545	1.733	0.5350	5.889	4.147	15.47	1.545	1.770	0.5414
1.575	4.736	2.980	19.97	1.575	1.697	0.5150	5.889	4.114	15.39	1.575	1.738	0.5218
1.605	4.736	2.954	19.78	1.604	1.650	0.4935	5.890	4.086	15.26	1.605	1.696	0.5013
1.635	4.736	2.931	19.54	1.634	1.599	0.4720	5.890	4.060	15.09	1.635	1.649	0.4804

Chapter 2

Experimental Setup

2.0.1 Overview of the Setup

SANE has used two detector complexes, Big Electron Telescope Array (BETA) and High Momentum Spectrometer (HMS). BETA covered a large solid angle of 200 msr, and served as a main detector. HMS, a built-in spectrometer of Hall C, collected complementary data. Even though BETA was the main detector, HMS also collected good amount of data. In the previous Hall C experiment to measure proton spin structure functions, Resonanace Spin Structure (RSS) experiment, only HMS was used to produce g_1 and g_2 [5]. The HMS data were independently analysed and have shown good agreement with other experiments. While BETA detected particles scattered to the left side of the beam, HMS detected electrons scattered to the beam right. Although BETA covers larger kinematic region, HMS, by varying the central angle and momentum, collected complementary data at four-momentum transfer Q^2 of 0.8, 1.3, and 1.9 GeV^2, from the resonance region to the region of invariant mass $W = 2.3\ GeV$. Some of the covered regions can also be used to extend the previous RSS experiment, allowing better determination of the integral of g_2 and the Q^2 dependency of

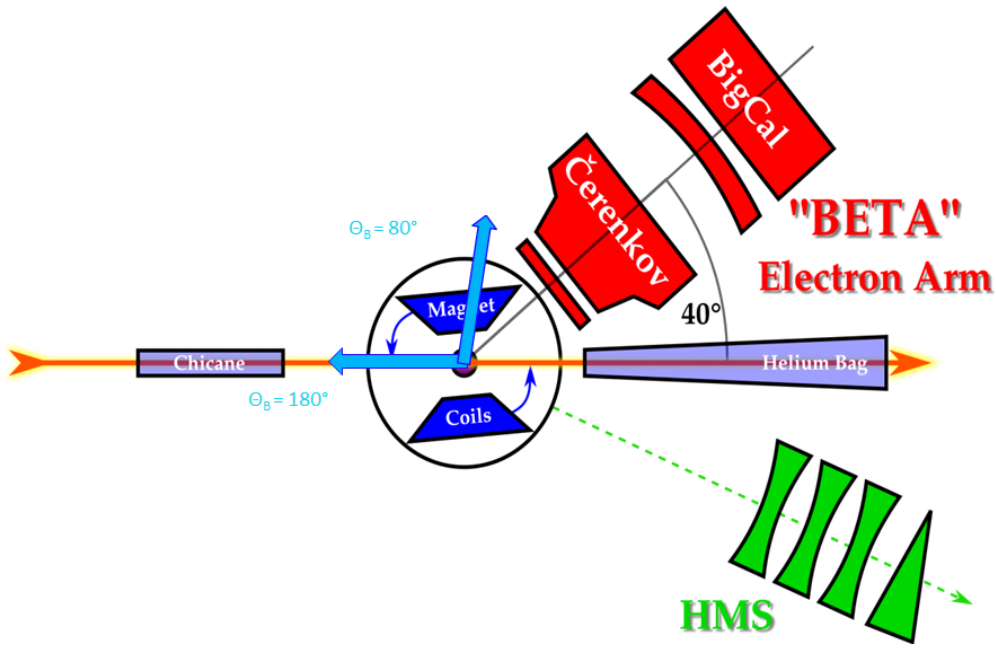

Figure 2.1: Schematic view of the experimental setting

A_1 and A_2 at resonance region.

Fig. 2.1 is the schematic view of the experimental setting. The polarized electron beam was delivered from the accelerator, Continuous Electron Beam Accelerator Facility (CEBAF), located at Jefferson Lab. The helicity of the electron beam can be controlled from the source and flipped by the frequency of $30Hz$ to reduce systematics errors in the asymmetry measurement. The beam energy used in SANE was 4.7 and $5.9GeV$. The target system consists of a vacuum chamber with rotatable superconducting magnet and target cells. The target material was a cup of frozen ammonia (NH_3) to be used as a polarized proton target. Dynamic nuclear polarization (DNP) method was applied to po-

larize the protons inside the target material. And a nuclear magnetic resonance (NMR) system measured the actual polarization of the target. Scattered electrons were detected by two detector sets. BETA, fixed at 40° on the left side of the beam direction, detected electrons with two hodoscopes, a Čerenkov detector, and a calorimeter. HMS, rotatable on the right side of the beam direction, has served as auxiliary detector mainly for electrons but occasionally also for protons. HMS detected electrons independently to BETA and the data served to measure the packing fractions of the target cells used in the experiment. At the same time, HMS asymmetry beam-target asymmetry data at low Q^2 region, as explaned in the Introduction. Protons in HMS were detected in coincidence with electrons in BETA. Such proton data were used to calibrate the detectors [19]. Chicane magnet in front of the target was to bend the beam to compensate the deflection by the target magnet. And the Helium bag after the target was to reduce the background from the beam up to the beam dump. More details will be explained in this chapter.

2.1 Electron Beam

2.1.1 Electron Source

The polarized electrons are produced by the injector system of CEBAF. The electrons are generated by DC photo-emission gun using a cathode. A Gallium Arsenide ($GaAs$) cathode is illuminated by a circularly polarized laser with a frequency matching the band gap of the crystal, to produce polarized electrons.

The circularly polarized laser light is produced using a Pockels cell. It converts linearly polarized light into circularly polarized one. The helicity of the outgoing light can be varied with the applied voltage to the Pockels cell. It varies at a frequency of $30Hz$ to change the beam helicity at the same frequency. Right-

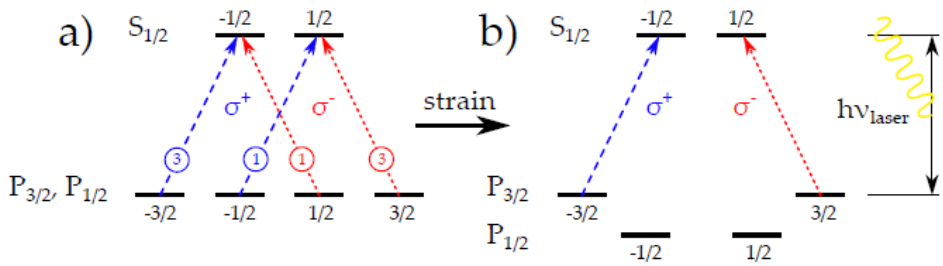

Figure 2.2: The energy levels and the laser-induced transitions of (a) unstrained and (b) strained and doped GaAs.

handed laser light excites electrons from valence band states of $P_{-3/2}$ and $P_{-1/2}$ to conduction band states $S_{1/2}$ $(-)$ and $(+)$, respectively. And left-handed light excites $P_{3/2}$ and $P_{1/2}$ to $S_{1/2}$ $(-)$ and $(+)$. These transitions are described in Fig. 2.2, right-handed light induced transition indicated by blue coarsely dotted line and left-handed by red finely dotted line. Theoretically, laser light induces transitions of both $P_{3/2}$ and $P_{1/2}$, for the two states are degenerate in a pure GaAs. The transition rate of $P_{3/2}$ is three times higher than $P_{1/2}$, due to the Clebsch-Gordan coefficients. So, it will produce 50% polarization of the beam [49]. JLab's GaAs cathode, however, are strained by phosphorus doping in every other layer. It is called "superlattice". The strain brakes the degeneracy, producing ideally 100% polarization like (b) of Fig. 2.2. Practically, it delivers a electron beam of 85% polarization with 1% quantum efficiency.

Three diode lasers are used, one for each experimental hall. Three bunches at $499MHz$ pulses are combined to a train of $1497MHz$. It is the resonant frequency of the RF cavities in the accelerator. The three are phase shifted by 120° relative to each other. The Pockels cell allows rapid change of the

polarization of the light. This combination produces pseudo-random based $30Hz$ helicity reversing beam. Additionally, a rotatable half-wave plate can be inserted to flip the helicity to observe time-dependent systematic effects. More details about polarized particle beam can be found Ref. [50].

2.1.2 Accelerator

The CEBAF accelerator is the main accelerator of JLab. It is a combination of two linear accelerators (north linac and south linac), 9 recirculating arcs, and an injector [16]. The injector supplies $67MeV$ electron beam to match with the linac energy. Each linear accelerator consists of 20 cryomodules. One cryomodule has 8 superconducting RF cavities, cryogenics, and power. Each cryomodule provides an acceleration of roughly $28MeV$, resulting an acceleration of $570MeV$ for each linac. Maximum 5-pass of this race-track is possible, accelerating electron up to $5.7GeV$. But in the period of SANE, a partial upgrade of CEBAF raised the maximum energy to $5.9GeV$, as a part of $12GeV$ upgrade plan. The layout is illustrated in Fig. 2.3.

The cavity is superconducting RF-resonant niobium cooled to $2K$. Oscillating electromagnetic field are supplied into the cavity to accelerate electron bunches by riding it on the crest of the wave. Input rate of electron and the RF frequency match to accumulate the energy on the beam. For the electrons from injector are already relativistic, they keep the phase with the RF field of the cavities. Electrons leaving one linac pass a recirculating arc of magnets, entering another parallel accelerator. The recirculating arc has dipole and quadrupole magnets. Dipoles bend the path of the electron and quadrupoles focus the beam. At the end of the arc, an identical series of magnets of opposite polarity recombine the electrons back into a common beam line of linac. This process is repeated until the beam reaches designated energy to supply to each

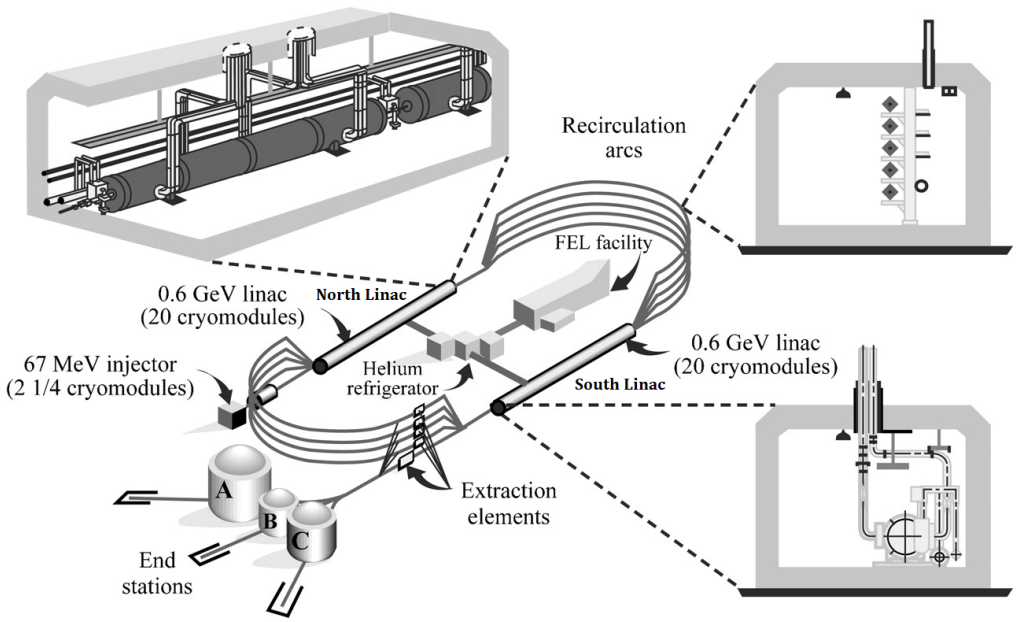

Figure 2.3: Layout of the Continuous Electron Beam Accelerator Facility (CEBAF) [16].

hall. Maximally five electron beams of different energies can be circulating at the same time.

At the end of the south linac, the beam at the designated energy is extracted to the hall requesting it. RF separator operating at $499 MHz$ extracts the beam. The extracted beam enters the beam switch yard (BSY), where the beam is guided to the experimental hall that requests it. So, each of the three halls can get the beam of the different energy and different current simultaneously. This feature of continuous supply of polarized electron makes the CEBAF a world-leading accelerator for fixed target electron scattering experiment.

As an inclusive double spin asymmetry measurement, SANE used polarized electron beam of 4.7 and $5.9 GeV$ energies. The nominal beam current was $90 nA$. Average beam polarization was about 73%.

2.2 Hall C Beamline

Though beam quality tests and any major measurements are performed by the accelerator crew, each hall has its own beam diagnostics for beam current, energy, position, and polarization. The beamline from the switching yard into Hall C consists of 8 dipoles, 12 quadrupoles, 8 sextupoles to steer and focus the beam [51].

2.2.1 Beam Position Monitor

Hall C beam position monitor (BPM) measures the beam position continuously. There are three BPMs on the beamline. Each consist of a resonant cavity with the same resonant frequency with the accelerator. Each cavity has four antennae: two for x and two for y position, rotated 45 degrees from the vertical to minimize synchrotron radiation damage. An asymmetry of the signal amplitudes

of opposite antennae is proportional to the distance between the beam and the midpoint of the antennae [52]. The BPM operation during SANE was quite unusual, for usual beam current in Hall C is on the order of $100\mu A$, not $100nA$. And slow raster changes the beam position rapidly even after the BPMs. So, BPM information is not exact beam position on the target. Only relative position from the beam center was recorded by the raster amplitude.

2.2.2 Beam Current Monitor

Hall C has three beam current measurement devices: two beam current monitors (BCMs) and a Unser monitor. BCMs are RF cavities oscillating at one third of the accelerator frequency. Their TM_{010} mode of oscillation is the same as the electron bunch frequency in the Hall C beam. Using a pickup antennae, the signal caused by the excitation of the cavity is converted to a DC voltage. A scaler of DAQ system reads this signal every two seconds. TM_{010} mode matches with the operational frequency of the accelerator, because the cavity response at this mode is insensitive to the beam position [53].

But the gain of BCM is varying slowly over time. So, it need to be calibrated periodically for its accuracy. A Unser monitor is used for this purpose. Unser is a parametric current transformer, obtaining absolute measurement of current. However, Unser is not suitable for real time measuring, for it has an unstable zero offset [54]. Unser is used for periodic recalibration of the BCMs. But, the asymmetry measurement depend not on the total charge, but on the relative ratio of charge of each helicity. So, it does not affect on the systematic uncertainty.

Table 2.1: Average beam energy for each run configuration [17].

Nominal E(GeV)	Target Field	Average E(MeV)	Standard Deviation
4.7	180°	4736.7	0.9
4.7	80°	4728.5	0.8
4.7	80°	4729.1	0.5
5.9	180°	5895.0	1.9
5.9	80°	5892.1	4.9

2.2.3 Beam Energy Measurement

Arc dipole magnets on the Hall C beamline are functioned as spectrometers to measure the beam energy entering the hall. For usual Hall C experiments, three pairs of high resolution wire scanners, superharps [55], determine the beam position and direction at the entrance, middle, and exit of the arc. The curvature of the beam deflected by 34.4° is used to determine the energy of the beam, as dipole field is precisely known.

$$E \approx p = \frac{e}{\theta} \int \vec{B} \cdot d\vec{l}, \tag{2.1}$$

where e is electric charge and θ is bending angle, and $\vec{B}$ field integrated over the path [56].

But, for the beam current was low during SANE experiment, the superharps could not work. So, the less accurate position form BPM was used to read the beam energy. Table 2.1 shows the average beam energy for each run configuration, according to the nominal beam energy and target field direction.

2.2.4 Møller Polarimeter

The beam polarization at the injector is not equal to that at the experimental halls, because the electron spin precession caused by recirculating arcs and Hall

C arc, due to its anomalous magnetic moment. The precession is related to the number of passes, beam energy, and the Wien angle. The Wien filter applies electric and magnetic fields of appropriate strength and direction, to rotate the electron spin at the injector for maximized longitudinal polarization at the halls.

Therefore, the delivered beam's polarization should be measured again. In Hall C, it is the function of the Møller polarimeter. Using one simple QED process, $\vec{e}+\vec{e} \rightarrow e+e$, it measures the asymmetry, which is proportional to the polarization. The polarized cross section of this reaction is given by

$$\frac{d\sigma}{d\Omega} = \frac{d\sigma_0}{d\Omega}[1 + P_t^{\parallel} P_b^{\parallel} A_{zz}(\theta)] \tag{2.2}$$

$$\frac{d\sigma_0}{d\Omega} = \left[\frac{\alpha(4-\sin^2\theta)}{2m_e\gamma\sin^2\theta}\right]^2 \tag{2.3}$$

$$A_{zz}(\theta) = -\sin^2\theta\frac{(8-\sin^2\theta)}{(4-\sin^2\theta)^2}, \tag{2.4}$$

where θ is the scattering angle $\frac{d\sigma_0}{d\Omega}$ is the unpolarized cross section, $A_{zz}(\theta)$ is the analyzing power, $P_t^{\parallel}$ is the target electron polarization parallel to the beam axis, and $P_b^{\parallel}$ is the beam polarization [57]. The asymmetry of the beam and target spins parallel and anti-parallel is

$$\frac{d\sigma^{\uparrow\uparrow} - d\sigma^{\uparrow\downarrow}}{d\sigma^{\uparrow\uparrow} + d\sigma^{\uparrow\downarrow}} = A_{zz}(\theta) P_t^{\parallel} P_b^{\parallel} \tag{2.5}$$

Hall C Møller polarimeter measures the scattering of the beam on a pure iron foil, which is polarized by 4 T superconducting split-coil solenoid. Because the analyzing power $A_{zz}(\theta)$ is maximized when the electrons scattered by 90° in the center of mass frame, it measures the pairs of electrons scattered by 90° in coincidence. Backgrounds from other processes are eliminated by the coincidence measurement. Movable collimators are used to narrow down the scattering angle, as in Fig. 2.4.

The Møller measurement cannot performed in the same time with data taking. So, the beam polarization is periodically measured. Table 2.2 and 2.3 shows

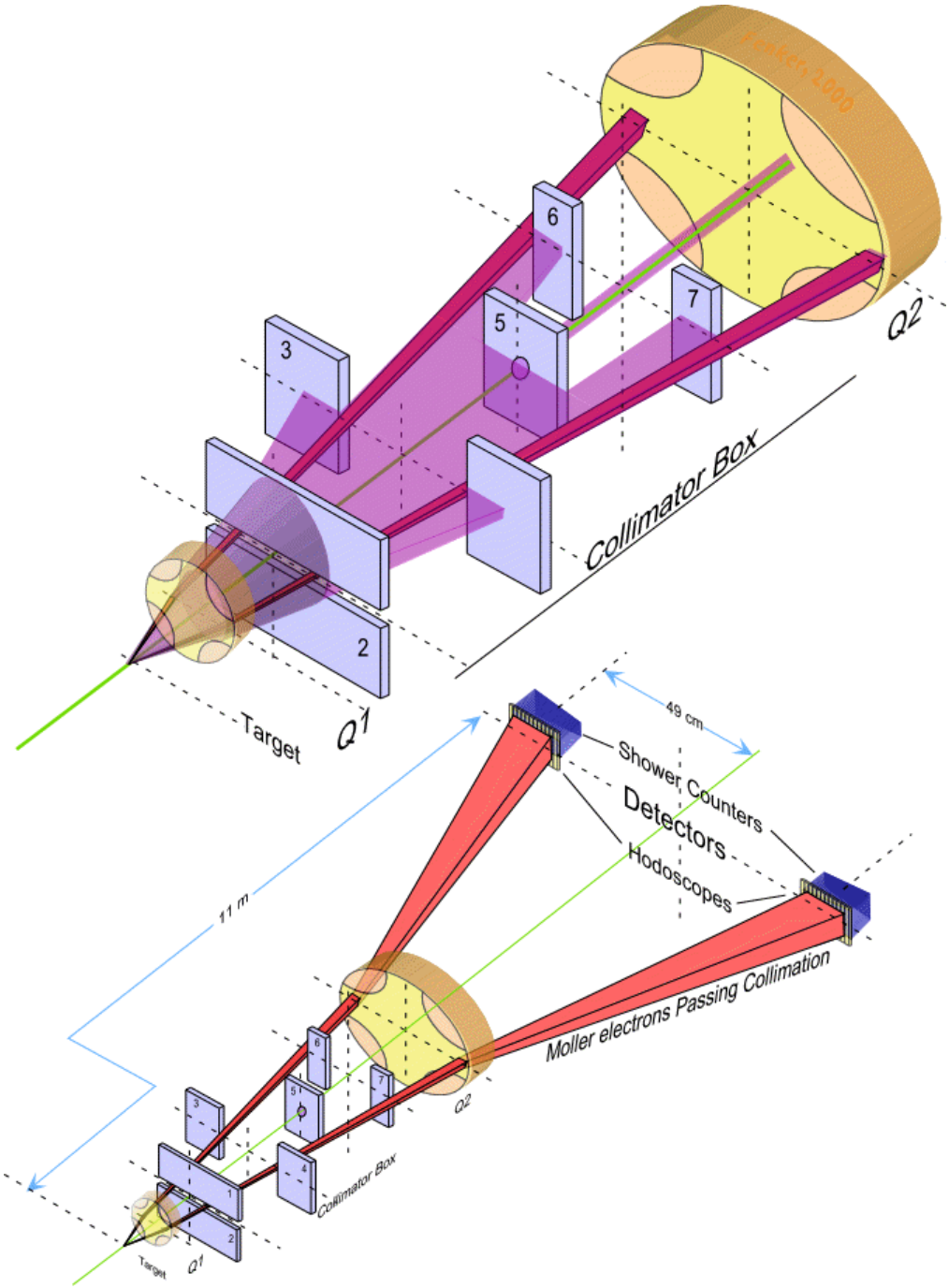

Figure 2.4: Schematic view of Møller polarimeter in Hall C.

the full list of Møller runs during SANE experiment, done by SANE collaborator D. Gaskell. By fitting the measurements, extrapolation of the beam polarization for whole experimental period is obtained. The fit has three degrees of freedom: the polarization at the source P_{source}, the degree of imbalance between north and south linac, and a global correction from the beam energy F_{corr}. With correction for the quantum efficiency of the cathode $F(\epsilon_q)$, half wave plate status n_{hwp}, and Wien angle θ_w, the beam polarization P_b is

$$P_b = (-1)^{n_{hwp}} P_{source} F_{corr} F(\epsilon_q) cos(\theta_w + \phi_{precession}) \tag{2.6}$$

where $\phi_{precession}$ is the the spin precession from source to the experimental hall, including recirculating arcs and Hall C arc.

$$\phi_{precession} = \frac{(g-2)}{2m_e} E \times \theta, \tag{2.7}$$

where m_e it the mass of the electron, g is the electron's gyromagnetic ratio, E is the beam energy while bending, and θ is the bending angle [17, 58]. Each recirculating arc bends 180°, and Hall C arc 37.52°. Combined with Møller measurement, it gives precise beam polarization. The code developed by D. Gaskell was used with porting. Fig. 2.5 is the run-by-run beam polarization. The more detail can be found in Ref. [17].

2.2.5 Raster

Not to heat one spot of the target too much, the beam passes the raster system, for the beam size on the target is very small($\leq 200\mu m$). The Hall C standard beamline has fast rasters only. It is designed to avoid damage of solid target and boiling of cryogenic target, as well as to prevent damage on target chamber windows and beam dump.

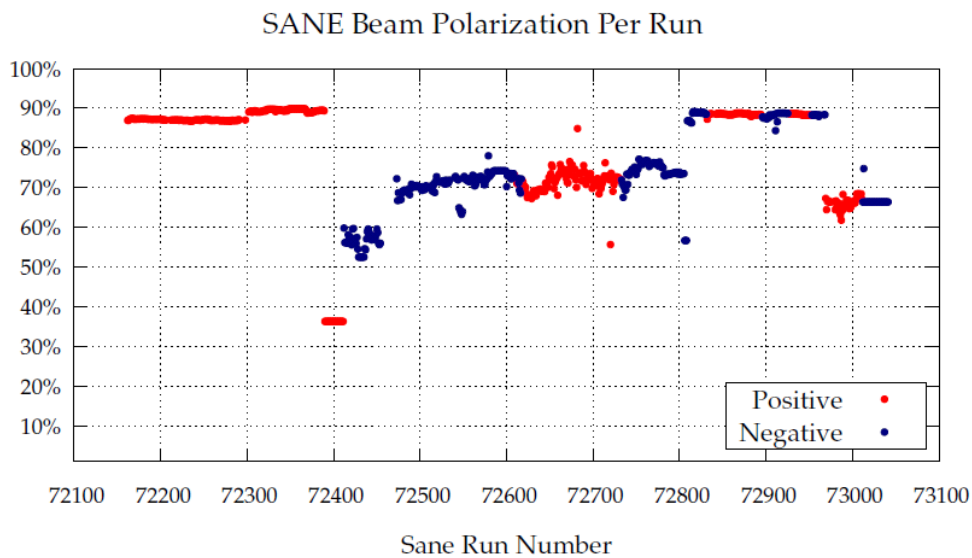

Figure 2.5: Absolute beam polarization for SANE experimental run [17]. Red (Blue) is positive (negative) polarization.

Table 2.2: List of SANE Møller runs, HWP is half wave plate, QE(%) is quantum efficiency, and Wien is Wien Angle(°), and Beam E is in unit of MeV, Polarizaion %.

Date	Run	HWP	Wien	Beam E	QE	Polarization
1/25	71942	IN	29.99	4730.46	0.1844	87.79±1.54
	71943	IN	29.99	4730.48	0.1844	88.21±0.98
	71944	IN	29.99	4730.51	0.1844	85.13±0.93
	71945	IN	29.99	4730.53	0.1844	87.71±0.99
	71946	IN	29.99	4730.53	0.1844	88.24±1.01
	71947	IN	29.99	4730.53	0.1844	86.76±0.95
	71948	IN	29.99	4730.53	0.1844	87.33±1.55
	71949	IN	29.99	4730.52	0.1844	86.58±0.99
	71950	IN	29.99	4730.52	0.1844	85.38±0.97
	71951	IN	29.99	4730.53	0.1844	86.71±0.97
2/1	72209	IN	29.99	4729.25	0.0888	89.00±1.02
	72210	IN	29.99	4729.29	0.0888	87.32±1.10
	72211	IN	29.99	4729.28	0.0888	83.45±1.04
2/5	72300	IN	29.99	4728.23	0.0708	87.26±0.68
	72301	IN	29.99	4728.27	0.0708	85.64±0.93
2/11	72465	OUT	29.99	5892.84	0.3124	-61.16±1.10
	72466	OUT	29.99	5892.70	0.3124	-60.56±1.11
	72467	OUT	19.99	5892.81	0.3124	-72.83±1.02
	72468	OUT	19.99	5892.43	0.3124	-72.04±0.98
	72469	OUT	19.99	5891.65	0.3124	-75.35±0.97
	72470	OUT	29.99	5891.75	0.3124	-71.88±1.06
	72471	OUT	29.99	5891.46	0.3124	-70.82±1.06
	72472	OUT	29.99	5891.08	0.3124	-70.64±2.17
2/14	72537	OUT	29.99	5891.24	0.2790	-73.36±1.08
	72538	OUT	29.99	5891.11	0.2790	-73.70±1.05
	72539	OUT	29.99	5891.03	0.2790	-72.19±1.83

Table 2.3: List of SANE Møller runs (continued from Table 2.2)

Date	Run	HWP	Wien	Beam E	QE	Polarization
2/24	72767	OUT	13.00	5892.92	0.0830	-75.51±1.08
	72768	OUT	13.00	5892.85	0.0830	-76.90±1.00
2/28	72839	IN	29.99	4728.95	0.2516	87.63±0.96
	72840	IN	29.99	4728.88	0.2516	86.28±1.08
3/9	72965	OUT	-18.00	5895.58	0.1635	-90.22±1.29
	72966	OUT	-18.00	5894.22	0.1635	-86.81±1.27
3/12	72977	OUT	21.19	4736.33	0.1789	65.83±0.97
	72978	OUT	21.19	4736.34	0.1789	66.36±0.99

The fast raster, located at 25 meter upstream from the target, consists of vertical and horizontal sets of steering magnets [55]. Triangular wave drives the magnet currents, to produce a uniform square beam spot of $1 \times 1mm^2$.

The slow raster is added for SANE, to spread the beam up to even larger area on the target. Although SANE uses relatively low current, the $1K$ target with high polarization can easily lose its polarization. Therefore, the beam is rastered by slow raster again. The three wave-form generators drive the slow raster magnets. Two of them are for circular motion, and the rest one is for spiral motion. They produces spiral raster pattern with $1cm$ radius. Fig. 2.6 shows examples of the events detected at HMS with rastering. Raster evenly spreads the beam on the target.

2.2.6 Chicane Magnet and Helium Bag

The target field magnet orientation is set to measure parallel or near-perpendicular asymmetry. For parallel setting, the target magnet is aligned to parallell to the beam direction, causing almost no deflection. But for near-perpendicular set-

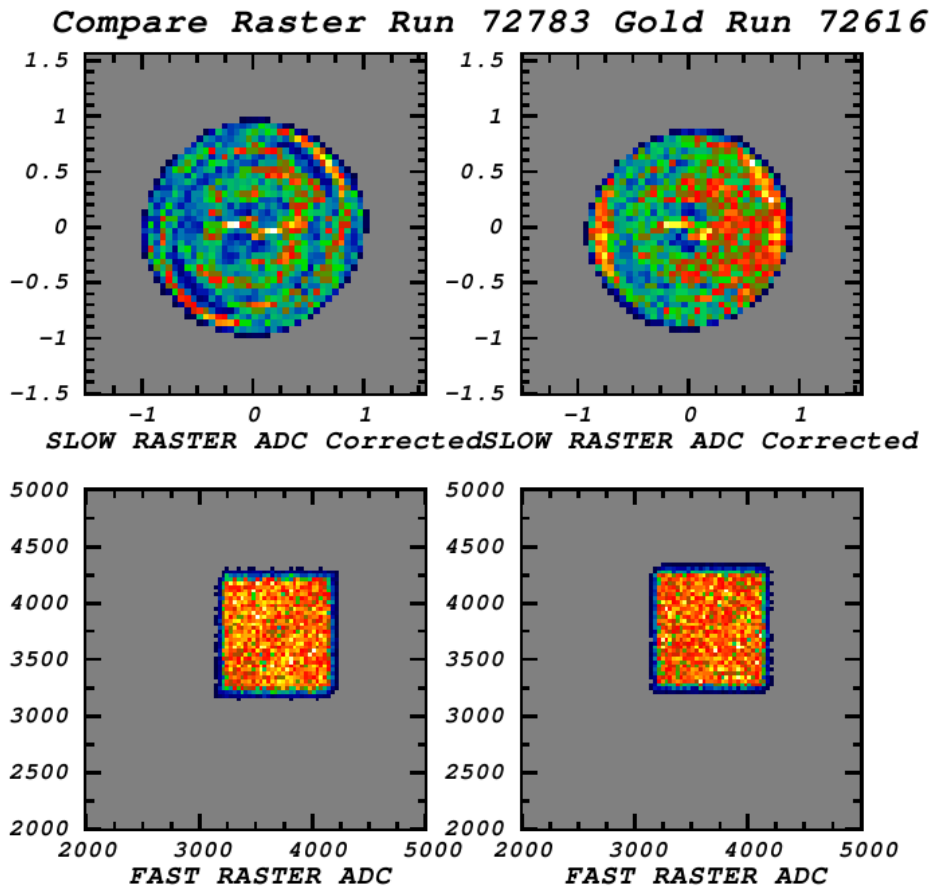

Figure 2.6: Examples of the distribution of the HMS events versus raster signal, which is monitored during the beam time.

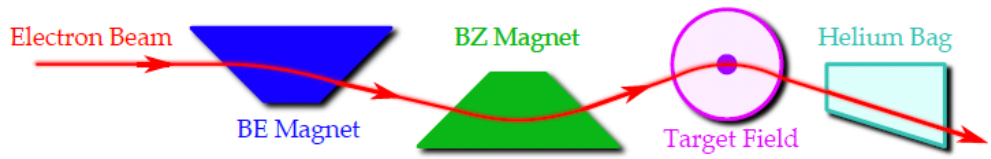

Figure 2.7: Schematics of chicane magnet operation for near-perpendicular target field.

Table 2.4: Chicane magnet parameters for near-perpendicular runs with two beam energies, integrated Bdl is in unit of Tm, where Beam E in GeV.

Beam E	BE Bend	BZ Bend	Target Bend	BE Bdl	BZ Bdl	Target Bdl
4.7	0.878°	3.637°	2.759°	0.513	1.002	1.521
5.9	0.704°	2.918°	2.214°	0.513	1.002	1.521

ting, the target magnet, which is $5T$ at the center, is set to 80° from the beam direction. So, the beam cannot hit the target cell. To prevent this, chicane magnets at upstream deflects the beam before affected by target magnetic field. As illustrated in Fig. 2.7, the electron beam is deflected down by BE magnet and then up by BZ magnet, to guide it to the center of target. Table 2.4 is the details of the chicane parameters, which were used for near-perpendicular runs.

In Fig. 2.7, the Helium bag is located at the downstream. It is mainly for radiation safety, for the electron beam going to beam dump can interact with air, causing unwanted ionization. They could make additional background and harmful secondary radiation. As the standard beam exit pipe cannot cover the deflected beam, the helium filled bag is used as the beam exit instead.

2.3 Target System

Solid $^{14}NH_3$ is regarded as a proton target. It is $3cm$ long frozen ammonia cell. The target system as a whole was a University of Virginia apparatus [59]. Liquid ^{4}He at $1K$ is supplied into the target ladder. $5T$ magnetic field by superconducting magnet and microwave radiated into target cell polarize target. This process is called dynamic nuclear polarization (DNP). Then NMR pickup coil measured the proton's polarization in real time. The average target polarization of 67 % was archived. For near-perpendicular asymmetry measurement, the whole target magnet rotated by 80°.

2.3.1 Target System

Fig. 2.8 is the target system as a whole. A Helmholtz style superconducting magnet applies $5T$ magnetic field on the target. The superconductor is cooled by $4K$ liquid helium. The cryostat liquid helium and nitrogen is supplied by the JLab Central Helium Liquefier. Helium from the magnet enters the refrigerator, which is a ^{4}He evaporation fridge cooling down the temperature to $1K$. Cooled down helium is supplied to target material. The target insert is a moveable ladder containing two ammonia targets with microwave horns, and a carbon target, also including holes and empty targets for beam position check. Through the microwave horn and connected waveguide, microwave is transferred to each ammonia target. The microwaves is generated in an extended interaction oscillator (EIO) tube. The microwave is at the frequency around $140GHz$ and is tunable by $\pm 2GHz$, to find suitable frequency for polarization. Optimal microwave frequency changes, due to beam current and target damage.

As summarized in Fig. 2.9, magnetic field, cryogenic, and microwave make the DNP process possible. But it is crucial to monitor real time polarization,

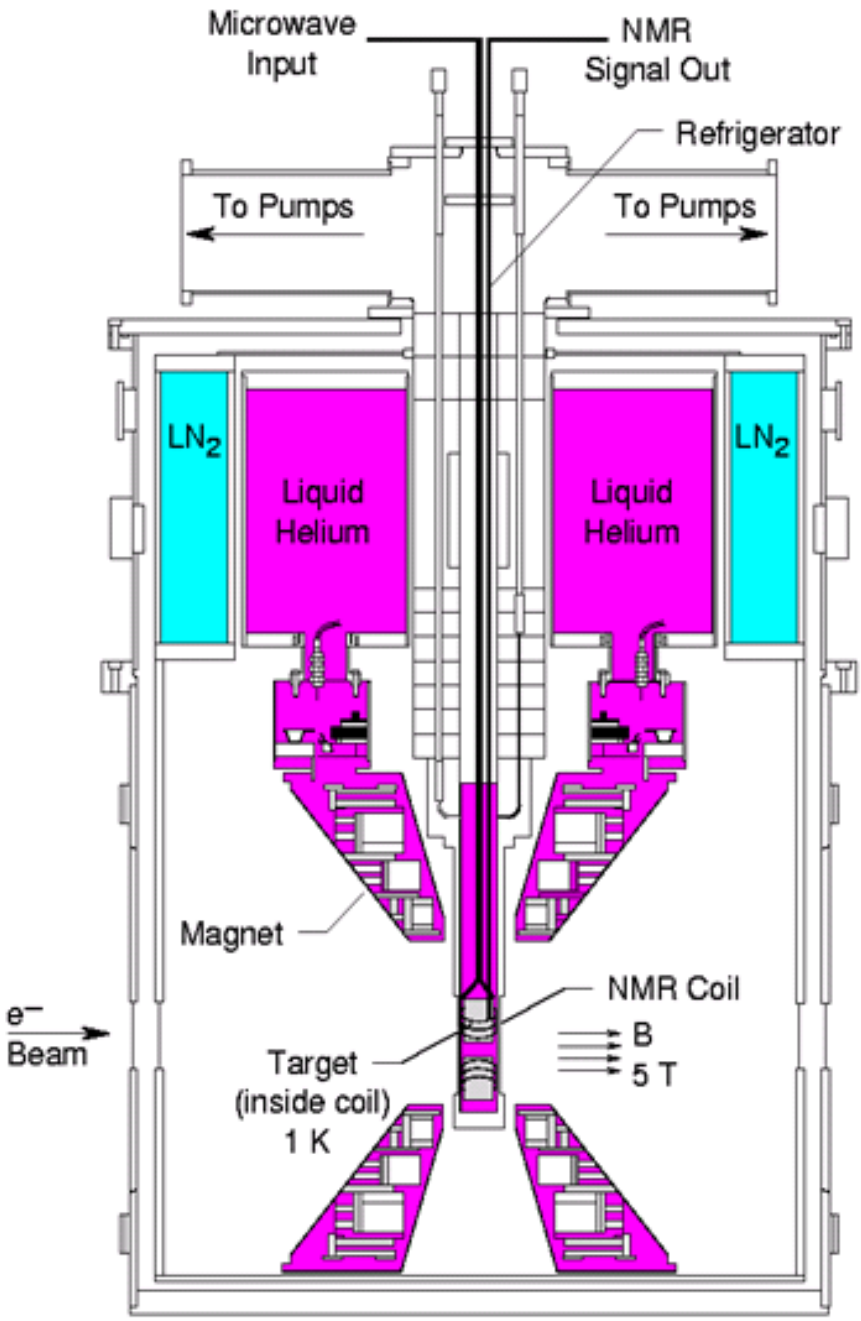

Figure 2.8: UVa target system used in SANE

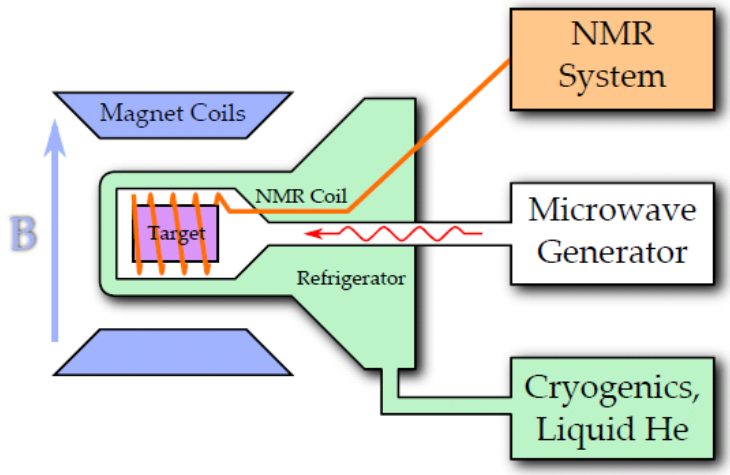

Figure 2.9: Schematics of the target system: cryogenic, magnetic field, microwave, NMR

for the optimal frequency changes by various condition. A target operator monitored the polarization and adjusted the frequency during the beam time. To monitor the polarization, NMR pickup coil inside the target cell gets the NMR signal and NMR measurement gives the polarization. The target system with electronics is managed by local computer in the hall and the computer is controlled remotely at the counting house. More details about target system can be found in Ref. [17] and [53].

2.3.2 Dynamic Nuclear Polarization

The magnetic field applied to split the degenerate states according to its magnetic moments by Zeeman effect. If particles are weakly interacting, the ratio of the population of the spin states (aligned $N_{\uparrow}$ and anti-aligned $N_{\downarrow}$) is calculable

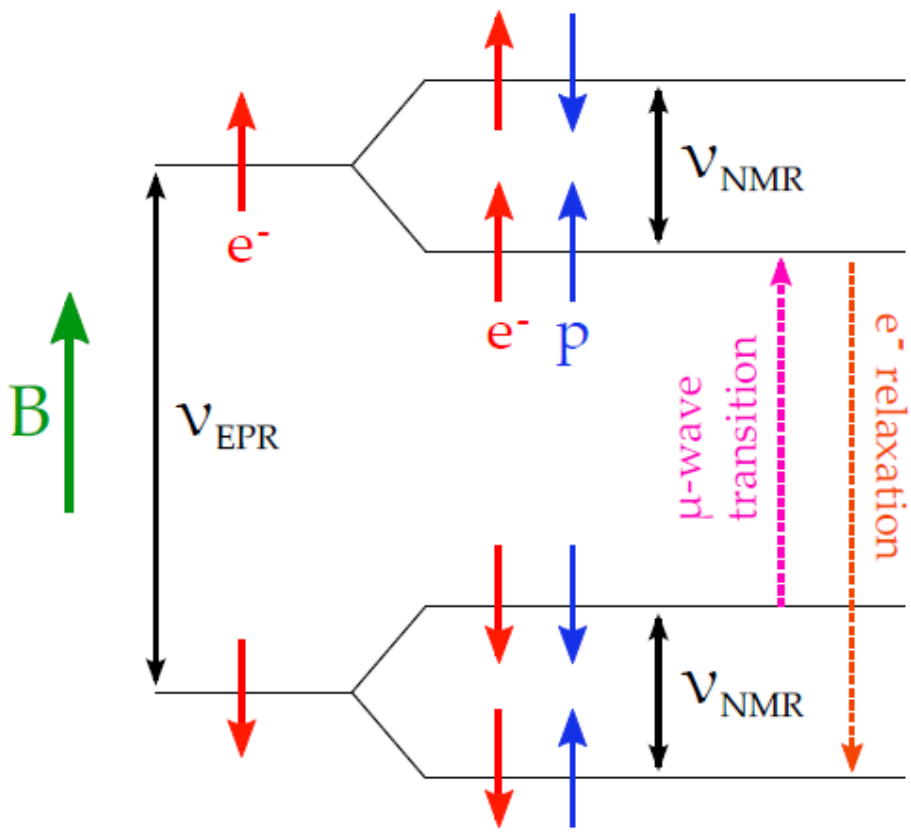

Figure 2.10: The energy spectrum and transitions used in dynamic magnetic polarizaiton [17].

by Maxwell-Boltzmann distribution.

$$\frac{N_\uparrow}{N_\downarrow} = \exp\left(\frac{2\mu B}{k_B T}\right), \tag{2.8}$$

where μ is the magnetic moment, B is the applied magnetic field, T is the temperature, and k_B is the Boltzmann constant. Hence, the polarization as defined by asymmetry of spin-1/2 particles is given by,

$$P_{1/2} = \frac{N_\uparrow - N_\downarrow}{N_\uparrow + N_\downarrow} = \tanh\left(\frac{\mu B}{k_B T}\right) \tag{2.9}$$

For example, Eq. (2.9) shows that the electron polarization at $1K$ in a $2.5T$ is approximately 92%. While the proton in the same condition has much smaller polarization of 0.25%, for proton's magnetic moment is far lower than electron's ($\mu_e \approx 660\mu_p$). Much higher magnetic field and lower temperature under beam is hard to achieve.

DNP is used to solve this problem. The target material should be doped with paramagnetic impurities. In such system of free electrons and nucleons, the Hamiltonian is given by,

$$H = H_0 - \vec{\mu_e} \cdot \vec{B} - \vec{\mu_N} \cdot \vec{B} + H_{ss}, \tag{2.10}$$

where H_0 is the free Hamiltonian for electrons and nucleons, H_{ss} is the spin-spin interatcions between electrons and nucleons, which is relatively small effect. Hyperfine splitting from the spin-spin interaction of electron and proton in the magnetic field makes four discrete energy levels, as in Fig. 2.10. Electron spins can be flipped by microwaves at the electron paramagnetic resonance (EPR) frequency ν_{EPR}. And proton spins can be flipped at the nuclear magnetic resonance (NMR) frequency ν_{EPR}. Though dipole selection rules ($\Delta m_j = \pm 1$) forbid both spin flipped simultaneously, mixing term H_{ss} make an access to this forbidden transition. Therefore, Thus, the transition $|\downarrow_e\downarrow_p> \rightarrow |\uparrow_e\uparrow_p>$ is

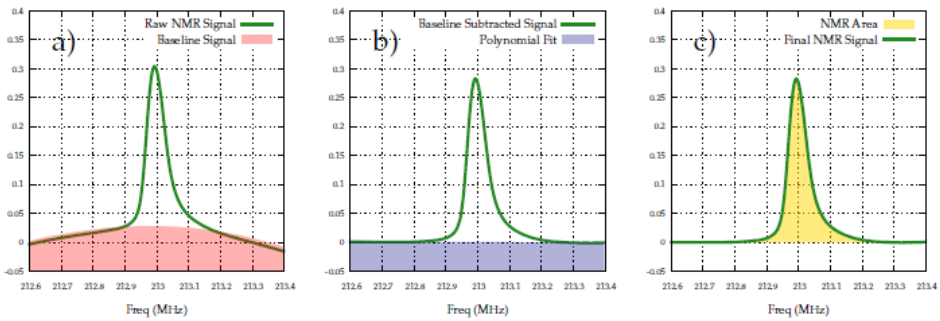

Figure 2.11: Steps of NMR signal analysis [17].

induced by microwave frequency of $\nu_{EPR} - \nu_{NMR}$. Much faster relaxation of electron allows electrons polarize another proton. This DNP process gives positive (aligned) polarization of protons. Likewise, the transition $|\downarrow_e\uparrow_p> \rightarrow |\uparrow_e\downarrow_p>$ is also possible by the frequency of $\nu_{EPR} + \nu_{NMR}$. And it makes negative (anti-aligned) polarization possible, to reduce systematic uncertainty. More detail of DNP is in Ref. [59]. In SANE, positive polarization is done by microwave frequency around $140.1 GHz$, and negative $140.5 GHz$.

2.3.3 Target Polarization Measurement

Target polarization was measured by Nuclear Magnetic Resonance (NMR) using Q-meter connected to resonant circuit. The inductor coil is inside the target cell. This NMR coil has both inductance L_C and resistance r_C. The impedance at the frequency ω is $Z_C = r_c + i\omega L_C(1+4\pi\eta\chi(\omega))$, where $\chi(\omega)$ is the susceptibility of the material and η is the filling factor. $\chi(\omega)$ has real part of dispersive and imaginary part of absorptive. Integration of the absorptive part is proportional

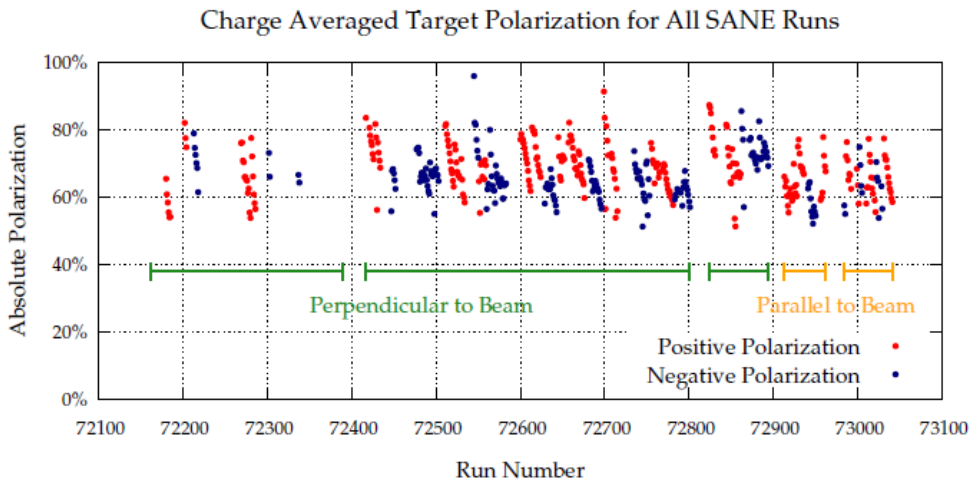

Figure 2.12: Offline target polarization for all SANE runs [17].

to the polarization:

$$P \propto \int_0^\infty Im[\chi(\omega)]d\omega. \tag{2.11}$$

An RF signal is applied to the resonant circuit, then the response is measured by the Q-meter. The RF signal is modulated around the Larmor frequency of the proton. The Larmor frequency of proton, in a 5 T magnetic field, is 213 MHz. From this Q-curve measurement, background signal should be removed. Fig. 2.11 shows the steps of this process. The main background is removed by modulating magnetic field from a). Even after background removed, background signal depending target environment, such as small temperature shifts, remains. So, a polynomial fit is applied on the baseline of b). The final curve in c) is integrated to get NMR area. This NMR area is in arbitrary unit, so it should be calibrated. It can be done by measuring Q-curve of a known polarization. Polarization of thermal equilibrium, i.e. beam off status, is Eq. (2.9) at the

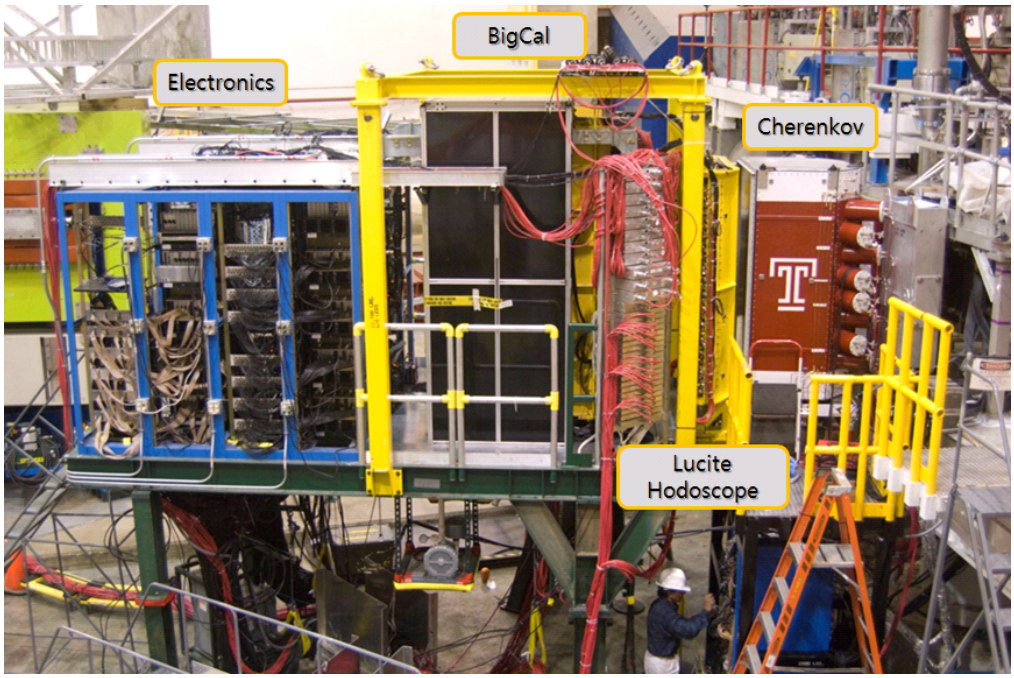

Figure 2.13: Side view of big electron telescope array (BETA), an official photo taken by JLab [18]. From right to left, a Čerenkov, a lucite hodoscope, a calorimeter named BigCal, and the electronics are shown.

temperature T. Though on-line analysis was done during the running time, off-line analysis was also performed after the experiment to get more precise results. The whole data of NMR signal was recorded during the experiment. The final polarization is in Fig. 2.12. It was done by J. Maxwell, with more details and estimation of error in Ref. [17].

2.4 Big Electron Telescope Array

BETA is the main detector complex of SANE. It is composed of a plastic scintillator hodoscope (Norfolk State U.), a nitrogen gas Čerenkov (Temple U.), a lucite hodoscope (NC A&T State U.), and a large lead glass calorimeter (GEP III collaboration). It has been designed for large acceptance, high pixelization, high background rejection, low deadtime, and appropriate energy resolution to observe high Bjorken x. Fig. 2.13 is the Side view of the BETA.

In this thesis, BETA data is not analysed. But, the packing fractions obtained with HMS data is applied to BETA data analysis [17, 53].

2.5 High Momentum Spectrometer

The HMS, during SANE experiment, detected the scattered electrons at various scattering angles, 15.4°, 16.0°, 20.2°. Together with beam energy and HMS central momentum, scattering angle determined the kinematic range to see. HMS can detect both electrons and protons, according to the polarity setting. The electron or proton entering to HMS goes through three quadrupole magnets and a dipole magnet. The frame supporting detectors is mounted on a common carriage with the magnets to maintain same optical axis, while shielding hut is supported on a different carriage. The entire HMS is on concrete rails to rotate it around the central pivot, where the target located at.

Fig. 2.14 shows the design of HMS, including zoomed view of detector set. HMS standard configuration consists of two gas drift chambers (DC1, DC2), four planes of scintillator hodoscopes(S1X, S1Y, S2X, S2Y), a gas Čerenkov, and a lead-glass calorimeter. Two drift chambers is to track the particles at the focal plane. The hodoscopes are for triggering and timing information. The Čerenkov and the calorimeter are for particle identification. The acceptance

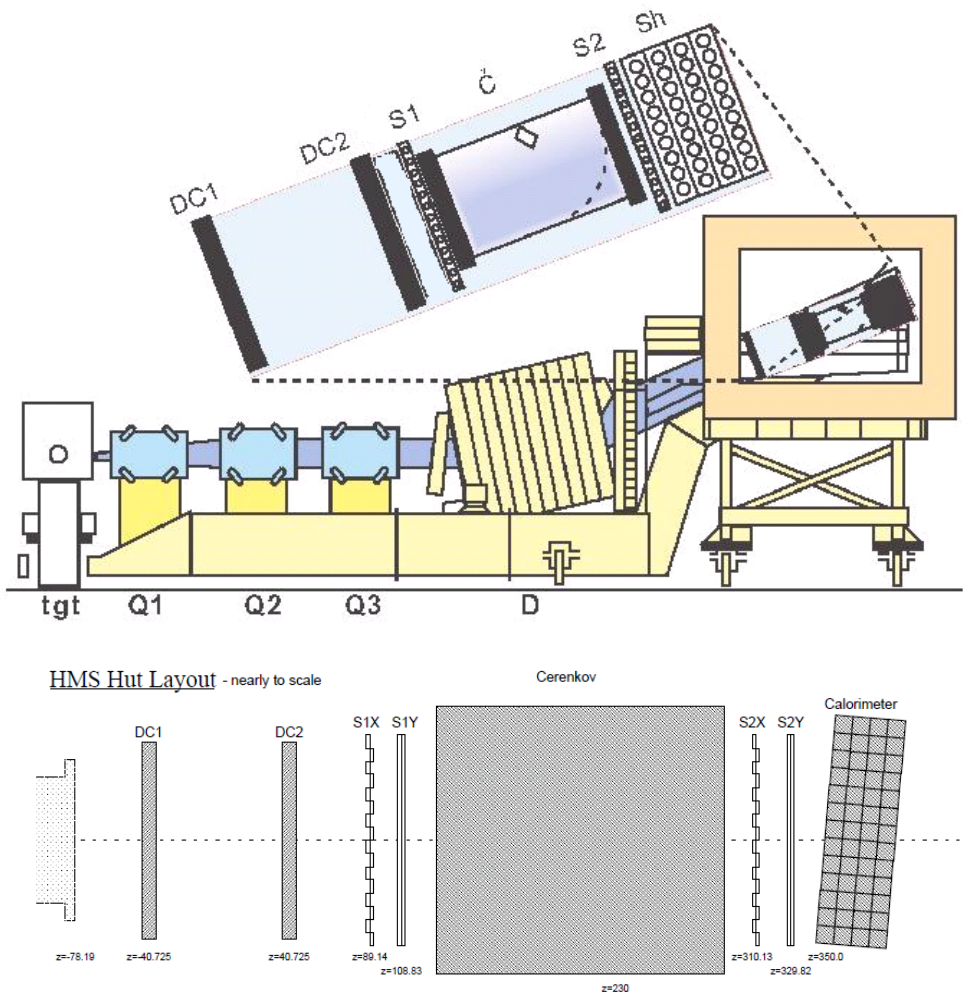

Figure 2.14: Side view of high momentum spectrometer (HMS), with schematics of the detectors.

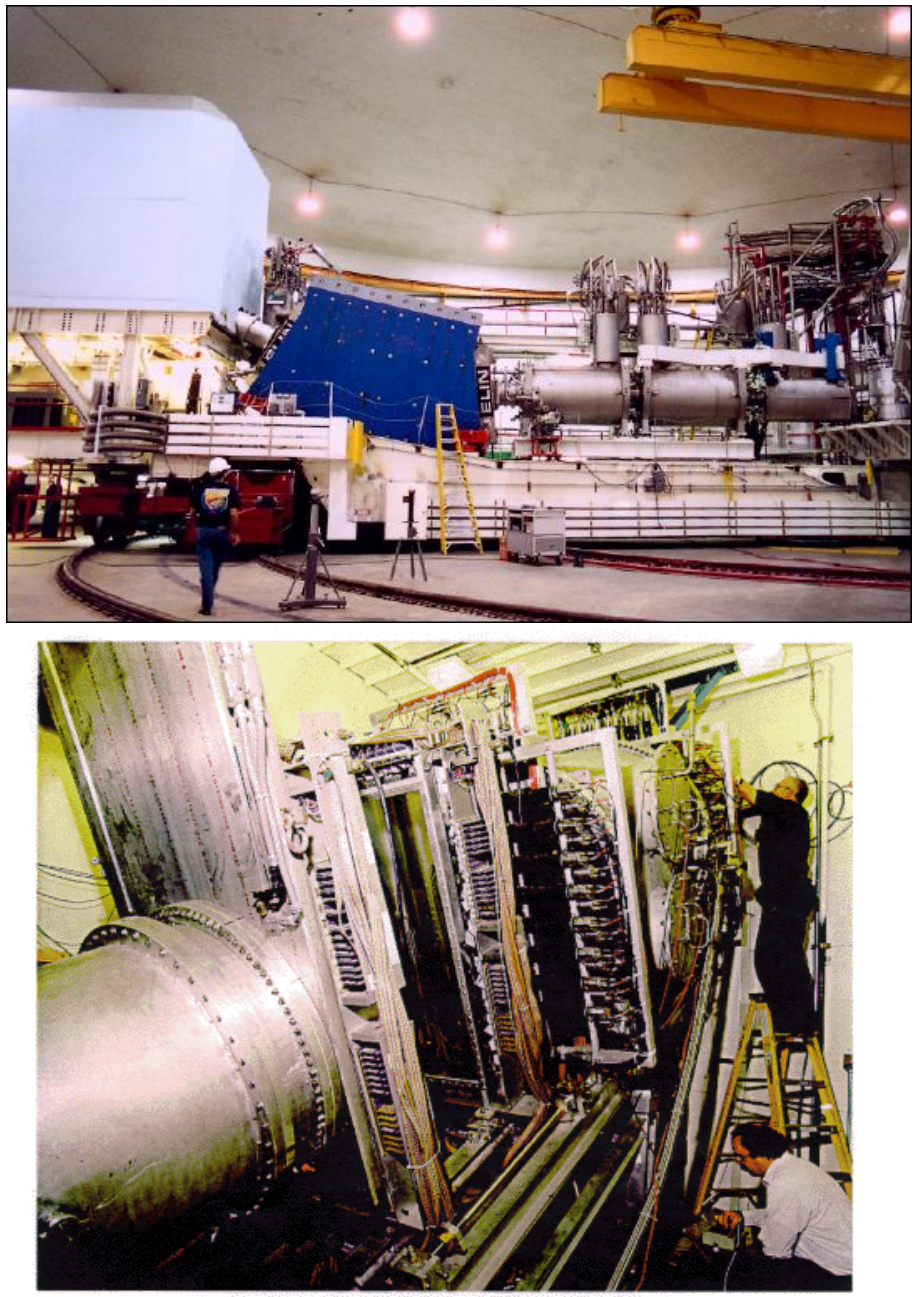

Figure 2.15: Side(top) and inside(bottom) view of HMS, official photos taken by JLab [18].

Table 2.5: Specification of HMS: acceptance and resolution

Max. central momentum (GeV/c)	7.4
Min. central momentum (GeV/c)	0.5
Momentum acceptance	±10 %
Momentum resolution	<0.1 %
Solid angle (msr)	6.74
Scattering angle acceptance (mr)	±27.5
Out-of-plane angle acceptance (mr)	±70
Extended target acceptance (cm)	7
Scattering angle resolution (mr)	1.0
Out-of-plane angle resolution (mr)	2.0

and resolution is in the Table 2.5. Detailed calibration and reconstruction using HMS data is in Ref. [19].

2.5.1 Magnets

The HMS magnet system is basically QQQD system. The first three quadrupole magnets focus the trajectories of charged particles. First magnet named Q_1 is smaller than next two identical magnets called Q_2 and Q_3. Q_1 and Q_3 focus in the dispersive direction, while Q_2 in the transverse direction. The optical axis of quadrupole is determined using the Cotton-Mouton method [60]. All magnets are aligned with respect to the optical axis. Maximum current I_{max} and dimension of the quadrupoles are in Table 2.6. All magnets in the HMS are superconducting magnet, cooled by $4K$ liquid helium.

COSY INFINITY program (Michigan State U.) was used to determine the initial model of the field setting [61]. The field map of each quadrupole has been well established. The map information is used to convert current to $\int B \cdot dl$,

Table 2.6: Specification of the HMS quadrupoles.

Magnet	Effective length (m)	Inner pole radius (cm)	I_{max} (A)
Q_1	1.89	25.0	580
Q_2	2.155	35.0	440
Q_3	2.186	35.0	220

as the magnetic field is regulated by the current. Although true focal plane is the plane where ray of particle trajectories focused at, HMS nominal focal plane is defined as the plane perpendicular to the central trajectory, roughly at the halfway between the two drift chambers. The particle's track is reconstructed by using the coordinates, in-plane, out-of-plane angles at the focal plane.

The dipole magnet is located at the end of magnet array, tilted by 25° from the central ray. Dipole also has been well field-mapped. The bending radius is 12.06 m, with effective length of 4.26 m. 1% deviation of the particle momentum from central momentum shows 3.71 cm dispersion from the central ray at the focal plane. Particles entering dipole at higher vertical position gets smaller $\int B \cdot dl$ than particles at central position, resulting smaller deflection. Likewise, particles at lower vertical position gets larger deflection.

2.5.2 Slit System

A slit system, inserting and removing collimators, is at the front of the magnet system. HMS collimators are shown at Fig. 2.16. They are HEAVYMET (90% machinable Tungsten with 10% CuNi). The sieve slit, 3.175 cm thick, is used to test the opticcal properties of HMS. It consists of small holes, with some missing holes for checking the left-right and top-bottom direction. Two octagonal collimatotors of different size is to determine the solid angle acceptance of the HMS. SANE used the larger collimator, so-called pion collimator. It has an opening

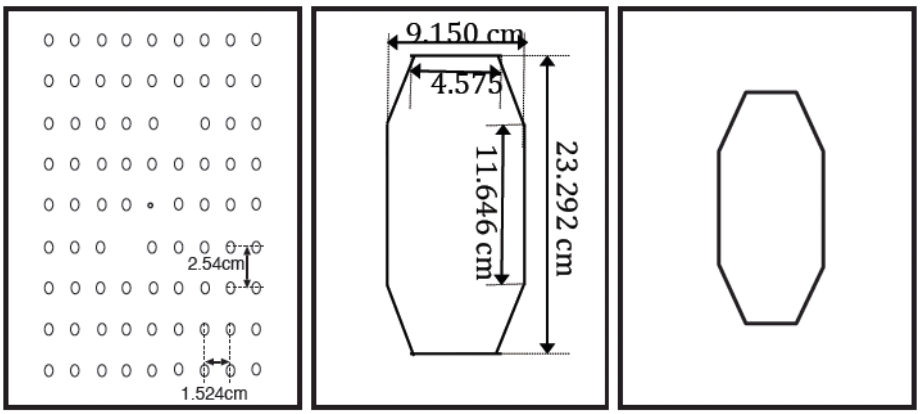

Figure 2.16: HMS collimators: (left to right) the sieve slit, the larger (pion) collimator, the smaller collimator.

as shown in the Fig. 2.16. As its distance from the target center is 166.00 cm, the angular acceptance is solid angle of 6.74 msr.

2.5.3 Drift Chambers

The drift chambers are gas-ionization detectors, to measure the position and angle of the particle trajectories at the focal plane. HMS drift chambers are two sets separated by 81.2 cm [62]. Each chamber has six planes: two for x coordinate (X and X'), two for y coordinate (Y and Y'), and the other two is rotated $\pm 15^\circ$ from the X plane (U and V), as in Fig. 2.17. Spacing between each plane is 1.8 cm. X measures the dispersive direction, while Y the non-dispersive direction. Each plane consists of field and sense wires. Negative field wires (cathodes) are 150 μm diameter gold-plated copper-beryllium. Positive sense wires (anodes) are 25 μm diameter gold-plated tungsten. The gas inside

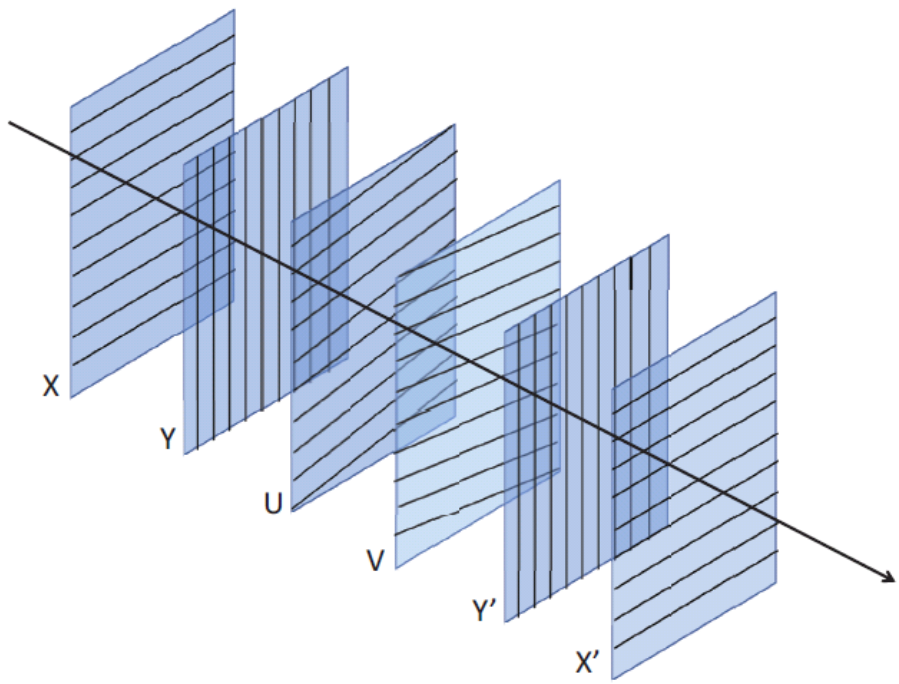

Figure 2.17: Six planes of HMS drift chamber, along the particle trajectory.

the chamber is half and half mixture of argon and ethane, doped with 1% isopropyl alcohol. The argon gas is the primary ionization source, and the ethane propagates the avalanche to the sense wire. The alcohol dopping prevents the gas from forming of polymers, which can be accumulated on the wires.

As a charged particle ionize the gas, liberated electrons are sensed by nearest anode. This signal is amplified and discriminated, then sent to time-to-digital converters (TDCs) located at the back of the detector hut. The hodoscope timing information is used to reconstruct the time of particle passing the focal

plane. Then, the time difference between the hodoscope time and the wire chamber time determines the drift time. The drift distance, calculated from drift time, determines the position of trajectory on the DC plane. The accuracy is better than 0.5 cm (half of the wire spacing) Collecting position information from planes, the trajectory is reconstructed. Large separation of two DCs gives a precise determination of the angle of the particle trajectory. The particle trajectory, together with dipole magnetic field map, determines the momentum of the particle.

2.5.4 Hodoscopes

Two sets of HMS hodoscopes contains two scintillator planes (x and y plane) in each set [63]. Fig. 2.18 is the structure of the hodoscope. It consists of strips of scintillators equipped with photomultiplier tubes (PMTs). Each X (Y) strip is 1.0 cm thick, 8.0 cm wide, 75 (120.5) cm long. They are overlapped by 0.5 cm each other to avoid gap. 16 paddles of X plane are to measure dispersive coordinate, while 10 paddles of Y plane to measure non-dispersive coordinate.

Because scintillator have relatively fast response time, the hodoscope signal is used as a trigger. Particle crossing the hodoscope occurs scintillation to emit photons. This light is guided by total internal reflection up to the PMTs at the ends. The PMT signal are sent to logic modules, to determine the triggering. At least signals from three out of four planes opens the data acquisition (DAQ). Triggered event is recorded with signals from other detectors. And such event is recorded into the scalers also, to determine the tracking efficiency.

2.5.5 Čerenkov

HMS gas Čerenkov is mainly used for pion rejection by particle identification (PID). It detects Čerenkov raditation from charged particles. It is a large cylin-

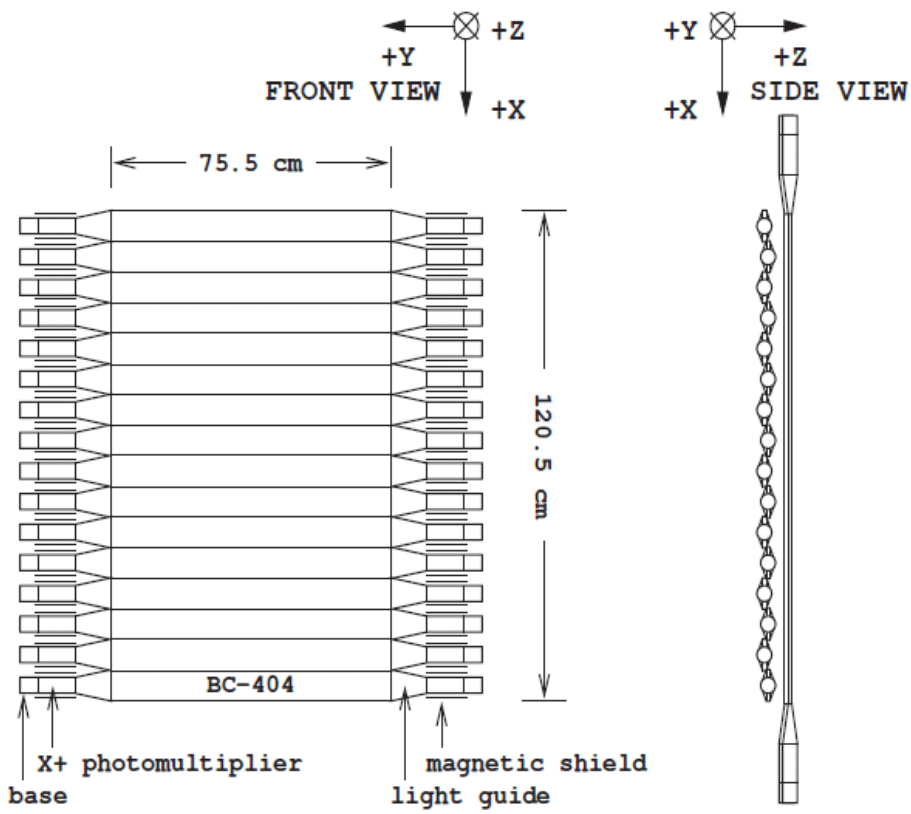

Figure 2.18: Dimensions of HMS hodoscope.

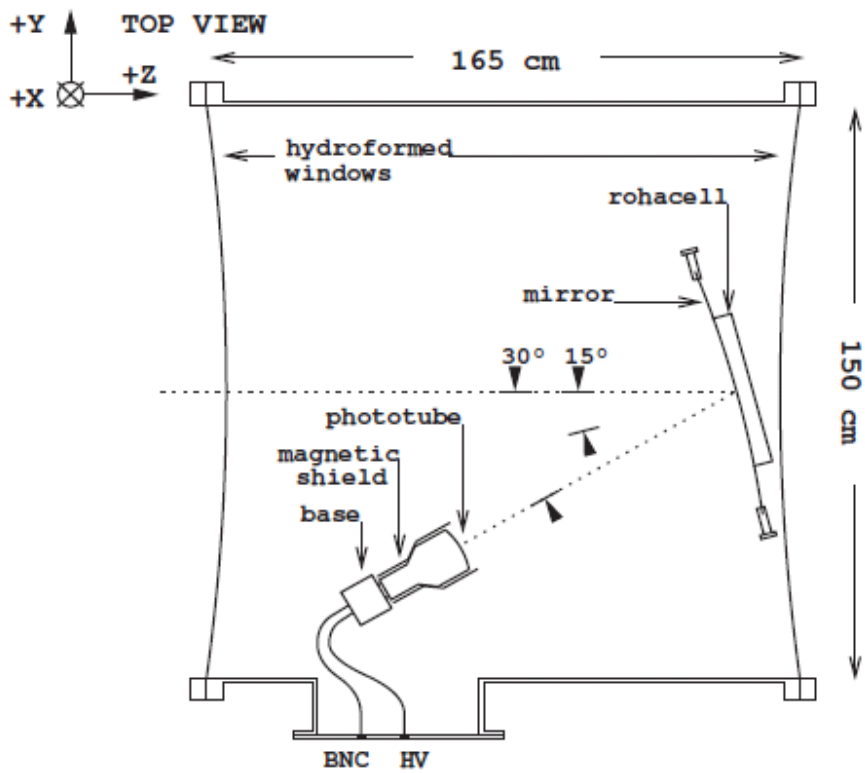

Figure 2.19: Dimensions of HMS Čerenkov.

drical tank, positioned between two hodoscopes. Two reflecting mirrors inside the tank focus the light to two PMTs. Fig. 2.19 is its structure.

Charged particle of faster speed than the light speed of the medium c/n, where c is the speed of light in vacuum, n is the index of refraction, radiates Čerenkov light. By careful determination of the index of refraction, the threshold speed c/n was determined to emit light from electrons, not from pions. 1-4 GeV electron and pions can be identified by HMS Čerenkov. So, the tank is filled with 0.42 atmospheres of C_4F_10, to make the index of refraction 1.0006. Resulting pion threshold is 4 GeV/c, while electron about 15 MeV/c. To reduce the misidentification of pion, as it can knock on electrons from windows, entrance and exit windows are 0.1016 cm thick Aluminium. At least 0.5 photoelectrons, together with 3/4 of hodoscope signal, triggers the DAQ.

2.5.6 Calorimeter

HMS has a lead-glass calorimeter at the back of the detector set. Together with Čerenkov, it is functioned as a PID detector. It measures the deposit of energy of charged particles. It consists of four layers of 13 blocks of lead-glass, as in Fig. 2.20. Lead-glass has radiation length of 2.54 cm. PMTs are attached to each blocks to detect the light from the electromagnetic shower. The calorimeter is inclined by 5° from the optical axis, to avoid missing of the particles by passing between blocks.

Dense (density of 3.86 g/cm^3) and high Z material like lead-glass makes high energy electrons to radiate Bremsstrahlung photons. This high energy photons creates e^+e^- pairs, which radiate more photons. This process continues until secondary particle's energy falls below 100 MeV, making a shower of particles. The charged particles produce Čerenkov radiation in the glass, and it is detected by PMTs. The amount of detected photons is approximately proportional to the

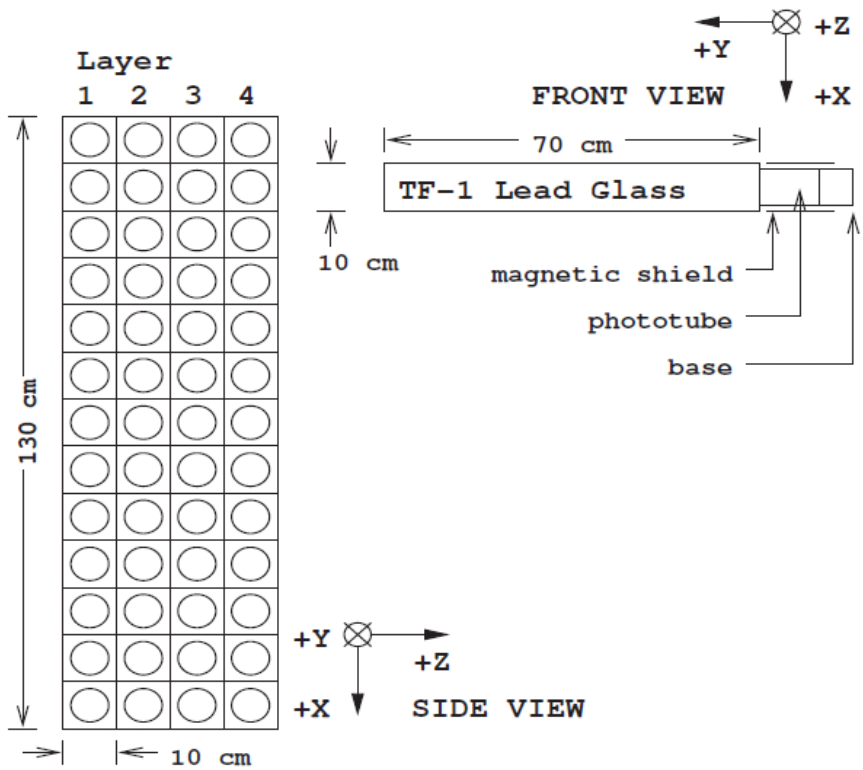

Figure 2.20: Dimensions of HMS calorimeter.

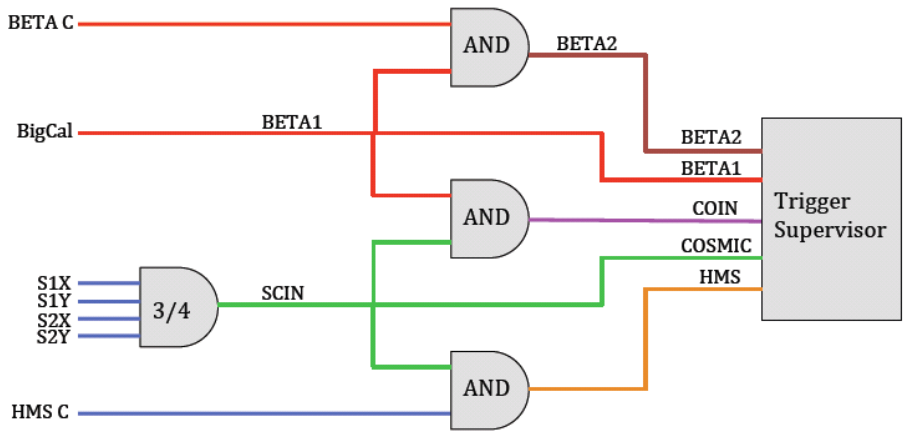

Figure 2.21: Schematics of triggers and trigger supervisor [19].

initial energy of the electron. Electrons of HMS operating momentum deposits entire energy to the calorimeter, i.e. ratio of deposited energy to momentum from tracking information should pick at 1. On the other hands, heavy hadrons like pions are too heavy to radiate Bremsstrahlung. Most pions are only stopped by a strong interaction with nucleons in the glass. 1 GeV Pion deposits about 300 MeV, resulting the ratio of calorimeter energy and momentum from tracking peaks at 0.3. Therefore, the Čerenkov and the calorimeter identify the particle.

2.6 Trigger and Data Acquisition

Trigger system is important to reduce unwanted data from background. A specified logical combination of the signals produces pre-trigger and opens the event read-out. When certain condition is satisfied, pre-trigger is formed. Pre-triggers from both HMS and BETA within a certain timing windows are accepted

in coincidence mode.

SANE used five trigger types, as in Fig. 2.21. They are called BETA1, BETA2, HMS, COSMIC and COIN. First four triggers are single-arm triggers, and COIN is the coincidence trigger that only occurs by HMS and BETA. BETA1 is triggered by BigCal only. BETA2 is produced by logical AND of both BigCal and BETA Čerenkov signal. When 3/4 hodoscope planes are fired (SCIN trigger), COSMIC trigger is made. If both 3/4 hodoscope and HMS Čerenkov conditions are satisfied, HMS trigger is generated. And COIN trigger is from both BETA1 and SCIN trigger. COIN is for coincidence data taking, when HMS gets protons. The HMS electron signal comes with HMS trigger.

The trigger supervisor (TS) controls these pre-triggers. TS accepts next pre-trigger, only if DAQ is not busy. It opens the gates for ADCs and starts the TDCs. For each run, 1000 triggers were collected for pedestals. Cebaf online data acquisition (CODA) handles three types of DAQ data: ADC and TDC signals, scalers recorded every two seconds, EPICS database (containing magnet settings, beam position, target control information).

Chapter 3

Data Analysis

The parallel and perpendicular asymmetries in Eq. (1.8) and (1.9) can not be obtained without corrections. The raw asymmetry is just asymmetry of beam helicities, $A_{raw} = \frac{N_+ - N_-}{N_+ + N_-}$, where $N_{+(-)}$ is the yield of positive (negative) helicity, corrected by charge and dead time. It is not real asymmetry, because the target has non-polarizable materials, and the protons and electrons are not fully polarized. Besides, real asymmetry should be Born-level to get correct structure functions.

Applying all corrections above, the real asymmetries are given by

$$A_{\parallel,\perp} = \frac{1}{f C_N P_b P_t f_{RC}} \frac{N_+ - N_-}{N_+ + N_-} + A_{RC}, \tag{3.1}$$

where $N_{+(-)}$ is the charged normalized yield for positive (negative) beam helicity, f is the dilution factor, which is roughly the ratio of number of polarizable protons over the total material in the target , C_N is a small ^{14}N nuclear polarization correction, P_b and P_t are the beam and target polarizations, f_{RC} and A_{RC} are radiative corrections. Details of each correction will be discussed.

3.1 Calibration and Reconstruction

Once raw signals are recorded by CODA, it should be converted into real physical quantities [64]. It is basically done by Hall C analysis package ENGINE. It is a FORTRAN code (partially C), designed to transform raw data to CERN PAW Ntuple variables [65]. The variables include reconstructed quantities, such as the beam-on-target position, the position on focal plane, and the scattering angle, and even measured momentum of the particle, Q^2, and W. ENGINE also deals with scaler information, like beam current, position, and magnet settings. ENGINE replay was modified for SANE analysis. Each run is replayed by SANE ENGINE, producing a HBOOK file containing event-by-event information in forms of Ntuple variables, and a run summary file.

Though during the beam time of SANE, major calibration was done for online analysis, it should be examined again to extract precise and reliable result. In HMS analysis, the particle trajectory and momentum should be determined with careful calibration. It is two step job: to determine the trajectory at the focal plane, and to reconstruct the track back to the target. A track is established when both HMS drift chambers measure at least four out of six planes hit. A straight line fit of these hit is called a "stub". The best fit of the stub is extrapolated to the focal plane, between two drift chambers. Four variables X_{fp}, Y_{fp}, $X'_{fp} = dX_{fp}/dZ$, and $Y'_{fp} = dY_{fp}/dZ$ are decided, where X_{fp} is defined as the position of the dispersive direction (vertically downward in the HMS coordinate system), and Y_{fp} of the non-dispersive direction (leftward). And Z is parallel to the HMS central ray.

The focal plane position is tracked back to the target. The reconstructed position on the target is explained by five variables of position X_{tar} and Y_{tar}, angle $X'_{tar} = dX_{tar}/dZ$, $Y'_{tar} = dY_{tar}/dZ$, and fractional deviation from the central momentum of HMS $\delta = (P - P_0)/P_0$, where P is the particle mo-

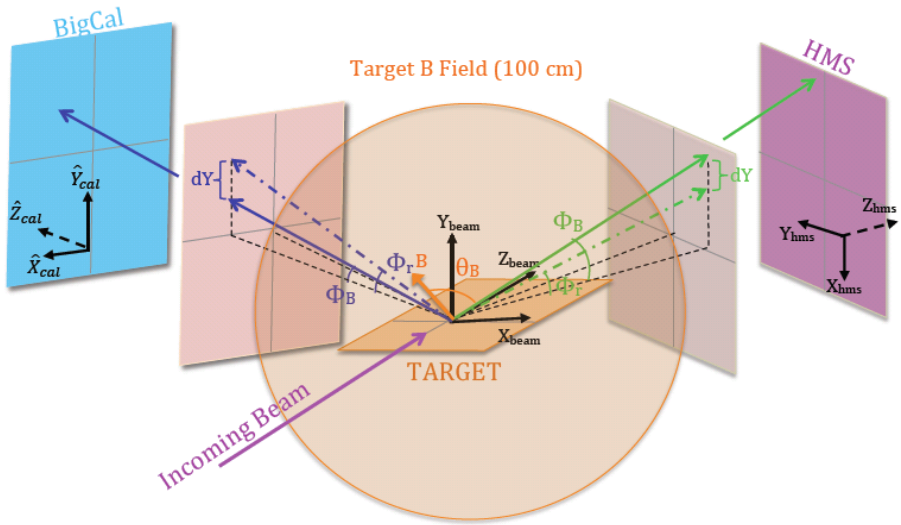

Figure 3.1: Coordinates used in analysis, showing the bent particle path due to the target magnetic field and its straight-line projection from the target [19].

mentum and P_0 is the central. These positions are in the HMS coordinate $(X_{hms}, Y_{hms}, Z_{hms})$, as illustrated in Fig. 3.1. Then, the reconstructed variables at the target can be related to the focal plane variables through a linear combination. The transformation is the optics matrix connecting $(X_{fp}, Y_{fp}, X'_{fp}, Y'_{fp})$ and $(X_{tar}, Y_{tar}, X'_{tar}, Y'_{tar}, \delta)$. It is determined by a fit from iteration, started from COSY INFINITY model [61]. Optics runs using the sieve slit and thin multi-foil targets are used to this process. Usual HMS optics matrix is limited due to the target magnetic field. So, the first reconstruction is limited to the region target field is weak enough, approximately 100 cm from the target center. Then, it is tracked back to the target using target field map. Also, the raster position is taken into account.

The calibration of HMS detectors has four major parts: hodoscope, drift chamber, Čerenkov, and calorimeter calibrations. Hodoscope calibration is to determine start time of drift chambers. It considers the cable delay between channels, light propagation time inside the scintillators, and pulse height discriminated. Drift chamber calibration is to convert drift time to drift distance. Using drift time distribution of large number of events, the conversion is calibrated. Čerenkov calibration uses the single photo-electron peak. ADC signal from PMTs is calibrated according to it. And calorimeter calibration is a χ^2 minimization process. The squared sum of difference between deposited energy and energy by reconstructed trajectory is minimized, with parameters of gain of each calorimeter blocks. Calibration was done by SANE collaborator A. Liyanage, with full details in Ref. [19].

For HMS analysis, major cuts to identify the electrons are ratio of energy measured by the Calorimeter E_{cal} to momentum measured by tracking P and the number of photo-electrons at the Čerenkov npe. $E_{cal}/P > 0.4$ and $npe > 2$ cuts are used to eliminate pion signals. Fig. 3.2 shows particle identification of

HMS using these cuts. Also, tracking efficiency using pedestal runs are applied. To extract the most reliable signal, Energy variation from the central HMS momentum setting is limited to 10 %.

3.2 Packing Fraction

Granular type of ammonia causes packing fraction issue. Target cell is not completely filled with solid ammonia. So, actual amount of material should be derived from data. It is closely related to the dilution factor. The dilution factor is the ratio of the yield from the proton to the yield from all materials in the target, nitrogen of ammonia, liquid helium, and small amounts of materials in the target system. Because only proton is polarizable material in the DNP process, the raw asymmetry should be divided by the dilution factor f. It is given by

$$f = \frac{N_1\sigma_1}{N_{14}\sigma_{14} + N_1\sigma_1 + \sum N_A\sigma_A}, \tag{3.2}$$

where σ_A is the electron-nucleus cross section, and N_A is the number of scattering nuclei in the target, when A is the mass number of the nucleus.

In SANE, N_A of hydrogen, nitrogen, and helium are unknown, because unknown amount of ammonia filled the target cell and the remaining volume is filled with liquid helium. So, the packing fraction should be obtained, and HMS electron data is used for this purpose. The packing fraction pf is defined as the fraction of volume in the target cell occupied by the ammonia. It is equivalent to the effective cell's length completely filled with ammonia, assuming cylindrical symmetry. Thus, $N_A = N_0\rho_A z_A/M_A$, where N_0 is the Avogadro's number, ρ_0 is the density of nuclear material of mass number A, z_A is the effective cell length fill with the material, and M_A is the atomic weight. And it is directly related

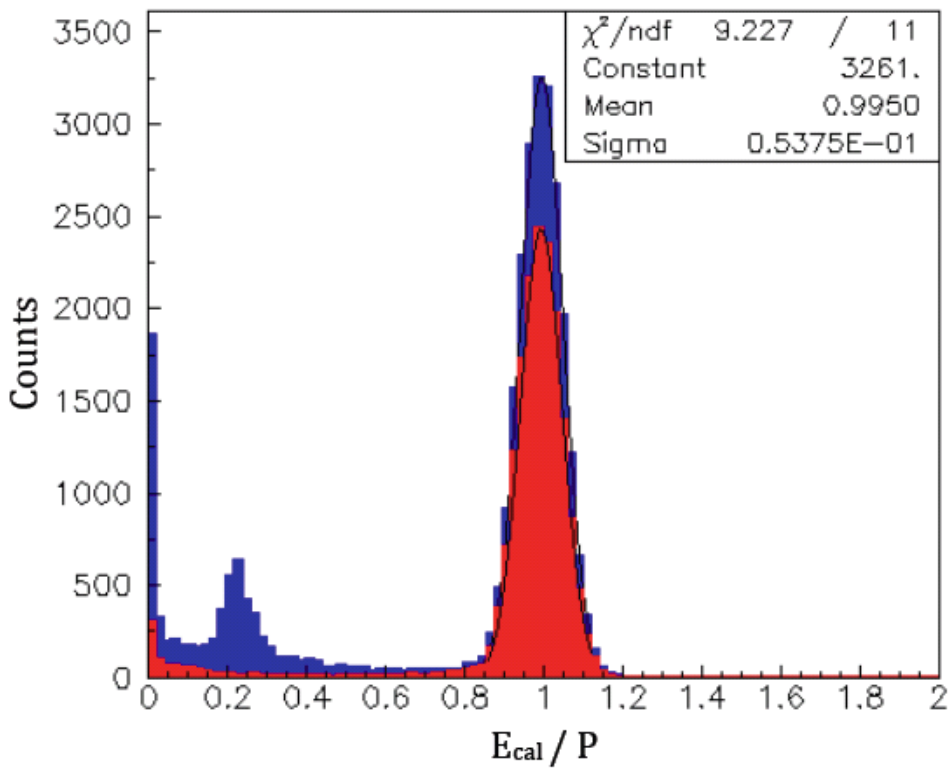

Figure 3.2: The ratio of calorimeter deposited energy E_{cal} to momentum P (Blue), showing electron peak at E_{cal}/P 1. After applying Čerenkov photoelectron cut (Red), pion signal is greatly reduced [19].

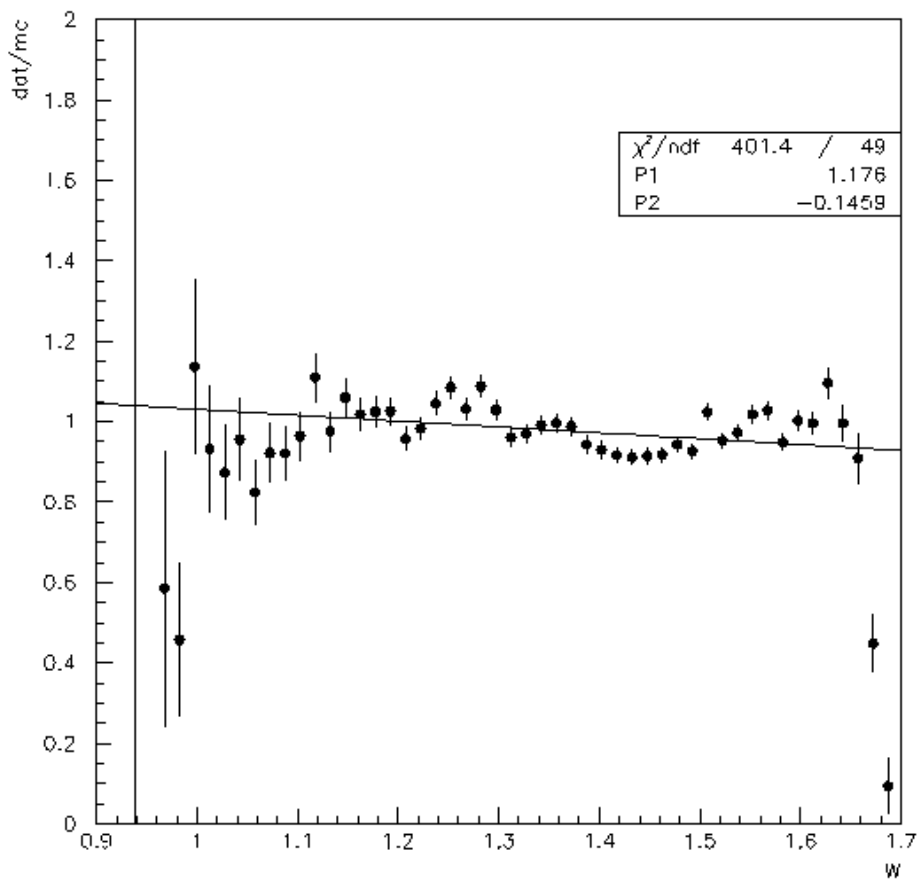

Figure 3.3: Data/MC ratio of Run 73014, assuming 59.4% packing fraction.

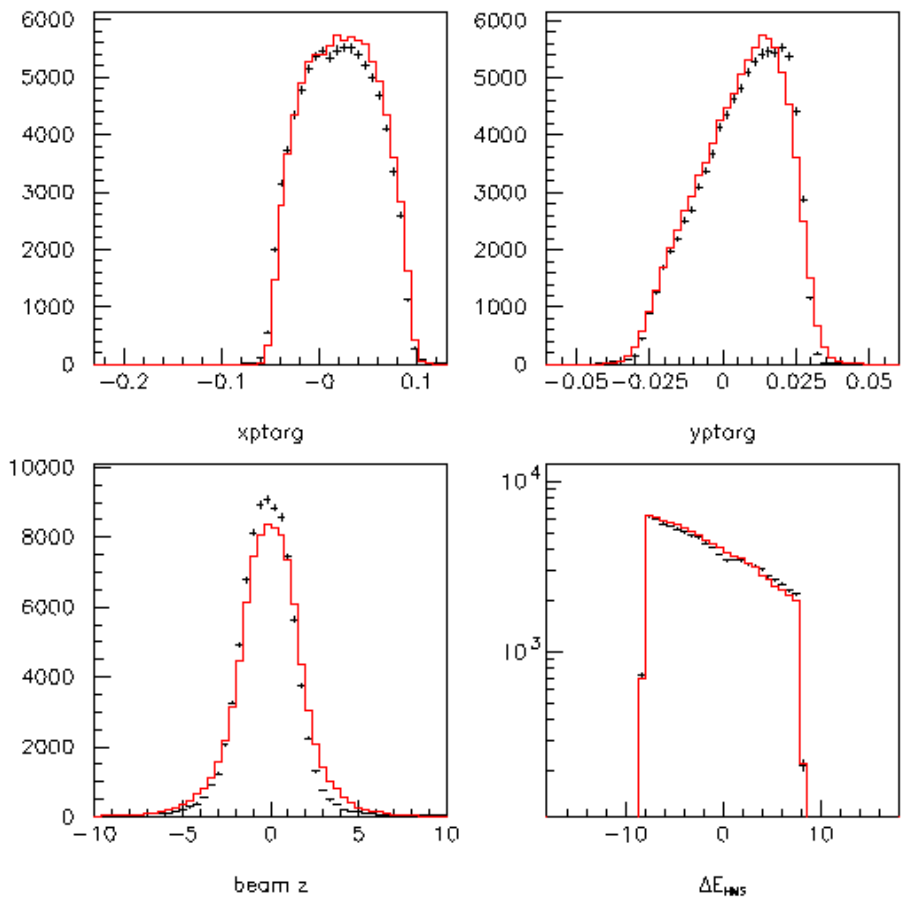

Figure 3.4: Reconstructed beam position of Run 73014, points are data and red line is MC, (From top left, clockwise) X'_{tar},Y'_{tar},δ,and Z_{beam}.

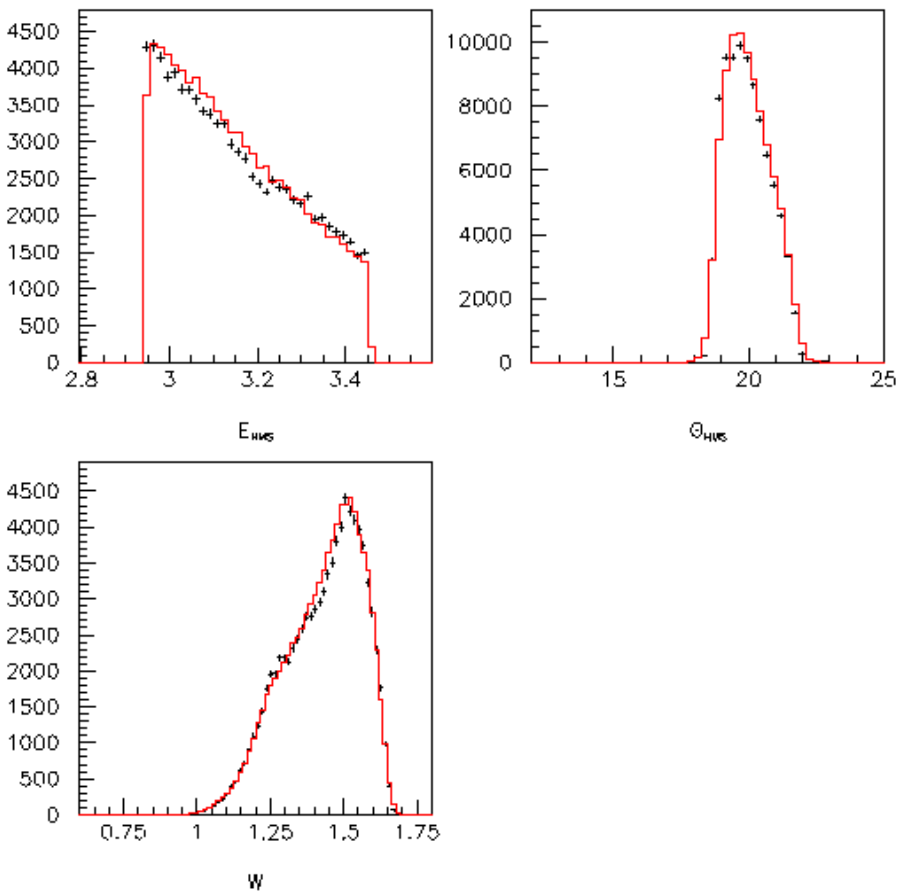

Figure 3.5: Energy and angle of scattered electron of Run 73014, points are data and red line is MC, (From top left, clockwise) Energy, scattering angle, and W measured at HMS.

to the total yield of HMS Y_T,

$$Y_T = I_b A_{hms} \left(\frac{\rho_{NH_3}}{M_{NH_3}} 3pf(3\sigma_1 + \sigma_{14}) + \frac{\rho_{He}}{M_{He}} 3(1-pf)\sigma_4 \right. \tag{3.3}$$

$$\left. + \frac{\rho_{He}}{M_{He}} z_{He}\sigma_4 + \frac{\rho_{Al}}{M_{Al}} z_{Al}\sigma_{27} \right), \tag{3.4}$$

where I_b is the beam current and A_{hms} is the HMS acceptance. So, Y_T is a linear function of pf,

$$Y_T = mpf + b, \tag{3.5}$$

with the slope m and intercept b. Therefore, if a Monte Carlo simulation can generate the HMS yield assuming certain packing fraction, this function can be obtained. And by comparing it with the data yield, packing fraction of specific target cell can be determined. Practically, a Monte Carlo simulation based on an empirical fit of inelastic cross section [25] is used. It is called Hall C HMS single arm MC. It contains correct HMS structure and magnetic field maps, and even radiative correction. The unpolarized cross sections assuming targets of 50% and 60% packing fraction is obtained from the MC. It gives m and b of Eq. (3.5). Then the yield of actual data decides the packing fraction of the target cell. Total eight ammonia target cells were used in SANE, due to the target life was limited by radiation damage. Each target cell has different packing fractions. Technical details are the same as the method used in RSS experiment [66].

At first, runs with carbon target is compared with data, as a reference. It gives weight factor to data/MC. Carbon runs' data/MC ratio is in the range of $0.867477 \sim 1.03192$, according to the kinematic range. It is usually lower at perpendicular target field runs than parallel. Run 73014, for example, is used to get the packing fraction of the insert B, material # 10. The data/MC ratio in Fig. 3.3 shows overall agreement of Data and MC. To avoid its fluctuation, the

selection of the stable W region in data/MC plot was tried, but showing almost same result within error bar. The error is estimated by 5 % of Y_T/m, studied in Ref. [66]. Fig. 3.4 and 3.5 shows that data reconstruction is well established and MC mimics it well. Of course, every MC data is corrected by total charge of beam, dead time, and tracking efficiency.

Table 3.1 is the list of packing fraction and its calculation. There are runs with the same material, but having different HMS setting: # 2 - (72213,72278), # 13 - (72247,72281), # 8& 5 - (72658,72790), # 5& 6 - (72672,72795), # 3 (72828,72957), # 9 (72984,73019), # 10 (72991,73014) (Target material number - (Runs using the same target)). They agree each other within error bars. Experiment and MC result show good enough agreement to determine the packing fractions. Overall, SANE packing fractions are 56 - 62 % with 4.5 % point error.

Also Both BETA and HMS total yields are proportional to the obtained packing fractions. Unlike HMS having different central momentum and angle, the BETA yield in the same beam energy and target field direction should be proportional to the packing fraction. Also, some packing fractions are calculated using SIMC, another Hall C MC, as a cross-check. The obtained packing fraction by this independent study agrees very well with this work [19]. The packing fraction of the same material is averaged out to the final official packing fraction. It is used in the BETA data analysis also.

3.3 Dilution Factor

As seen above, the packing fraction measurement is to get the dilution factor. MC yield assuming the obtained packing fraction can be classified according to the recoiled material, or the nucleus that the electron is scatted by. The left panel of Fig. 3.6 shows the W spectrum of the dilution factor. According to

Table 3.1: Packing fractions of each run, C is the data/MC of reference carbon run, Ydata is the yield of data, Ymc50(60) the MC yield assuming pf of 50(60)%, m is the slope and b is the intercept.

Run#	C	Y_{data}	Y_{mc50}	Y_{mc60}	m	b	pf	error
72213	0.8675	182612	154601	176787	221860	43671	0.626	0.0412
72247	0.8675	93341	79551	90833	112817	23142.4	0.622	0.0414
72278	0.9520	357790	319639	359001	393620	122829	0.597	0.0454
72281	0.9520	455353	405312	458155	528430	141097	0.595	0.0431
72658	0.9333	232893	209182	234720	255380	81492	0.593	0.0456
72672	0.9333	232978	214514	240090	255760	86634	0.572	0.0455
72790	0.9803	115049	105666	116458	107920	51706	0.587	0.0533
72795	0.9803	123604	115433	127973	125400	52733	0.565	0.0493
72828	0.8675	332739	297932	339271	413390	91237	0.584	0.0402
72957	0.9822	326976	291949	330787	388380	97759	0.590	0.0421
72959	0.9822	315150	283400	319627	362270	102265	0.588	0.0435
72984	0.9408	603843	508959	582642	736830	140544	0.629	0.0410
72991	0.9408	556527	485503	553661	681580	144713	0.604	0.0408
73014	1.0319	88392	80670	89930	92600	34369.8	0.583	0.0477
73019	1.0319	142414	127061	141092	140310	56906	0.609	0.0507

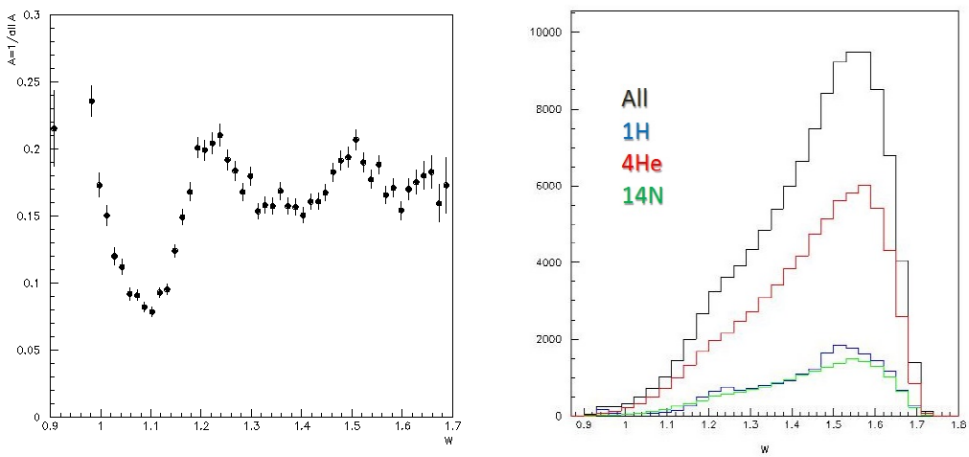

Figure 3.6: (Left) Dilution factor W spectrum in the resonance region, with target material # 10 of 59.4 % packing fraction, (Right) MC yield from each nucleus, black is total yield and blue the proton.

its HMS setting, the measured data is in the resonance region. It makes large variation of dilution factor, for proton yield based on unpolarized cross section shows clear resonances, while other material's resonances are smeared out due to the Fermi motion [67].

Unlike resonance region, DIS region dilution factors are almost just constant throughout the W range, for it has no resonance. The left panel of Fig. 3.7 is the W spectrum of the dilution factor in DIS region. The right panel shows almost flat yield along W for all materials. These dilution factors are applied into each W bin of the asymmetries.

Fig. 3.8 and 3.9 show the asymmetries along W before and after applying dilution factor. If you neglect region of W less than $1.1GeV$, where is neglected

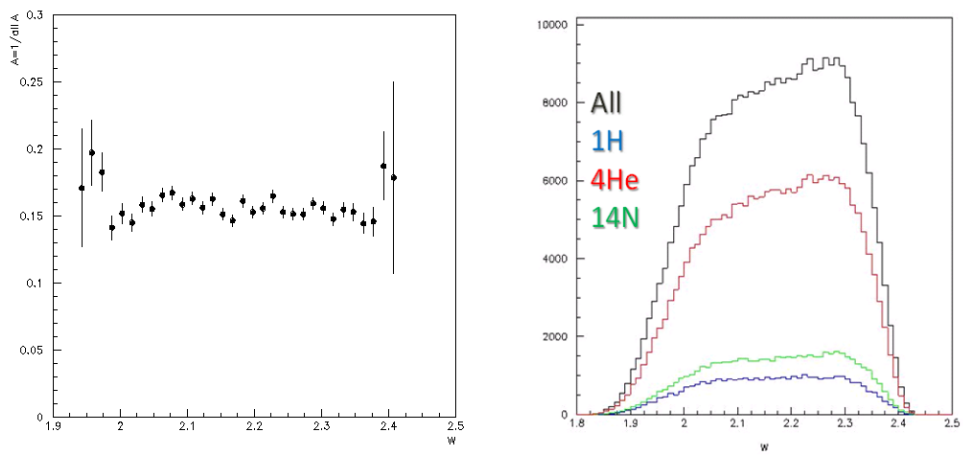

Figure 3.7: (Left) Dilution factor W spectrum in the DIS region, with target material # 2 of 58.8 % packing fraction, (Right) MC yield from each nucleus, black is total yield and blue the proton.

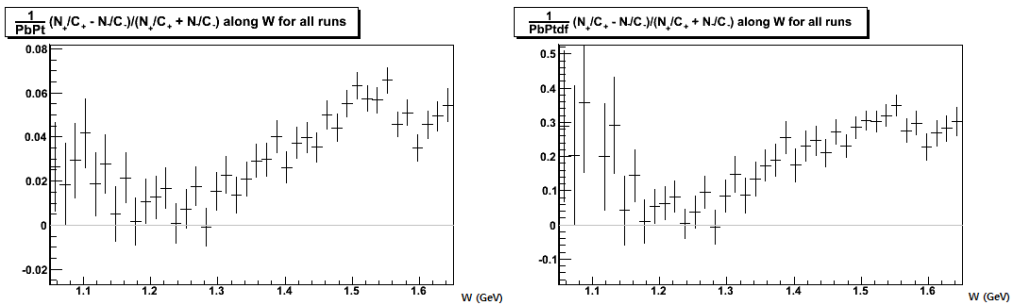

Figure 3.8: (Left) Before applying dilution factor, and (Right) After applying it. The data is parallel asymmetry result.

for this thesis due to huge error, overall trends are not changed at all. So, the resonance peaks are observed even before dilution factor. In these plots, asymmetries are already charge-normalized, dead time corrected, and Nitrogen polarization corrected.

3.4 Dead Time

Dead time of each helicity should be corrected in asymmetries. It is based on the scaler information, counts of each helicity. Unfortunately, the positive helicity scaler was not connected to the DAQ accidentally. Only total scaler and negative helicity scaler were written. It was expected that the subtraction negative scaler from total was positive scaler, but this estimation was not accurate. Although total scaler counts continuously, transition time switching negative to positive helicity scaler prevent this estimation.

One method to solve this problem is tried. The estimation of the transition time of helicities is directly related to the coefficient A of the equation $(positive\ scaler) = A \times (total\ scaler) - (negative\ scaler)$. The coefficient A

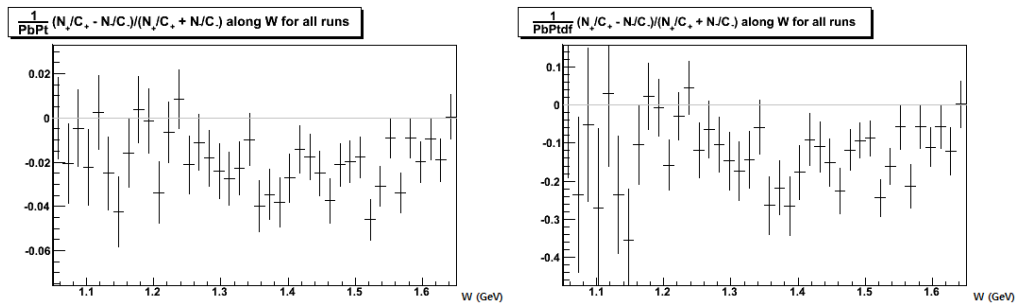

Figure 3.9: (Left) Before applying dilution factor, and (Right) After applying it. The data is near-perpendicular asymmetry result.

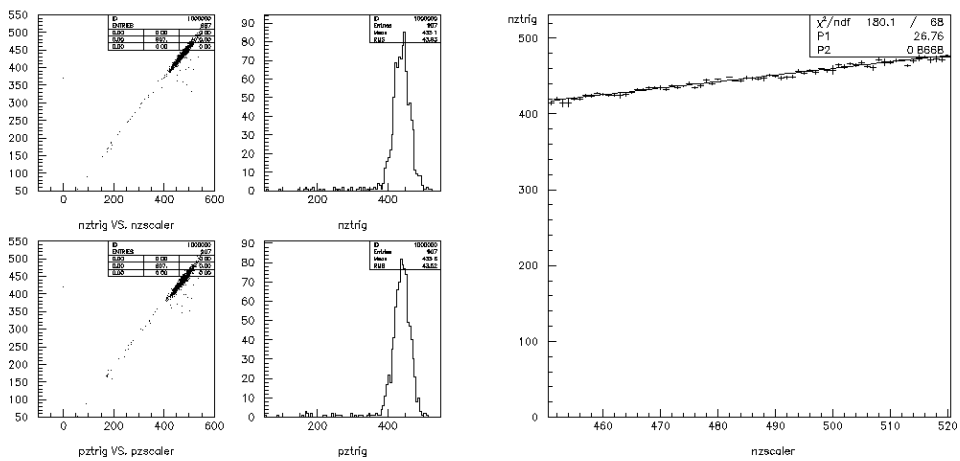

Figure 3.10: (Left) Trigger versus scaler for each helicity of Carbon run 73009, showing linear correlation, although positive scaler is estimated one, (Right) linear fit of negative trigger versus scaler.

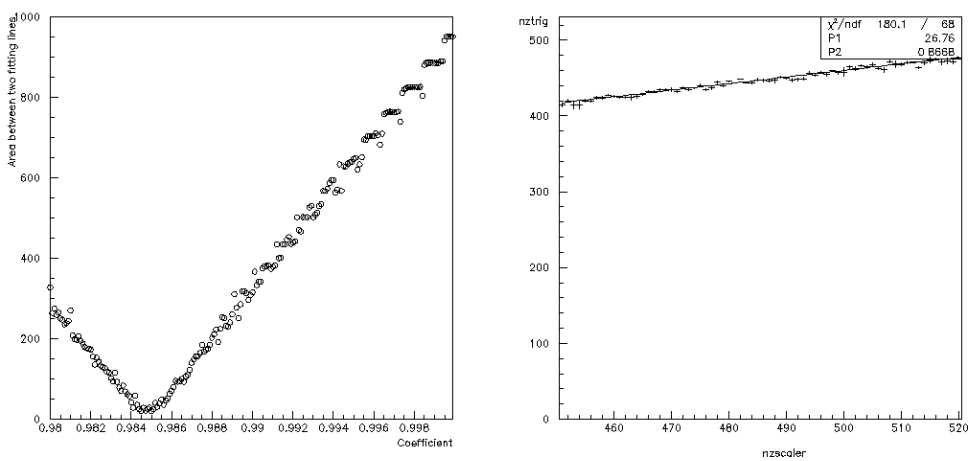

Figure 3.11: (Left) Trigger versus scaler for each helicity, showing linear correlation, although positive scaler is estimated one, (Right) linear fit of negative trigger versus scaler.

is expected to be 0.985, for 1.5% of time is required by the switching. But, some packet of beam could be supplied during the interval, so the event was recorded only in total scaler, not in positive or negative scalers. Thus, A must be calculated again. To get the correct coefficient, it is assumed that the trend of positive trigger vs. positive scaler should be similar to that of negative trigger vs. negative scaler, and that positive scaler can be reconstructed by $A \times (total\ scaler) - (negative\ scaler)$ with proper coefficient A. Fitting negative trigger vs. negative scaler for the region with high statistics can give a reference line to compare with positive trigger vs. reconstructed positive scaler.

Scanning the coefficient from 0.98 to 1.00, positive trigger-helicity plots are compared with negative helicity fit. The left panel of Fig. 3.11 is the plot of area between negative fitting line and positive fitting line. And the right panel is χ^2/ndf of two fitting lines, such that observed value is positive fitting line and expected value is negative one. Both plots have the minimum between 0.984 and 0.985, and it is a good estimation of A. This coefficient is the same with the expected A using zero asymmetry assumption, for carbon run should have no spin asymmetry. But this method can be extended to ammonia runs.

3.5 Nitrogen Polarization

In this experiment, only hydrogen in the target is expected to be polarized, for DNP process use a certain frequency of microwave, only for proton. But nitrogen atom in ammonia can be polarized also. If so, the nitrogen cross section will contribute to the asymmetries. And it is calculable. However its contribution is really small. Nitrogen contains a third of the polariable nucleons, but its polarization is about a sixth of the hydrogen's polarization. Since one third of the nucleons in the nitrogen nucleus is anti-aligned to the spin of nucleus [68].

So, the maximum contribution from the nitrogen 2% . This contribution is small enough for SANE's accuracy. Though C_N is estimated using the same method with RSS, the difference of result is almost negligible.

3.6 Asymmetry Calculation

Before applying radiative correction, it is necessary to get correct physics asymmetries A_1 and A_2, because they are the fits to iterate for radiative correction. As SANE measured near-perpendicular asymmetry, not exact perpendicular, Eqs. (1.13) and (1.14) cannot be used. If the kinematics are exactly same for both parallel and near-perpendicular asymmetry measurement, the following equation is enough to convert near-perpendicular asymmetry A_{80° to perpendicular $A_\perp$:

$$A_\perp = \frac{A_{180^\circ}\cos 80^\circ + A_{80^\circ}}{\sin 80^\circ}, \tag{3.6}$$

where A_{180° is $A_\parallel$, since SANE's magnet rotated 180° for parallel measurement.

When the kinematics of two measurement is different, Eq. (3.6) is just an approximation. For the resonance region measurement of HMS, parallel and near-perpendicular measurement had different setting, having the same Q^2 and Bjorken x. Parallel runs had 4.7 GeV beam energy, with HMS central momentum of 3.2 GeV/c and angle of 20.2°. But near-perpendicular runs had 5.9 GeV beam energy, with HMS central momentum of 4.4 GeV/c and angle of 15.4°. It was a clever kinematic matching, because CEBAF experienced a failure at the time of parallel measurement, so it could not deliver 5.9 GeV beam, but 4.7 GeV. Both of them have average Q^2 of 1.863 GeV^2. Actually, W, Q^2, Bjorken x, and ν are almost same. Even each W bin has almost completely same kinematic values. If the coefficients like D and ξ in Eq. (1.13) are calculated using only one

kinematic setting (either parallel or perpendicular setting), the asymmetries do not change much.

But it is should be precise as much as possible. Thus, the asymmetry calculation has been done by this different kinematics. Based on the definition of Ref. [24], the relation between (A_{180}, A_{80}) (for simplicity, omitting $^\circ$) and (g_1, g_2) is given by

$$A_{180} = \frac{-D'_{180}}{F_{1,180}}[-\frac{E_{180} + E'_{180}\cos\theta_{180}}{E_{180} - E'_{180}}g_1 + \frac{Q^2_{180}}{(E_{180} - E'_{180})^2}g_2] \quad (3.7)$$

$$A_{80} = \frac{-D'_{80}}{F_{1,80}}[-\frac{E_{80}\cos 80^\circ + E'_{80}(\sin\theta_{80} cos\phi_{80}\sin 80^\circ + \cos\theta_{80}\cos 80^\circ)}{E_{80} - E'_{80}}g_1 \quad (3.8)$$

$$+\frac{2E_{80}E'_{80}(\sin\theta_{80}\cos\phi_{80}\sin 80^\circ + \cos\theta_{80}\cos 80^\circ - \cos 80^\circ)}{(E_{80} - E'_{80})^2}g_2], \quad (3.9)$$

where $E_{180(80)}$ is the beam energy of parallel (near-perpendicular) setting, and other variables are defined by the same way, and

$$D' = \frac{1-\epsilon}{1+\epsilon R(Q^2, x)}. \quad (3.10)$$

Keeping track of all variables bin-by-bin according to the setting, the asymmetries are transformed to the spin structure functions. Then, they are linear combination of physics asymmetries. Reverse calculation is done by getting inverse matrix. And error propagation follows that matrix. Detailed formulae and algebra are in Appendix A.

3.7 Radiative Correction

Successful determination of dilution factor and beam and target polarization finally makes it possible to get real asymmetries. HMS covers three major kinematic regions at four-momentum transfer Q^2 of 0.8, 1.3, and $1.9 GeV^2$. These regions have both parallel and near-perpendicular asymmetry data, so can be

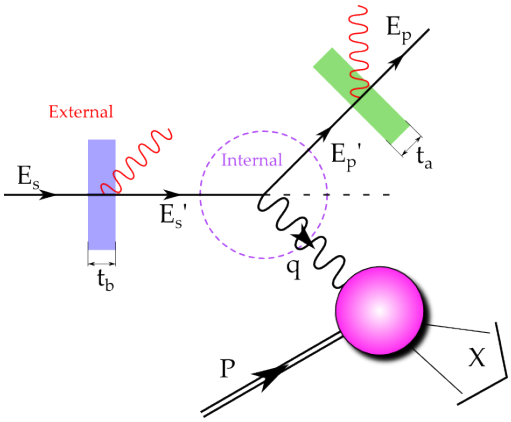

Figure 3.12: Illustration of radiative correction [17].

used to determine physics asymmetry and spin structure functions. After dividing raw asymmetries by beam and target polarization and dilution factor, it also requires radiative correction: the incoming and outgoing electron lose energy before and after scattering (external radiative correction), and elastic tail should be subtracted, and QED processes other than Born also contribute. It is illustrated in Fig. 3.12.

Radiative correction uses code based on POLRAD [69]. Basically, the methodology follows Ref. [70], a method established in a SLAC experiment on the resonance region. It uses fits of A_1 and A_2. An fit of certain model is assumed as real Born level asymmetry as a starting point. Then it is corrected using POLRAD to restore the real. The difference between corrected one and the original fit is regarded as the amount of correction, so that it is added to the real data. This radiative-corrected data is refitted to iterate until it converges. The χ^2 between (data)+(correction) and (fit) is observed during iteration. Both χ^2 and fitting parameters should be converged. The fit is a mix of Breit-Wigner (BW) type resonance terms and a polynomial with correction factors depending on

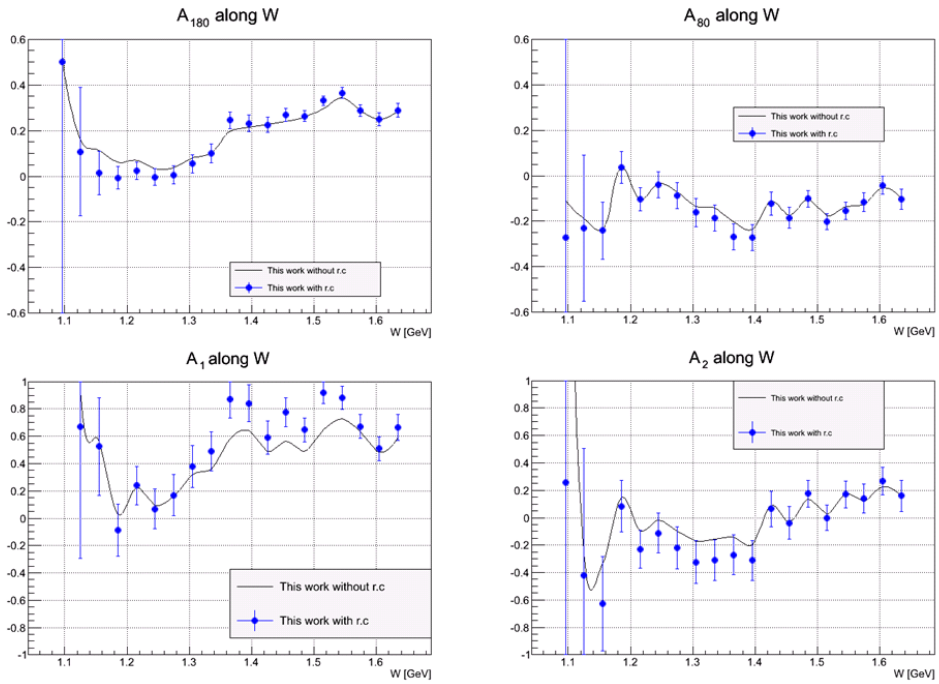

Figure 3.13: The asymmetries and physics asymmetries radiative correction applied, solid line is before radiative correction, and circles are after radiative correction.

Q^2. A_1 has three BW terms, while A_2 two BW. Both fits have DIS tail, which is modified polynomial of Bjorken x. The detailed form of the fitting function is in Appendix B. The goodness of fit is $\chi^2/ndf = 0.74(1.20)$ for $A_1(A_2)$. Actual fitting was performed using Minuit [71]. But it is not only fit to use. JLab CLAS fits and MAID fits [72] are also used to get radiative correction. Its model dependence is included in systematic uncertainty.

Fig. 3.13 shows the resonance region asymmetries, before and after radiative correction. Radiative correction generally makes the peaks more clear, because

Table 3.2: The fitting parameters of A_1 and A_2. a_i is the amplitude, ω_i is the centroid, and g_i is the width of the i-th BW peak.

Parameter	A_1 Fit	A_2 Fit
a_1	-0.553 ± 0.204	-0.306 ± 0.152
a_2	0.724 ± 0.267	-0.474 ± 0.210
a_3	0.615 ± 0.071	–
ω_1	1.186 ± 0.016	1.232 (fixed)
ω_2	1.381 ± 0.006	1.323 ± 0.010
ω_3	1.547 ± 0.012	–
g_1	0.031 ± 0.025	0.070 ± 0.057
g_2	0.053 ± 0.036	0.058 ± 0.035
g_3	0.197 ± 0.068	–

it reduces processes other than Born.

3.8 Fitting and Error

The fitting is not only for the radiative correction, but also for identification of the resonances. Although complete distinguishing of resonances are not possible without in-depth knowledge of final states such as semi-inclusive measurement, it is still useful to compare the peaks with known resonances. Table 3.2 shows the fitting parameters and errors. Both asymmetries have DIS tail from RSS results [5], for our kinematic range does not cover DIS region. These fitting parameters are converged, after the iterations of radiative correction. As an initial trail, σ_{TT} and σ_{LT} were fitted to get reasonable centroids and width, though its amplitude became huge. Then the σ_{TT} and σ_{LT} fits were served as the initial parameters for A_1 and A_2 respectively.

Table 3.3: The external error matrix of the A_1 fit, with row and column index follows the order of the Table 3.2. Each matrix element $\times 10^{-3}$ is the real.

a_1	a_2	a_3	ω_1	ω_2	ω_3	g_1	g_2	g_3
42.300	-0.155	-0.003	1.040	0.000	0.001	1.410	0.047	-0.026
-0.155	75.400	4.240	0.053	-0.438	-0.140	-0.557	-8.510	4.760
-0.003	4.240	5.080	-0.013	0.004	-0.494	0.013	-0.372	-2.980
1.040	0.053	-0.013	0.251	0.000	-0.001	-0.106	-0.022	0.006
0.000	-0.438	0.004	0.000	0.032	-0.003	0.004	0.086	-0.142
0.001	-0.140	-0.494	-0.001	-0.003	0.145	0.005	-0.013	0.528
1.410	-0.557	0.013	-0.106	0.004	0.005	0.642	0.152	-0.065
0.047	-8.510	-0.372	-0.022	0.086	-0.013	0.152	1.300	-1.270
-0.026	4.760	-2.980	0.006	-0.142	0.528	-0.065	-1.270	4.850

A_2 fit was hard to get, due to its broad negative peak. At first only one BW resonance was tried, and it converged well. But, this broad peak was not satisfactory, especially for we knew that there is $\Delta(1232)$ resonance. However, two BW peaks were not stabilized after radiative correction. Alternatively, peak center of $\Delta(1232)$ is now fixed at $W = 1.232GeV$. This fit converges well. After fixing Δ peak, Minuit finds another peak at $W = 1.323 \pm 0.010GeV$. It might be the appearance of low mass pole of $\Lambda(1405)$, which is recently reported in electroproduction by CLAS Collaboration [73], which is related to whether it is quasi-bound state or not.

Table 3.3 and 3.4 are the external error matrices of the fitting parameters. It is observed that the correlation between other BW peak is suppressed. These error matrices are used to get fitting error propagation. From it, g_1 and g_2 fits with error are obtained. And integration error propagation is also possible, which is essential to get d_2.

Table 3.4: The external error matrix of the A_2 fit, with row and column index follows the order of the Table 3.2. Each matrix element $\times 10^{-3}$ is the real.

a_1	a_2	ω_2	g_1	g_2
23.400	3.470	-0.061	5.700	0.143
3.470	44.700	0.820	2.340	5.200
-0.061	0.820	0.108	-0.011	0.162
5.700	2.340	-0.011	3.400	-0.452
0.143	5.200	0.162	-0.452	1.230

These A_1 and A_2 fits are evaluated at $Q^2 = 1.9GeV^2$ in Fig. 3.14. The red bands in the plot is the error band, which is calculated using numerical derivative of each parameter and the error matrix. They matches with data well, if we consider that DIS tail is fixed.

3.9 Measured Asymmetries to Others

It is worth to check the contribution of parallel (A_{180}) and near-perpendicular (A_{80}) asymmetries on the physics asymmetries and structure functions. Eqs. (1.21) and (1.22) are relatively simple to extract A_1 and A_2 from measured asymmetries. Our experiment, however, measured near-perpendicular asymmetry A_{80} instead of exact perpendicular asymmetry $A_\perp$. So, the relation formulae is a bit complicated. Complete equations are in the Appendix A.

We can define a matrix to transform the measured asymmetries to physical variables. The matrix C is for $(A_1, A_2) = C(A_{180}, A_{80})$. And the matrix D is for $(g_1, g_2) = D(A_{180}, A_{80})$. It means the following relation:

$$\begin{pmatrix} A_1 \\ A_2 \end{pmatrix} = \begin{pmatrix} C_{11} & C_{12} \\ C_{21} & C_{22} \end{pmatrix} \begin{pmatrix} A_{180} \\ A_{80} \end{pmatrix} \tag{3.11}$$

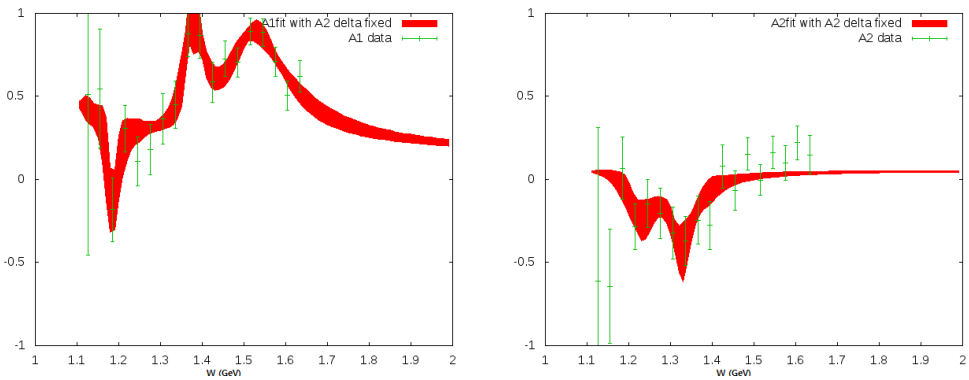

Figure 3.14: (Left) A_1 fit evaluated at at $Q^2 = 1.9GeV^2$ with the actual data points, (Right) A_2.

In the same way, D matrix is defined. Their entries are in the Table 3.5. Both A_{180} and A_{80} affect much on A_1 and A_2. But, A_{180} dominates the contribution on g_1, and A_{80} on g_2. One order difference on the D matrix elements makes these results. Each contribution is plotted in Figs. 3.15 and 3.16.

3.10 Systematic Uncertainty

SANE-HMS asymmetries has systematic uncertainties as in Table 3.6.

The beam polarization is measured by Møller polarimeter of Hall C. Its accuracy is high enough as studied in Ref. [57]. Its statistical error is less than one percent for five minute measurement. And the systematic error is just 0.47 %. Møller measurement, however, cannot be done simultaneously with the production runs. So, the measurement was analysed with accelerator status parameters. All of the measurements was fitted with these parameters. The fit has three degrees of freedom: the polarization at the source, the degree of

Table 3.5: Matrix elements of the transformation from (A_{180}, A_{80}) to (A_1, A_2) and (g_1, g_2), i.e. $(A_1, A_2) = C(A_{180}, A_{80})$ and $(g_1, g_2) = D(A_{180}, A_{80})$.

	C				D			
$W(GeV)$	C_{11}	C_{12}	C_{21}	C_{22}	D_{11}	D_{12}	D_{21}	D_{22}
1.095	1.5826	-2.2007	2.0173	2.7772	0.0048	0.0012	0.0002	0.0057
1.125	1.6152	-2.1441	2.0129	2.7642	0.0236	0.0056	0.0012	0.0284
1.155	1.6555	-2.0796	2.0178	2.7377	0.0671	0.0155	0.0036	0.0805
1.185	1.6900	-2.0113	2.0123	2.7087	0.1453	0.0325	0.0081	0.1739
1.215	1.7013	-1.9493	1.9760	2.6935	0.2026	0.0448	0.0117	0.2472
1.245	1.7026	-1.8849	1.9277	2.6773	0.1886	0.0417	0.0113	0.2359
1.275	1.7093	-1.8143	1.8847	2.6521	0.1648	0.0361	0.0102	0.2101
1.305	1.7179	-1.7545	1.8449	2.6403	0.1598	0.0348	0.0102	0.2085
1.335	1.7299	-1.6973	1.8088	2.6316	0.1685	0.0365	0.0111	0.2248
1.365	1.7382	-1.6487	1.7704	2.6346	0.1830	0.0397	0.0125	0.2512
1.395	1.7540	-1.5989	1.7399	2.6336	0.2024	0.0437	0.0143	0.2843
1.425	1.7777	-1.5605	1.7179	2.6502	0.2332	0.0502	0.0171	0.3359
1.455	1.8222	-1.5368	1.7153	2.6914	0.2956	0.0633	0.0225	0.4358
1.485	1.8760	-1.5283	1.7214	2.7597	0.4172	0.0892	0.0330	0.6326
1.515	1.8767	-1.4768	1.6784	2.7518	0.4560	0.0974	0.0375	0.7116
1.545	1.8302	-1.3896	1.5958	2.6717	0.3911	0.0833	0.0335	0.6275
1.575	1.8109	-1.3230	1.5399	2.6211	0.3770	0.0794	0.0337	0.6196
1.605	1.8224	-1.2815	1.5117	2.6132	0.4105	0.0851	0.0384	0.6909
1.635	1.8503	-1.2590	1.4977	2.6426	0.4860	0.0995	0.0479	0.8425

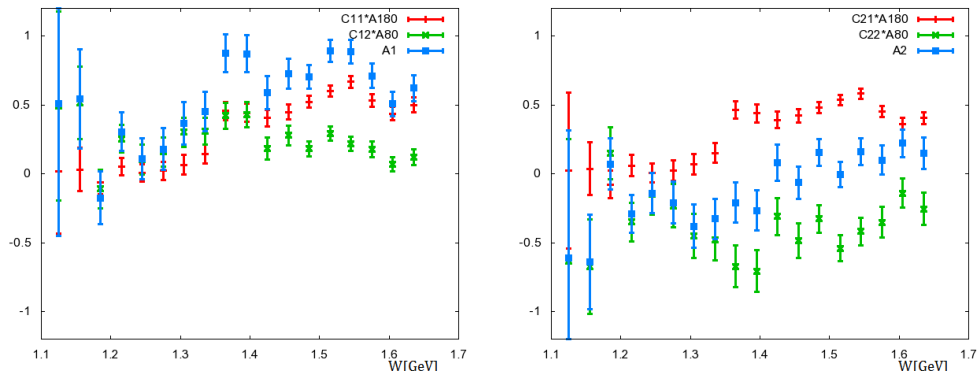

Figure 3.15: (Left) A_1 as a sum of $C_{11}A_{180}$ and $C_{12}A_{80}$, (Right) A_2 as a sum of $C_{21}A_{180}$ and $C_{22}A_{80}$

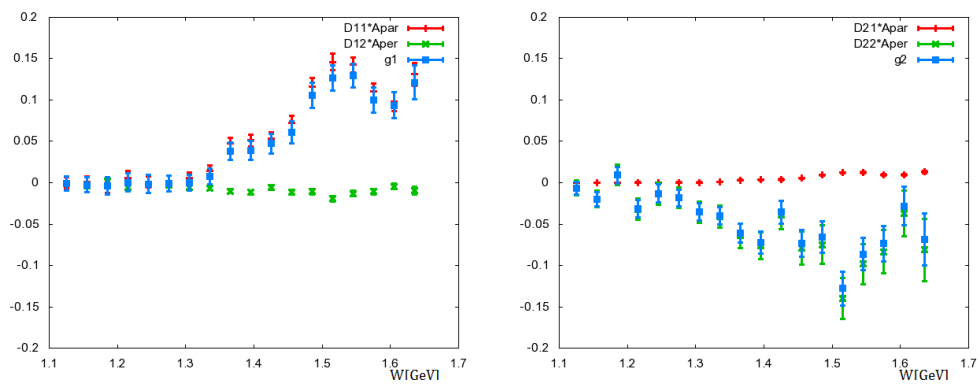

Figure 3.16: (Left) g_1 as a sum of $D_{11}A_{180}$ and $D_{12}A_{80}$, (Right) g_2 as a sum of $D_{21}A_{180}$ and $D_{22}A_{80}$

Table 3.6: Average systematic errors in the asymmetries

Error Source	Error
Target polarization	4.0 %
Beam polarization	1.5 %
Dilution factor	3.3 %
Nitrogen correction	0.4 %
Radiative correction	$\leq$ 10 % (A_{180}), $\leq$ 19 % (A_{80})
Kinematic Reconstruction	0.5 %

imbalance between north and south linac, and a global correction to the beam energy. The global fit has χ^2/dof of 1.4, and it can be 1.06 if we abandon the anomalous measurement of number 8. The error in the beam polarization comes from this global fit. Fitting error of 0.5 % and Møller measurement error makes conservatively 1.5 % uncertainty.

The target polarization error is based on the accuracy of the calibration constants used to produce the polarization from NMR area. Because, the target polarization in thermal equilibrium is accurately known, which is $P = \tanh(\mu B/k_B T)$, the calibration constant is obtained by comparing the NMR signal with this expected polarization. The thermal equilibrium measurements (TEs) was taken at around 1.6 K. To reach this temperature, it took longer than two hours until NMR area became stable. Then, the calibration constant was repeatedly measured. One example is in Fig. 3.18. The standard deviation of the individual calibration constants for a given material sample about the mean gives a measure of the systematic error [17].

The error from dilution factor is based on the error of the packing fraction. The systematic error of packing fraction comes from normal error of MC, studied with carbon runs. For SANE carbon runs, the data/MC ratio is within 5

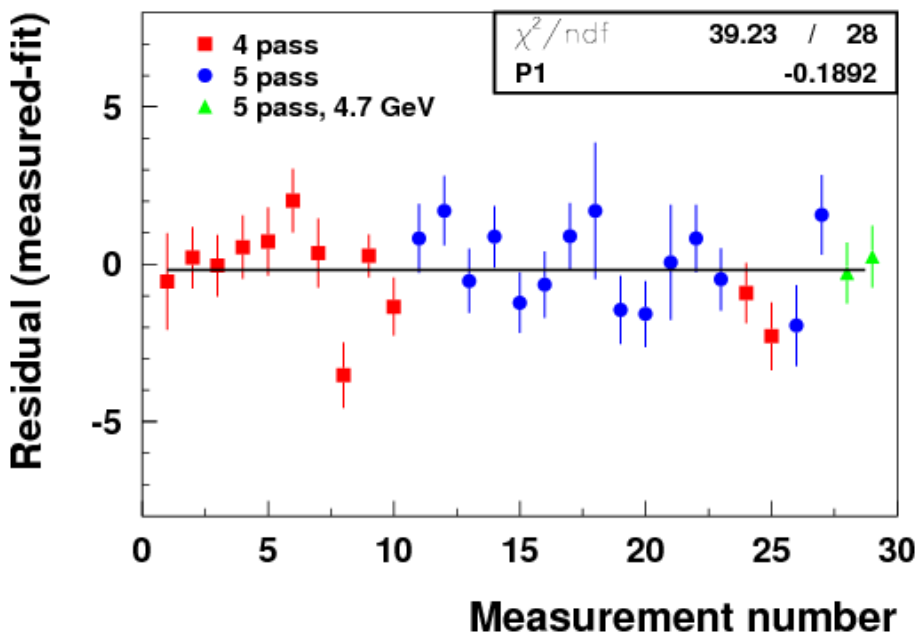

Figure 3.17: Residuals of the global fit and the Møller measurements

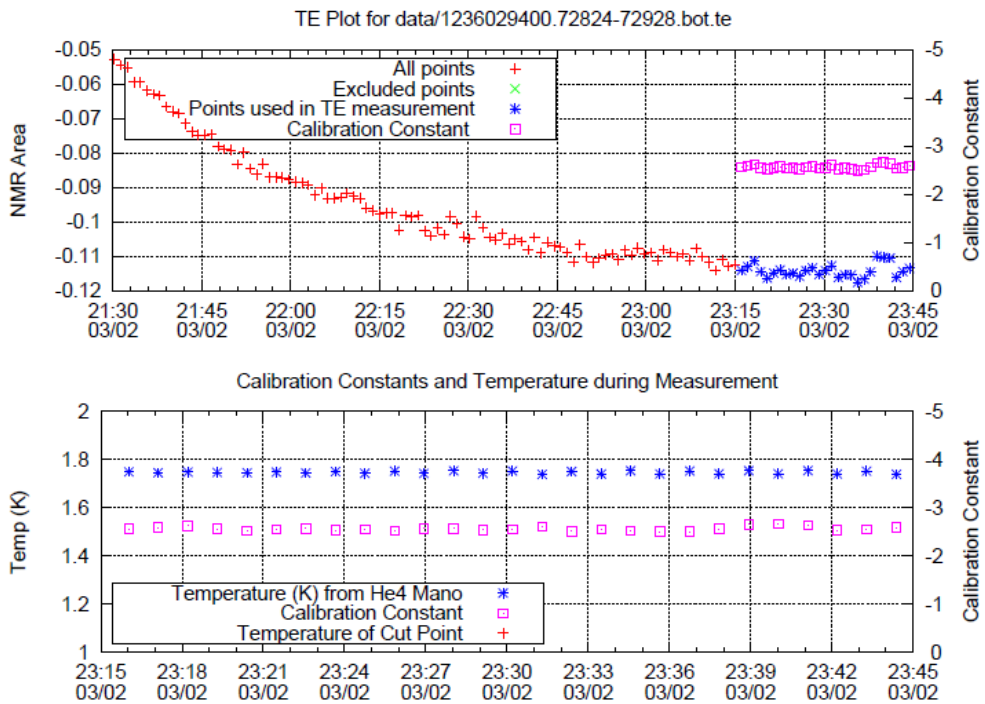

Figure 3.18: An example of thermal equilibrium measurement, showing selected points of TE (Blue stars) and corresponding calibration constants (Pink boxes) [17].

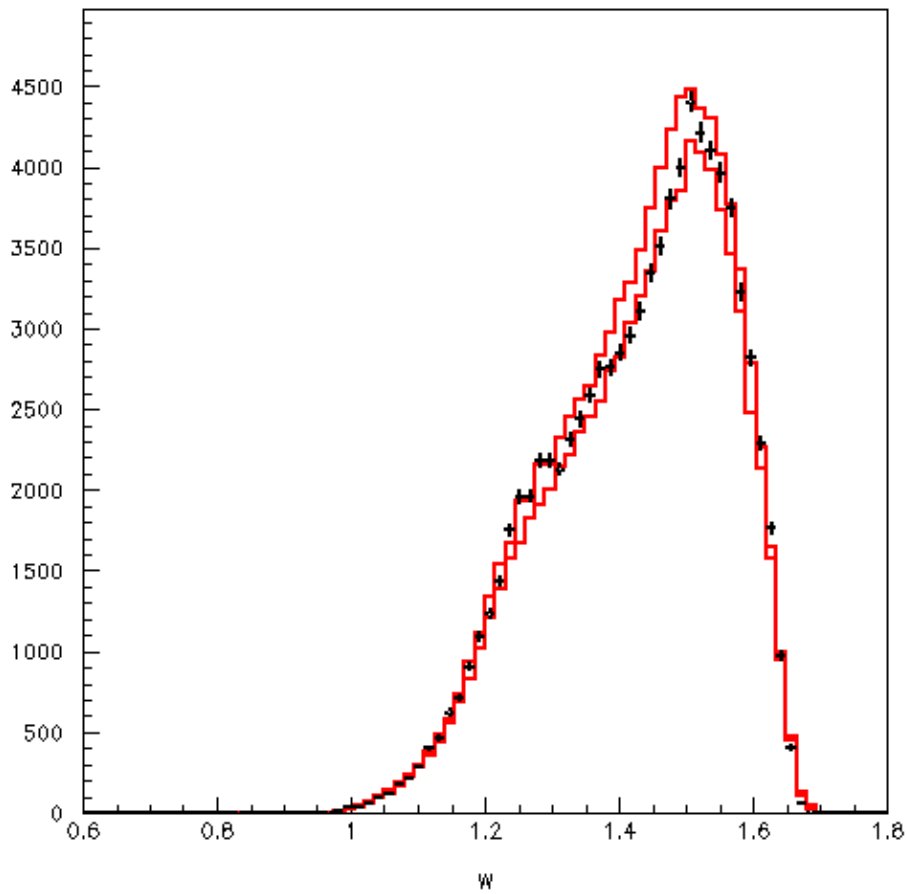

Figure 3.19: Data (points) and Monte Carlo (lines) of W assuming $59.4 \pm 4.44\%$ packing fraction. Region between two lines is within the systematic error.

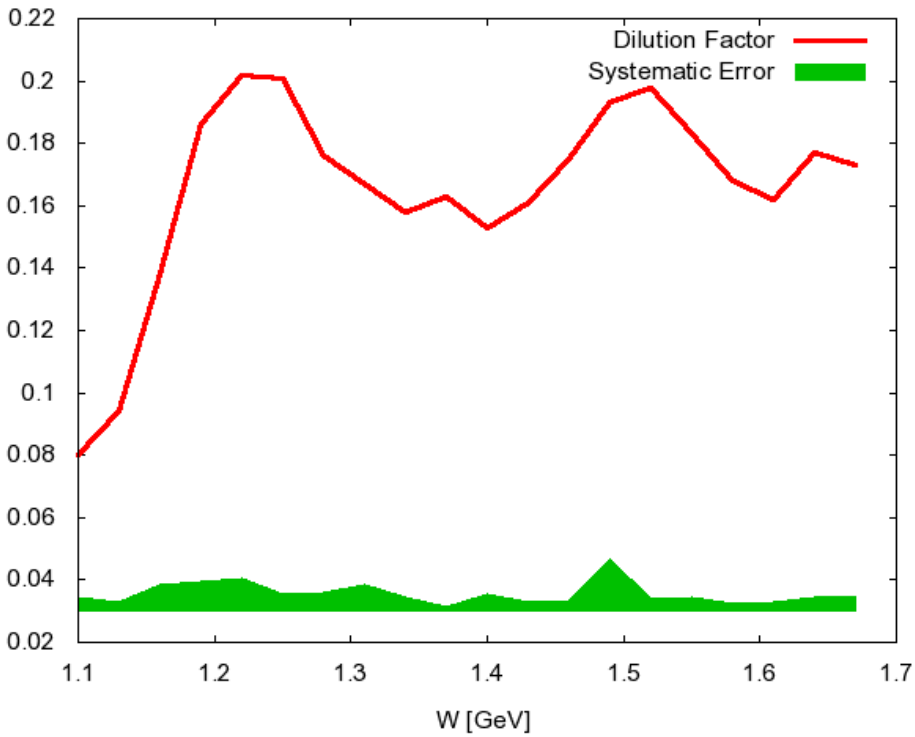

Figure 3.20: Dilution Factor of the resonance region of SANE-HMS, assuming 59.5 % packing fraction. The band below is the systematic error.

% range, agreeing with the Jefferson Lab's MC study [66]. For the resonance region, the target material had packing fraction of 59.4 ± 4.44 %. Monte Carlo simulation assuming (pf+error) % and (pf-error) % shows the systematic uncertainties, i.e. the deviation between two cases is the error. Fig. 3.19 shows the MC results along W compared with data. MC shows good agreement with data. Fig. 3.20 is the dilution factor with systematic error band. This error is propagated to the error of asymmetries, and the average error is 3.3 %.

Nitrogen correction adds minor uncertainty. The correction itself is just

tiny amount, i.e. $C_N \sim 1.01$ for $W > 1.2GeV$. It depends on the model for the nitrogen's spin states [74]. Kinematic reconstruction of HMS is another small source of uncertainty. The kinematic corrections follows a global study of the elastic measurements [75]. It said that the precisions of the kinematic settings are 5×10^{-4} for the beam energy, 5×10^{-4} for the scattered electron's energy, 0.2 $mrad$ for the angle. It is studied again with our elastic runs by A. Liyanage [19]. The effect on the asymmetry is about 0.5 %.

Systematic errors from radiative correction are calculated from deviation of fitting models used. The radiative correction uses various models ,such as Jefferson Lab Hall B (A_1 fit only) and MAID fit, to compare with our own fit. Complete list of models and their radiative correction are in the Figs. 3.23 and 3.24. The list is basically identical with one used in RSS [5]. Gaps between before and after radiative correction of each model are collected, to get standard deviation between them. It gives the systematic error from model dependence. Unlike other models, our fit iterates until fitting parameters are stabilized, and χ^2 between the radiative corrected data and our fit converges. But other fit does not iterate at all, and its radiative correction is used to estimate the model dependence. The standard deviation of radiative corrected data from all these fits are regarded as a systematic uncertainty. So, the error increases when the peak position or amplitude disagrees. Fig. 3.21 and 3.22 are the parallel and near-perpendicular asymmetries with systematic error bands. It is quite obvious that the RC uncertainty is large around $1.3GeV < W < 1.4GeV$, where the previous expectation does not match with our results. Actually, large uncertainty at the $W \approx 1.1GeV$ causes large fitting uncertainty. If we ignore that part, RC systematic error of bins $W > 1.2GeV$ is 10 % level. And error propagation gives us 10 % systematic uncertainties in A_1 and A_2, because the parallel asymmetry dominates them.

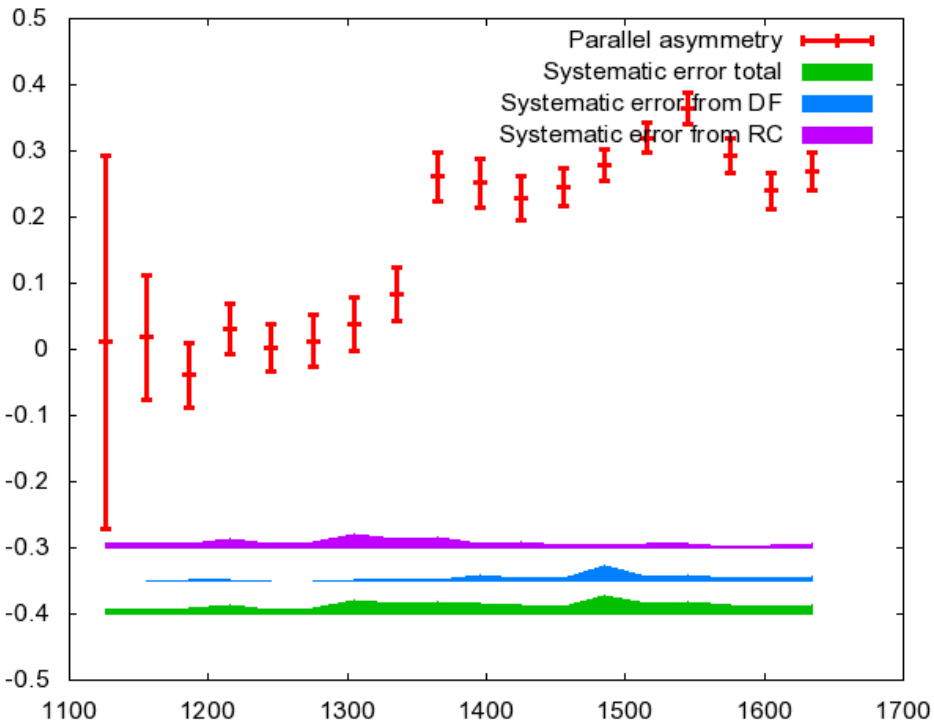

Figure 3.21: Parallel asymmetry with systematic error bands, which indicate the error of total (bottom green), from DF (middle blue), and from RC (top purple).

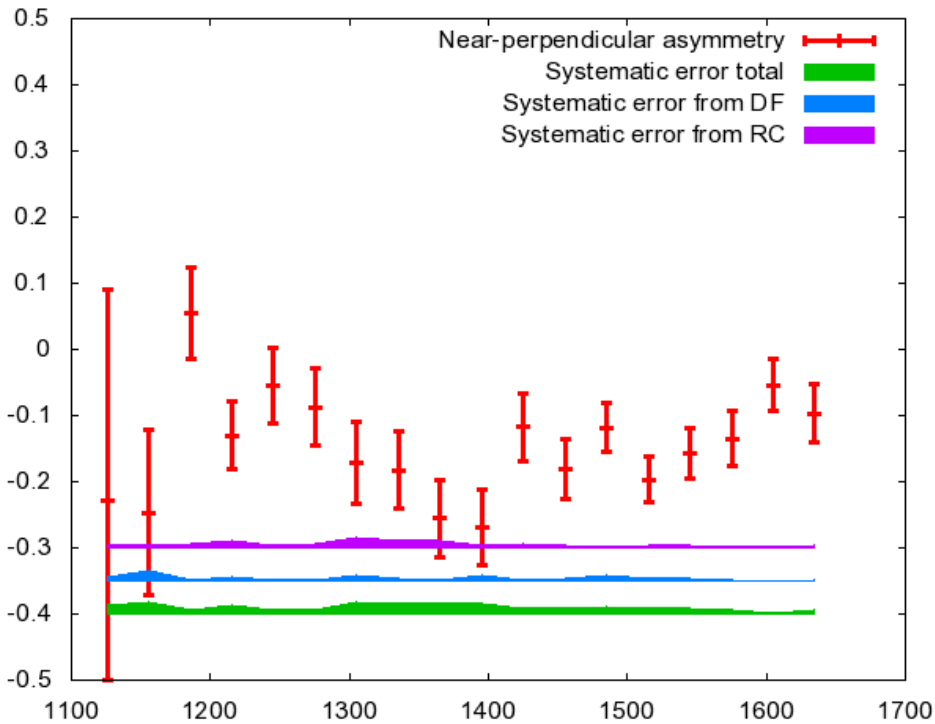

Figure 3.22: Near-perpendicular asymmetry with systematic error bands, which indicate the error of total (bottom green), from DF (middle blue), and from RC (top purple).

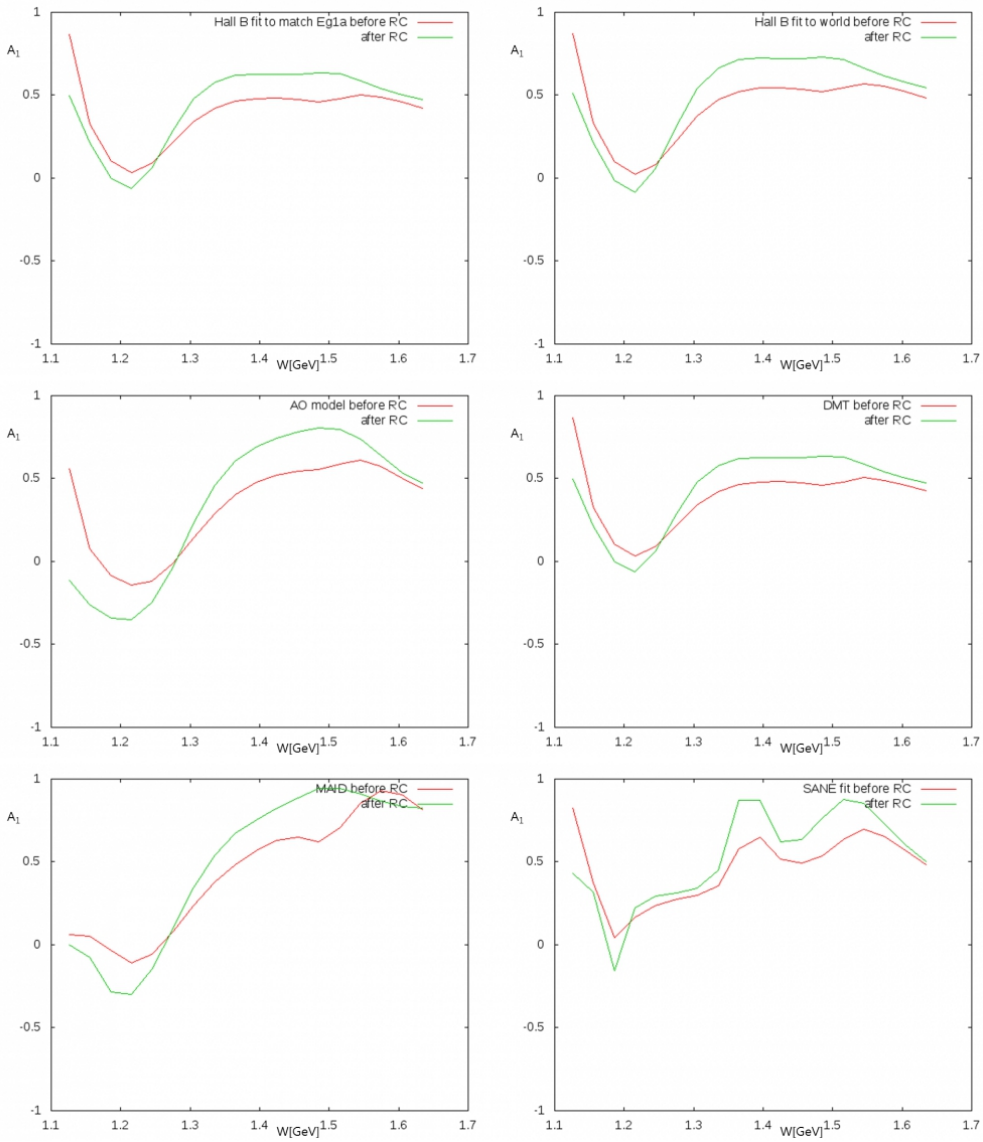

Figure 3.23: A_1 models used for systematic study, our radiative correction code transforms 'after r.c.' into 'before r.c.', to get the amount of correction.

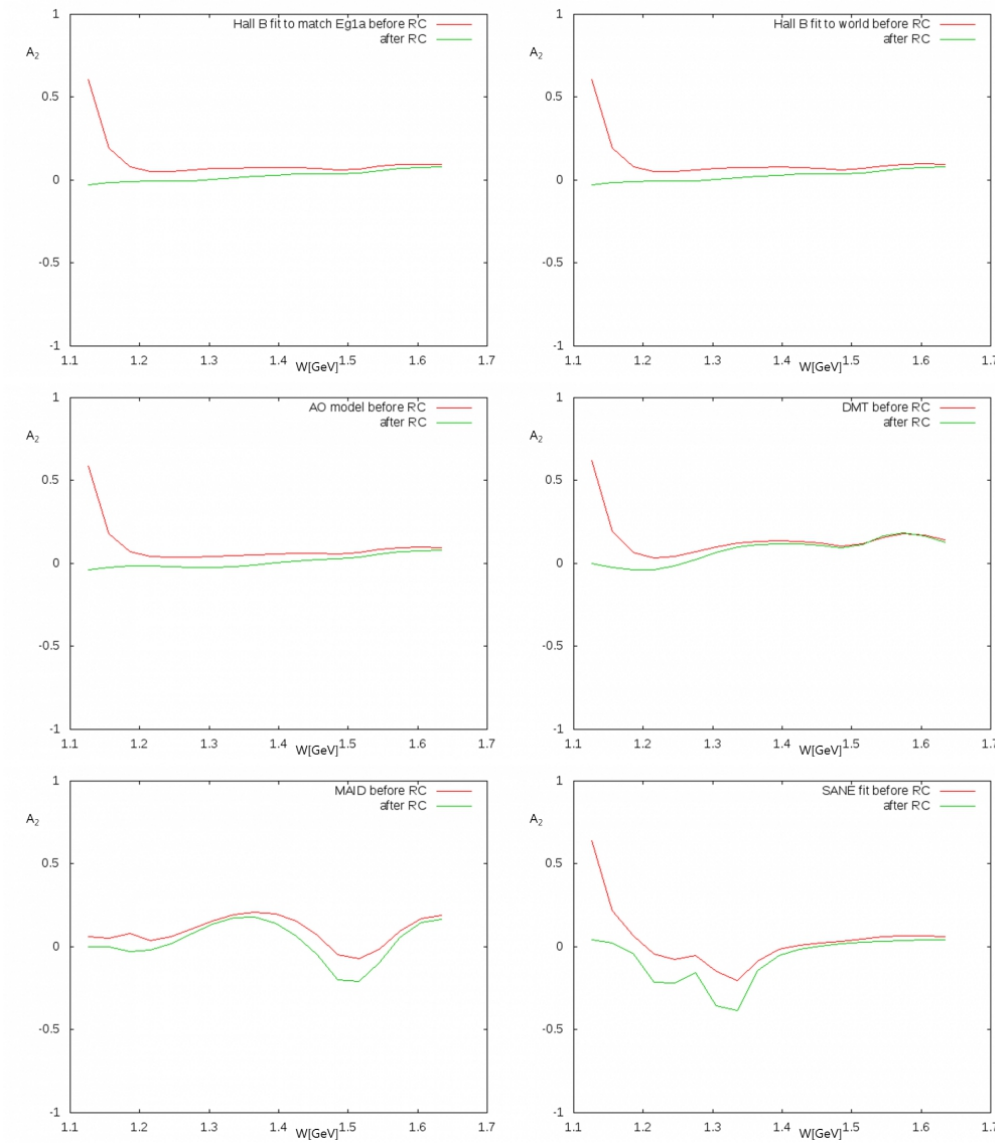

Figure 3.24: A_2 models used for systematic study, our radiative correction code transforms 'after r.c.' into 'before r.c.', to get the amount of correction.

Chapter 4

Results and Discussions

4.1 Asymmetries

The fully corrected measured asymmetries are shown in Fig. 4.1. $A_\perp$ in this plot means the near-perpendicular asymmetry A_{80}. Its overall shape is quite similar to RSS. This SANE-HMS data is the first direct measurement on the kinematics of virtual photon momentum transfer $< Q^2 >= 1.86\ GeV^2$ and invariant mass of recoiled system $1.1\ GeV < W < 1.6\ GeV$. This full corrected asymmetries can be converted to the physics asymmetries.

Fig. 4.2 shows the virtual photon absorption asymmetry A_1 along W. Fig. **??** is the virtual photon asymmetry A_1. It is consistent with CLAS results at corresponding Q^2. Fig. 4.3 puts our data with CLAS A_1 of two different Q^2 of $1.71\ GeV^2$ and $2.05\ GeV^2$. Our low W region has higher Q^2, close to $2GeV^2$, while high W region has lower Q^2, close to $1.7GeV^2$. So, the left panel plots should agree well at high W, while the right at low W, and they agree well. MAID, a theoretical prediction by empirical fits of Universität Mainz, is also in good agreement, considering that its prediction is limited especially at high W

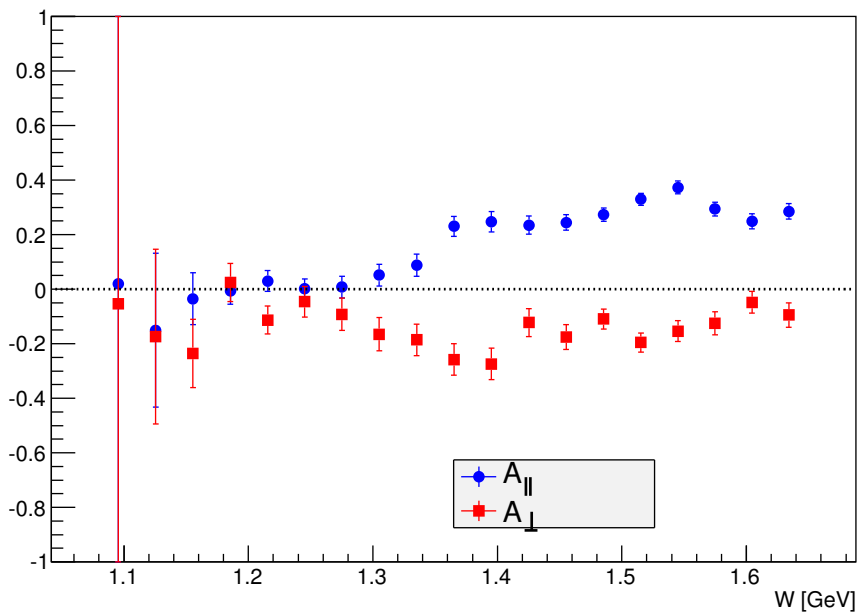

Figure 4.1: Our measured asymmetries, fully radiative corrected

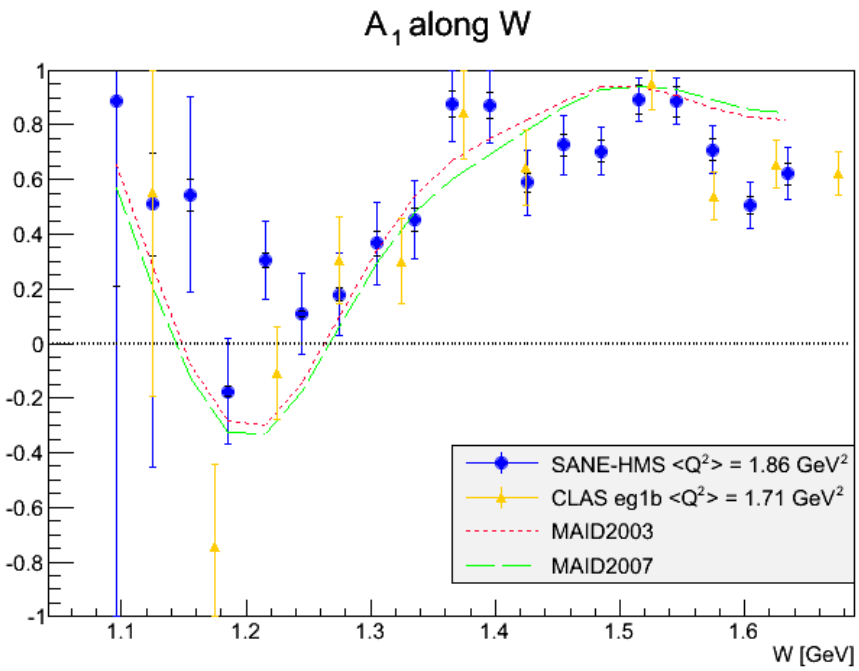

Figure 4.2: Virtual photon asymmetry A_1 from our data and CLAS experiment [20] and MAID fits [21], smaller error bar is systematic.

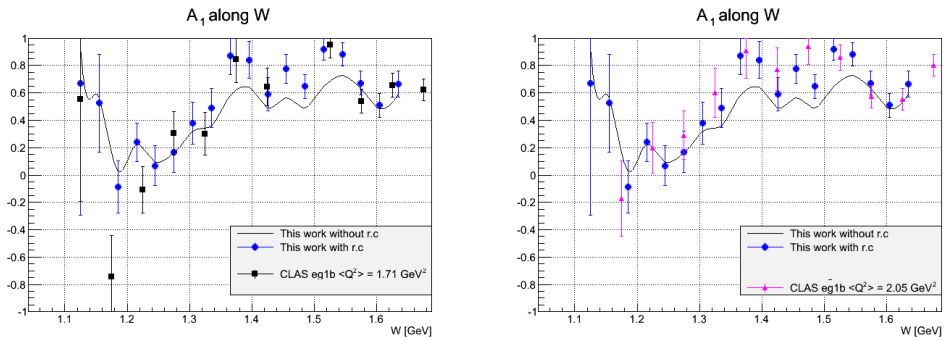

Figure 4.3: Virtual photon asymmetry A_1(smaller error bar is systematic and curve indicates data before radiative correction), comparing with (Left) CLAS data of $< Q^2 >= 1.71 GeV^2$ (Right) of $< Q^2 >= 2.05 GeV^2$ [20].

region, since it has no multi-pion channels. Cross section definitions of MAID are translated in SANE's language: $A_1 = -sigTT'/sigT$ and $A_2 = -sigLT'/sigT$, following an usual convention used in RSS and CLAS also. The reliability of A_1 (and also g_1 presented in the next section) is directly related to that of A_2 (and g_2), because A_1 and A_2 always obtained simultaneously through the same correction procedure. The agreement of A_1 with previous data is one evidence that the analysis is reliable. Fig. 4.4 shows comparison with RSS data. It has Q^2 evolution at some resonance peaks around $W \approx 1.4$ and 1.5 GeV. This observation of Q^2 dependence is confirmation of RSS and CLAS result.

The SANE-HMS data has produced the world first A_2 result at this kinematic region, as in Fig. 4.5. Previously, RSS A_2 measurement at different Q^2 is the only measurement of this resonance region, and some empirical fits exists. This data reveals the big difference at $1.2\ GeV < W < 1.4\ GeV$, although Q^2 difference between RSS and SANE-HMS is just $\approx 0.6 GeV^2$. A_2 shows un-

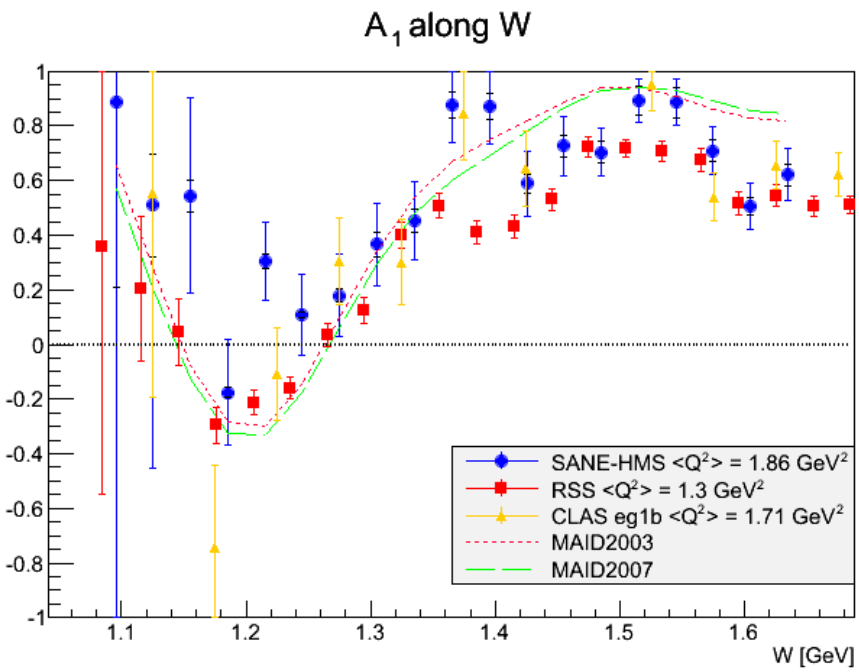

Figure 4.4: Virtual photon asymmetry A_1, comparing with RSS [5], smaller error bar is systematic.

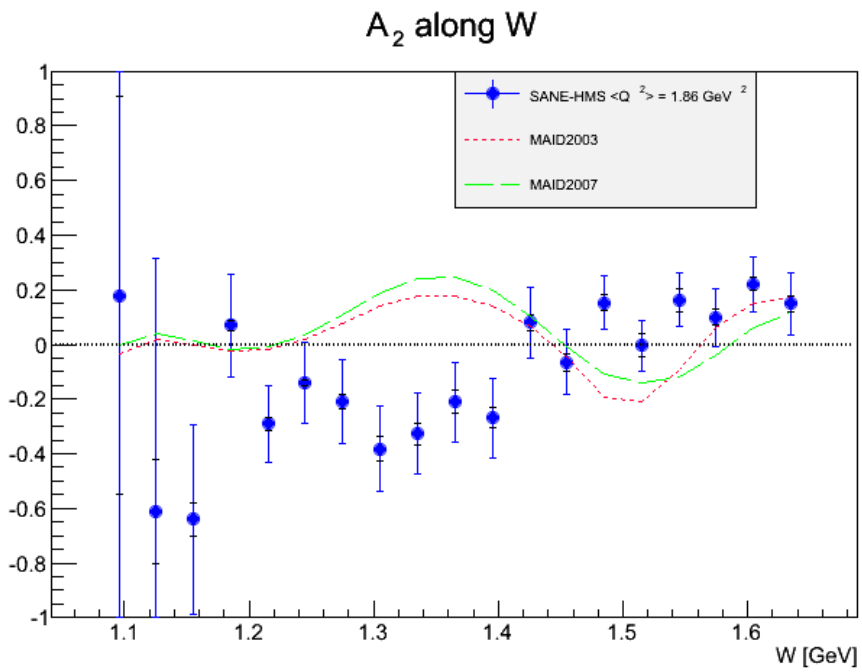

Figure 4.5: Virtual photon asymmetry A_2 from our data and MAID fits [21], smaller error bar is systematic.

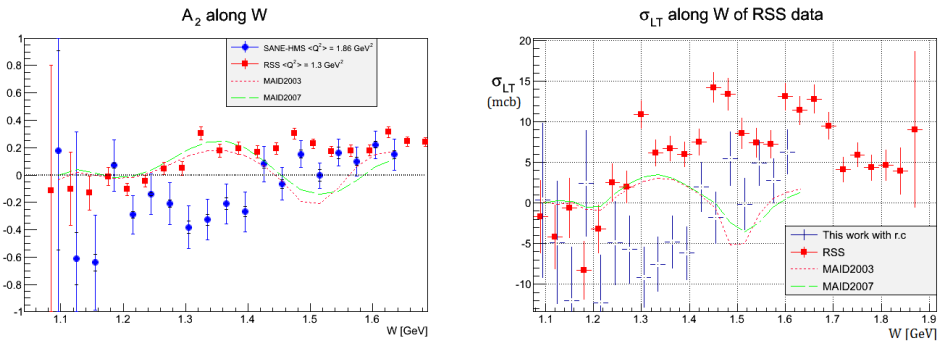

Figure 4.6: (Left) Virtual photon asymmetry A_2(smaller error bar is systematic), comparing with RSS [5], (Right) virtual photoabsorption interference term σ_{LT} with RSS and MAID [21].

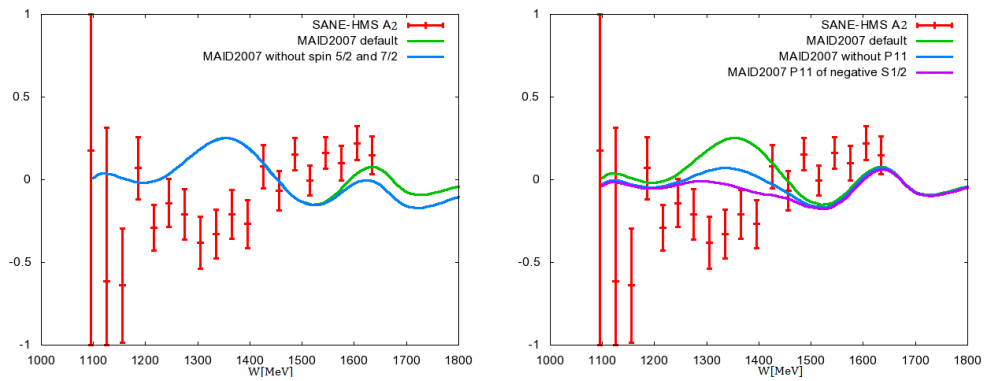

Figure 4.7: (Left) Virtual photon asymmetry A_2 from data and MAID with and without higher spin resonaces, (Right) MAID with P_{11} resonance contribution of positive, none, and negative [21].

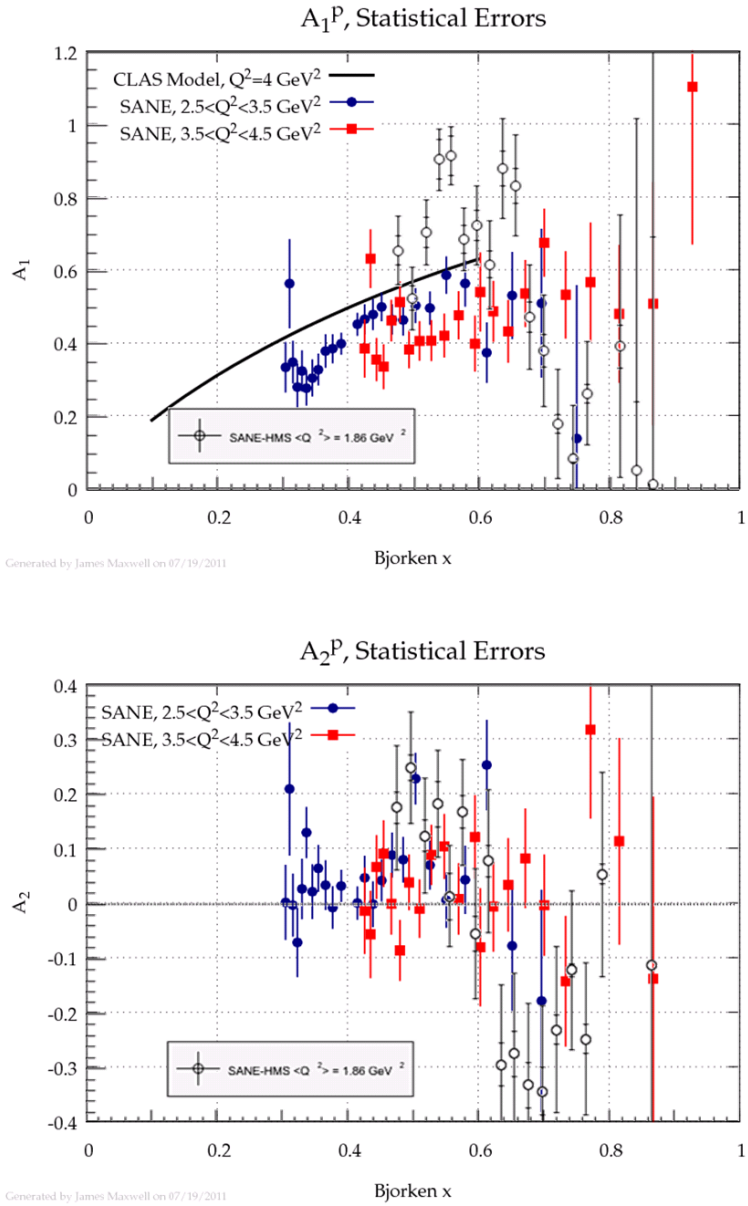

Figure 4.8: (Top) A_1 from SANE-HMS and SANE-BETA(preliminary), (Bottom) A_2 from the same, smaller error bar is systematic.

expected sign change at this region. It could be an indication of very negative transverse-longitudinal interference contribution at this resonance, since $A_2 = \sigma_{LT}/\sigma_T$ where $\sigma_{LT} = \sqrt{2}\frac{Q^2}{q*}S *_{1/2} A_{1/2}$ is the interference term between transverse and longitudinal photon-nucleon amplitudes, and σ_T is sum of both transverse photoabsorption cross section. The Left panel of Fig. 4.6 is with A_2 of RSS. Sign flip of the resonance depending Q^2 clearly appears, which MAID cannot expect.

To find the reason of this negative region, MAID was manipulated as a trial. Left plot of Fig. 4.7 shows MAID A_2 with and without higher spin resonances, such as $D_{15}(1675)$, $F_{15}(1680)$, $F_{35}(1905)$, $F_{37}(1950)$, whose spins are 5/2 or 7/2. It affects only on higher W region. Right plot of Fig. 4.7 is about P_{11} resonance. When the resonance is turned off, MAID A_2 is lowered. If we assume a negative $S_{1/2}$ for it, A_2 become even smaller at $W \approx 1.3GeV$. However, they cannot solve this significant negative result.

The right panel is σ_{LT} of both RSS and SANE, showing the sign change of σ_{LT}. Fig. 4.8 shows the speciality of this low Q^2 region data. BETA data has a few GeV^2 higher Q^2. Variation of asymmetries at $< Q^2 >= 1.9GeV^2$ is larger than that of BETA data, though HMS-BETA is very preliminary.

4.2 Spin Structure Functions

The parallel and perpendicular asymmetries can be transformed to the spin structure functions g_1 and g_2. In Fig. 4.9, g_1 shows good agreement with CLAS g_1 results. Lower x region of SANE has Q^2 around $1.7GeV^2$, higher x region of SANE has $2GeV^2$, and it agrees with CLAS data of close Q^2.

Again, SANE-HMS g_2 is the first measurement of this region, $< Q^2 >= 1.86\ GeV^2$ and $0.45 < x < 0.85$. Our g_2 in Fig. 4.10 shows significantly different

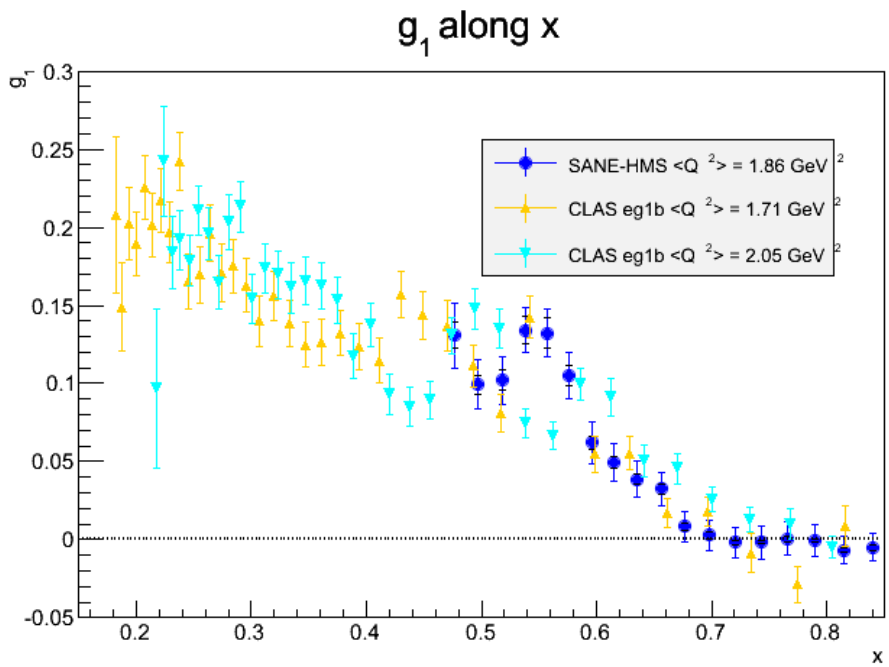

Figure 4.9: Spin structure function g_1 and CLAS with close Q^2 [20], smaller error bar is systematic.

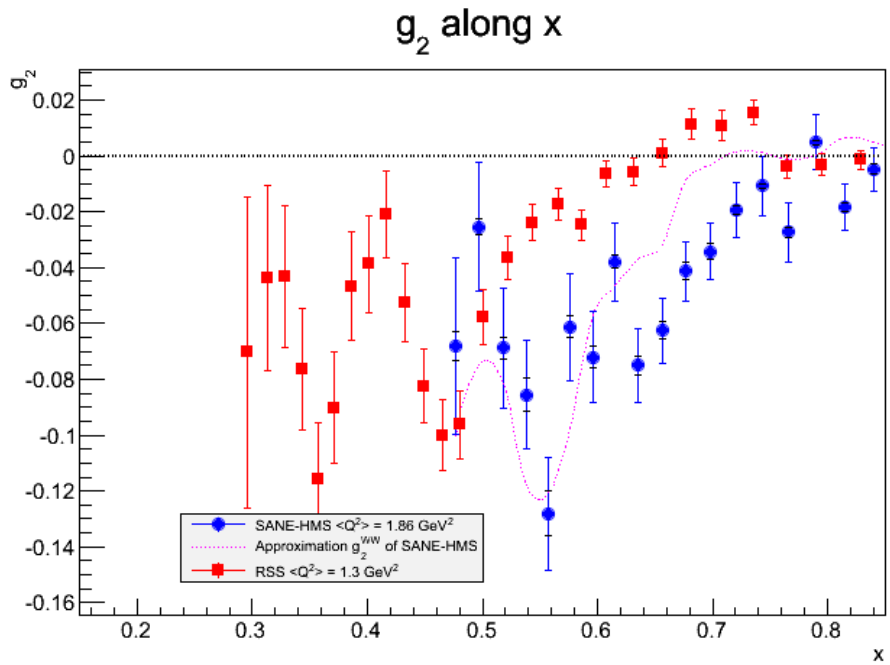

Figure 4.10: Spin structure function g_2 and g_2^{WW} from our data, smaller error bar is systematic.

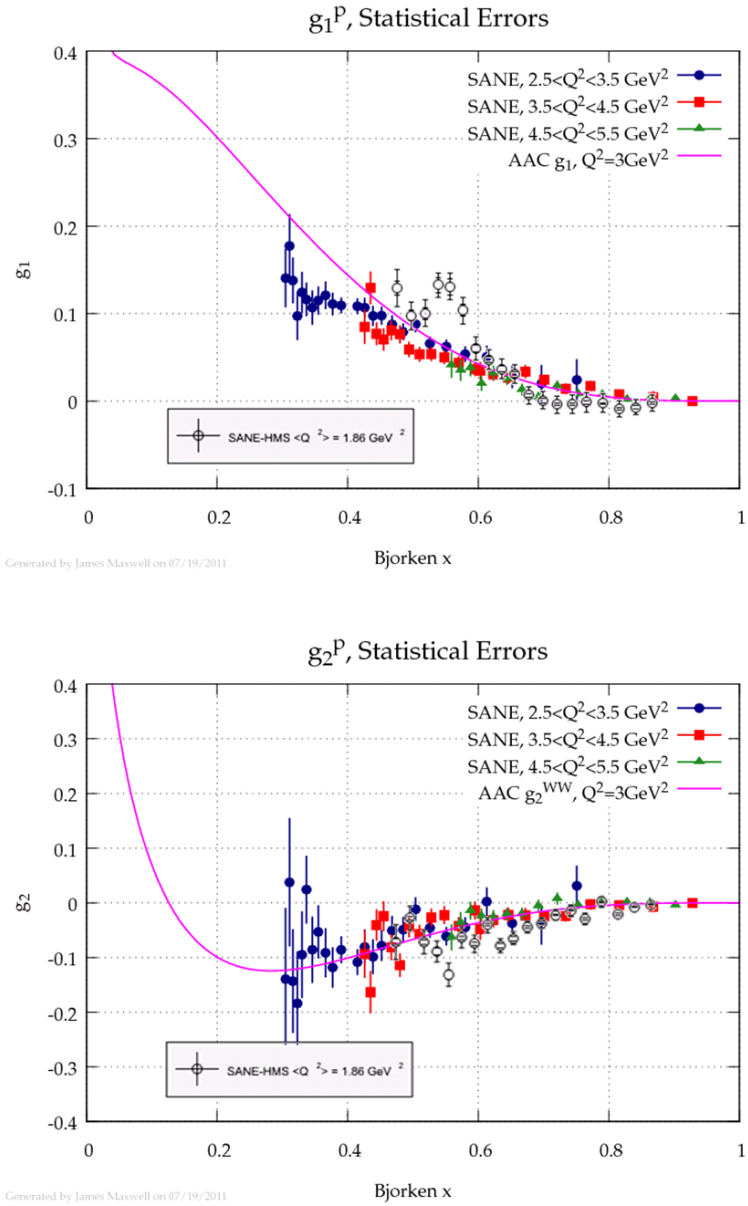

Figure 4.11: (Top) g_1 from SANE-HMS and SANE-BETA(preliminary), (Bottom) g_2 from the same, with AAC group prediction [22].

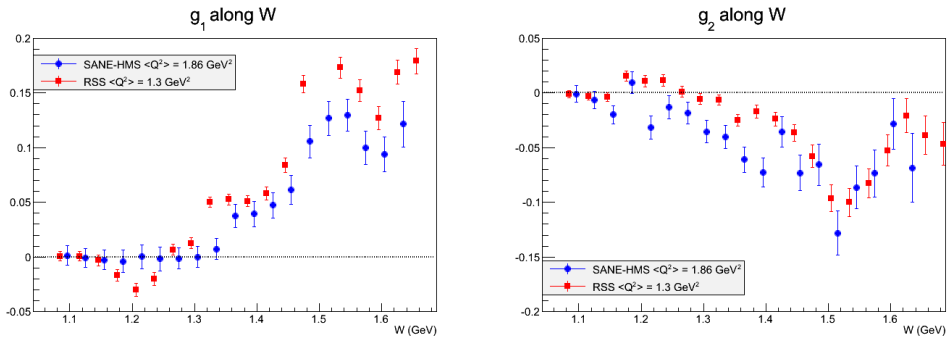

Figure 4.12: (Left) g_1, (Right) g_2 along recoiled system mass W, comparing with RSS[5].

with RSS, and it is a trivial result from A_2. It means that there is quite big changes depending on Q^2. Difference between g_2 and g_2^{WW}, obtained using our g_1, shows higher twist effect, for difference between g_2 and g_2^{WW} indicate higher twist contribution. It is suppressed then RSS [5], as SANE-HMS has higher Q^2. But still there is indication of twist-3 effect, around $x \approx 0.7$. Fig. 4.11 is the g_1 and g_2 from both HMS and BETA, though BETA result is preliminary. It shows that difference between g_2 and g_2^{WW} due to higher twist effect decreases as Q^2 grows.

Although Q^2 dependency looks too large, major part of these change is just an illusion. Higher Q^2 results in higher x for the same W. As Q^2 increases, the resonance region goes up close to $x = 1$ and is compressed. So, if we plot the structure functions along W, instead of x as usual, the difference between RSS and our result is limited in the amplitude problem of the resonances. g_1 and g_2 may not be the best language to understand the resonance region. Fig. 4.12 is the invariant mass W spectrum of the structure functions.

4.3 d_2 Matrix Element

d_2 is a measure of twist-3 contribution, which is defined as the third moment of $g_2 - g_2^{WW}$. Using a bit of calculus, it can be obtained simply using g_1 and g_2, as in Eq. (**??**). For either cases, Bjorken x^2 of the integrand makes large x region contribute much, while small x region can be neglected. Although SANE-HMS resonance data is limited in $0.47 \leq x \leq 0.87$. It is quite sufficient to calculate d_2, or at least $\bar{d_2}$ defined as a limited integration of d_2. It is calculated not from direct data points, but from fitting evaluation, because the integral of g_2^{WW} and d_2 should be done at the same Q^2 by definition. So, only fitting errors are propagated using the external error matrix. Fit itself has not much Q^2 dependency, so selection of $Q^2 = 1.9GeV^2$, an average Q^2, is good enough.

Fig. 4.13 shows the d_2 integrand and the d_2 running integral. The region of x larger than 0.8 is narrowed for BW becomes zero as it approaches to pion threshold. From this running integral, $\bar{d_2} = -0.0087 \pm 0.0014$ is obtained by integrating over $0.47 \leq x \leq 0.87$. It is the world first observed negative value of d_2. It was unexpected, for RSS d_2 at $Q^2 = 1.3GeV^2$, SLAC at $5GeV^2$, and HERMES at $10GeV^2$ all produced positive d_2. (Although HERMES d_2 is compatible with zero.) Only SANE-HMS d_2 is negative at $1.9GeV^2$.

However, there was possibility of negative d_2. Some theorists expected negative value. They are in agreement with our d_2 within error bar [8–10]. Moreover, negative d_2 comes from theory calculation at Q^2 $1GeV^2$, while the most of positive d_2 from theory at Q^2 $5GeV^2$. Revisited list of Fig. 4.15, with SANE-HMS $\bar{d_2}$, shows it clearly.

And, CLAS eg1 data analysis produced possible negative d_2 value at $2GeV^2$. Fig. 4.14 is allowing negative d_2. As CLAS cannot get perpendicular asymmetries, its A_2 and g_2 measurement is pretty much limited. But by changing kinematic variables and fitting it, it can at least constrain the range of them [23].

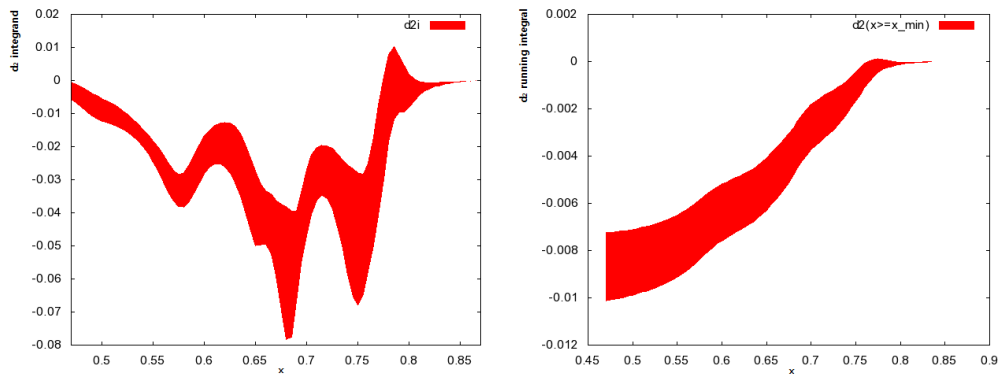

Figure 4.13: (Left) d_2 integrand $x^2(2g_1+3g_2)$, (Right) $\bar{d_2}$ integrated from lower bound x to 0.87.

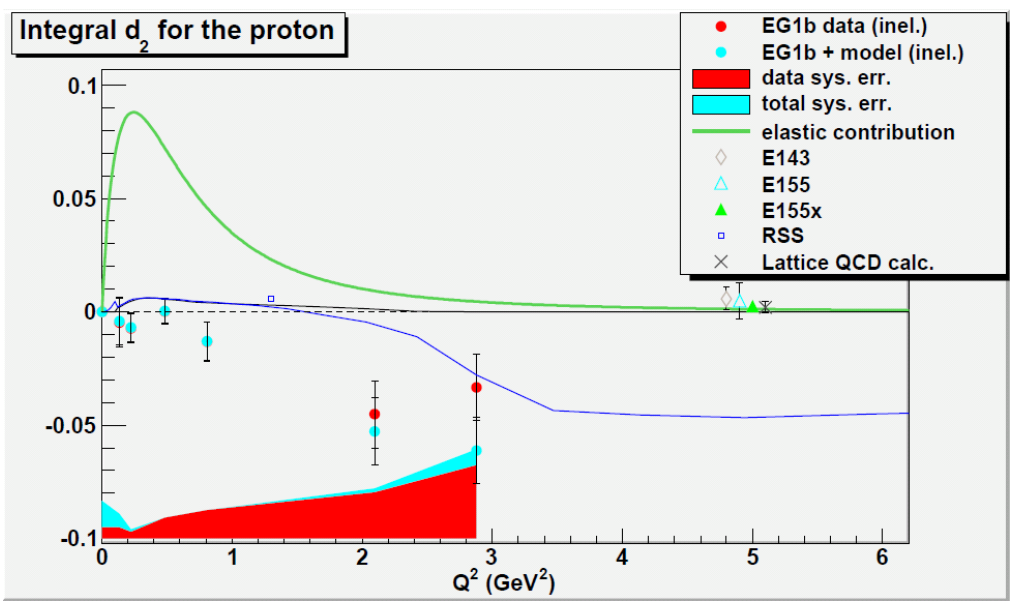

Figure 4.14: CLAS $d_2(Q^2)$ measured by indirect way [23]. Solid circles are d_2 from CLAS data, with systematic error band below.

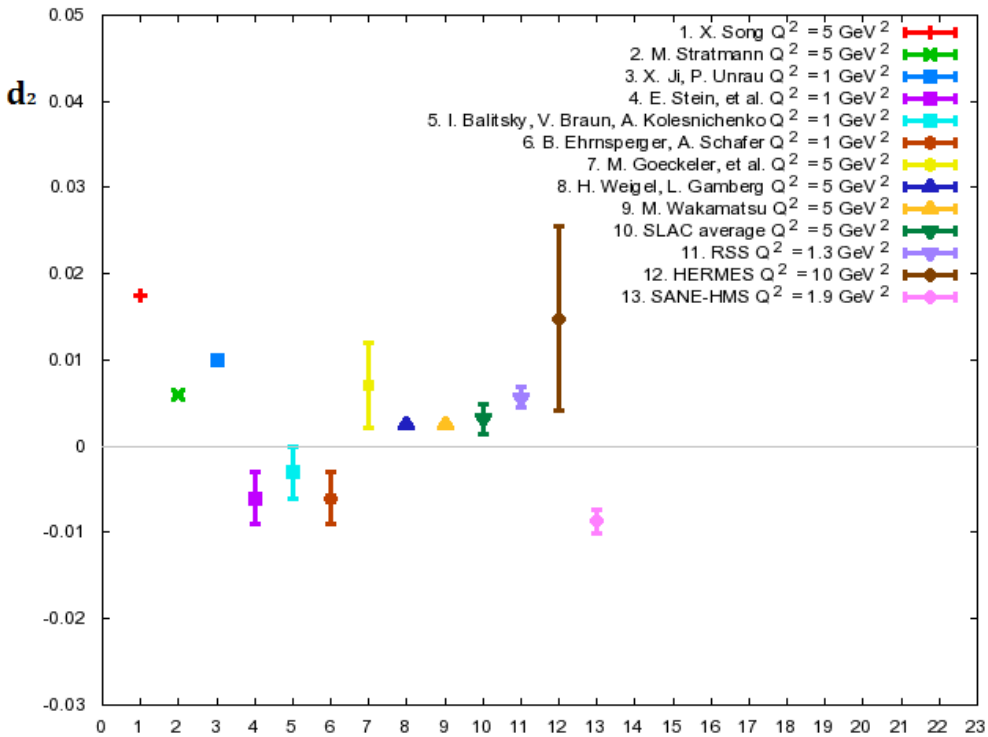

Figure 4.15: List of d_2 theories and experiments, same as Fig. 1.7, with additional SANE-HMS $\bar{d_2}$.

Resulting d_2, even with huge error bar, is negative at $2GeV^2$. Our negative $\bar{d_2}$ is in this constraint. Thus, our negative d_2 shines light on this intermediate Q^2 region. And it should be examined by both theory and experiment in the future.

4.4 Summary

In summary, our result increases the available data on the proton spin structure, especially at resonance region with low Q^2. This new data fill an unexplored

region in the world data. Especially, A_2 and g_2 data show clear Q^2 evolution, comparing with RSS and SANE-BETA. Negative resonance in A_2 data needs to be examined by theory. It can be an indication of very negative transverse-longitudinal interference contribution at $W \approx 1.3GeV$. Higher twist effect appears at the low Q^2 of $1.9GeV^2$. Twist-3 d_2 matrix element is also obtained using fit evaluated at $Q^2 = 1.9GeV^2$, $\bar{d_2} = -0.0087 \pm 0.0014$ by integrating $0.47 \leq x \leq 0.87$. It is the first negative d_2 of proton from experiment.

Appendices

Appendix A

Asymmetry Extraction

The difference of cross sections of opposite spin directions is

$$\begin{aligned}\Delta\sigma &= \sum_{s'}\left[\frac{d^2\sigma}{d\Omega dE'}(k,s,P,S;k',s') - \frac{d^2\sigma}{d\Omega dE'}(k,s,P,-S;k',s')\right] \\ &= \frac{8m\alpha^2E'}{q^4E}\{[(q\cdot S)(q\cdot s)+Q^2(s\cdot S)]MG_1 \\ &+ Q^2[(s\cdot S)(P\cdot q)-(q\cdot S)(P\cdot s)]\frac{G_2}{M}\},\end{aligned} \tag{A.1}$$

where k^μ is the 4-momentum of the incoming electron, k'^μ is of the scattered, P^μ is the initial 4-momentum of the proton, S^μ is the initial covariant spin 4-vector of the proton, s^μ is of the incoming electron, and s'^μ is of the outgoing electron. Other definition is the same as ep scattering process in the Introduction. In this context G_1 and G_2 are the spin structure functions, where $G_1 = \frac{g_1}{M^2\nu}$ and $G_2 = \frac{g_2}{M\nu}$.

Fig. A.1 shows the target coordinate in the lab frame. The target is positioned at the origin, and the beam direction is defined to follow z-axis. The x-axis points at the BigCal side, i.e. the beam left, therefore HMS is in the opposite side. This detector direction can be controlled by ϕ. Actually, HMS *phi*

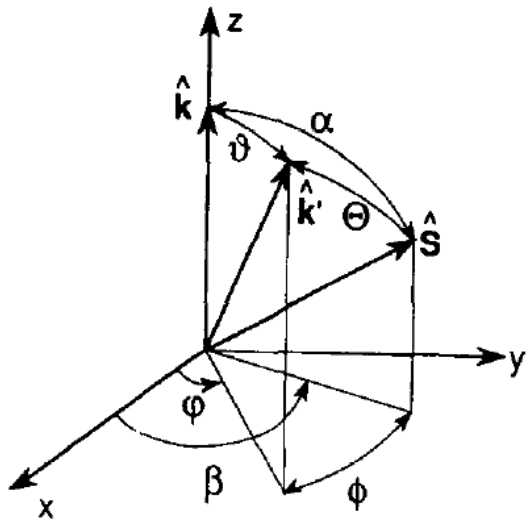

Figure A.1: Coordinate system of the target [24]

is defined already in this manner, i.e. *phi* 180°. After some algebra, following Ref. [24],

$$\Delta\sigma = \frac{-4\alpha^2 E'}{Q^2 E}\left[(E\cos\alpha + E'\cos\Theta)MG_1 + 2EE'(\cos\Theta - \cos\alpha)G_2\right]. \quad \text{(A.2)}$$

As $\cos\Theta$ is obtained by other angles like

$$\cos\Theta = \sin\theta\sin\alpha\cos\phi - \beta + \cos\theta\cos\alpha, \quad \text{(A.3)}$$

the parallel setting, where target spin is directing 180° from the beam direction, has

$$\alpha = 180°, \beta = 0, \cos\Theta = -\cos\theta, \cos\alpha = -1. \quad \text{(A.4)}$$

So, $\Delta\sigma_{180}$, the parallel setting cross section difference of $\Delta\sigma$, is

$$\Delta\sigma_{180} = \frac{-4\alpha^2 E'_{180}}{Q^2_{180}E_{180}}[-(E_{180} + E'_{180}\cos\theta_{180})MG_1 + Q^2_{180}G_2], \quad \text{(A.5)}$$

where subscript 180 means the kinematic variable from the parallel setting. Likewise the near-pependicular setting, where target spin is directing 80° from the beam direction, has

$$\alpha = 80^\circ, \beta = 0, \cos\Theta = \sin\theta \sin 80^\circ \cos\phi + \cos\theta \cos 80^\circ, \cos\alpha = \cos 80^\circ. \quad \text{(A.6)}$$

$\Delta\sigma_{80}$, the near-perpendicular setting cross section difference of $\Delta\sigma$, is

$$\begin{aligned}\Delta\sigma_{80} = \frac{-4\alpha^2 E'_{180}}{Q^2_{180} E_{180}}[&(E_{80}\cos 80^\circ \\ &+ E'_{80}(\sin\theta_{80}\cos\phi_{80}\sin 80^\circ + \cos\theta_{80}\cos 80^\circ))MG_1 \\ &+ 2E_{80}E'_{80}(\sin\theta_{80}\cos\phi_{80}\sin 80^\circ \\ &+ \cos\theta_{80}\cos 80^\circ - \cos 80^\circ)G_2],\end{aligned} \quad \text{(A.7)}$$

where subscript 180 means the kinematic variable from the near-perpendicular setting. These cross section difference is divided by two times of the unpolarized cross section, which is

$$\sigma^{unpol.} \equiv \frac{d^2\sigma^{unpol.}}{d\Omega dE'} = \frac{2\alpha^2 E'}{Q^2 E}\frac{F_1}{MD'}, \quad \text{(A.8)}$$

where $D' = \frac{1-\epsilon}{1+\epsilon R}$ as ϵ defined in Eq. (1.19), while F_1 and R are unpolarized structure functions, to get the asymmetries.

The kinematics of parallel and near-perpendicular asymmetries are different for SANE HMS resonance region, though their W, Q^2, x_{Bj}, and ν are almost same, with maximum offset of each W bin is 3%. So relation between (A_{180}, A_{80}) and (g_1, g_2) and also (A_1, A_2) should be carefully examined. First, (A_{180}, A_{80}) and (g_1, g_2) have the following relation:

$$A_{180} = \frac{-D'_{180}}{F_{1,180}}[-\frac{E_{180} + E'_{180}\cos\theta_{180}}{E_{180} - E'_{180}}g_1 + \frac{Q^2_{180}}{(E_{180} - E'_{180})^2}g_2], \quad \text{(A.9)}$$

$$\begin{aligned}A_{80} = \frac{-D'_{80}}{F_{1,80}}[&-\frac{E_{80}\cos 80^\circ + E'_{80}(\sin\theta_{80}\cos\phi_{80}\sin 80^\circ + \cos\theta_{80}\cos 80^\circ)}{E_{80} - E'_{80}}g_1 \\ &+ \frac{2E_{80}E'_{80}(\sin\theta_{80}\cos\phi_{80}\sin 80^\circ + \cos\theta_{80}\cos 80^\circ - \cos 80^\circ)}{(E_{80} - E'_{80})^2}g_2].\end{aligned} \quad \text{(A.10)}$$

Second, (g_1, g_2) and (A_1, A_2), with average F_1 and γ, have the following:

$$g_1 = \frac{F_1}{1+\gamma^2}(A_1 + \gamma A_2), \tag{A.11}$$

$$g_2 = \frac{F_1}{1+\gamma^2}(-A_1 + \frac{A_2}{\gamma}) \tag{A.12}$$

Above equations can be inverted as 2x2 matrices to get reverse relation. But the usual relation between (A_{180}, A_{80}) and (A_1, A_2) becomes ambiguous. So, it is not good to use the following:

$$A_{\parallel} = D(A_1 + \eta A_2), \tag{A.13}$$

$$A_{\perp} = d(A_2 - \zeta A_1), \tag{A.14}$$

though they are usual formulae when the kinematics are completely same. Instead we can use the new relations keeping track of variable of each setting. All the calculation followed it, and the errors were propagated using it.

Appendix B

Fitting Functions

To do radiative correction, fitting of the asymmetries is necessary. Our fits of A_1 and A_2 consist of Breit-Wigner (BW) functions for peaks and deep inelastic tail. Basic idea and formulae came from Ref. [70]. Due to our limited kinematics range, it is almost impossible to constrain the deep inelastic tail using only SANE-HMS resonance data. So, the function of this part followed RSS fit [5] (Appendix in arXiv:nucl-ex/0608003), because it has close Q^2 and it contains A_2 fit also.

$$A_1 = \sum_{i=1}^{3} BW_i + x^{\alpha} \sum_{n=0}^{3} \beta_n x^n, \tag{B.1}$$

$$A_2 = \sum_{i=1}^{2} BW_i + x^{\alpha} \sum_{n=0}^{3} \beta_n x^n \frac{1}{\sqrt{Q^2}}. \tag{B.2}$$

where $\alpha = 0.031, \beta_0 = 0.186, \beta_1 = -0.032, \beta_2 = -0.393, \beta_3 = 0.957$ for A_1 and $\alpha = 0.458, \beta_0 = 0.100, \beta_1 = 0.094, \beta_2 = -0.119, \beta_3 = -0.957$ for A_2.

The Breit-Wigner resonance BW_i is

$$BW_i = \frac{a_i \kappa_i^2 \omega_i^2 \Gamma_i \Gamma_i^{\gamma}}{\kappa_{cm}^2 [(\omega_i^2 - W^2)^2 + \omega_i^2 \Gamma_i^2]}, \tag{B.3}$$

where

$$\Gamma_i = g_i \left(\frac{q_{cm}}{q_i} \right)^{(2l_i+1)} \left(\frac{q_i^2 + X_i^2}{q_{cm}^2 + X_i^2} \right)^{l_i} \tag{B.4}$$

$$\Gamma_i^\gamma = g_i \left(\frac{\kappa_{cm}}{\kappa_i} \right)^{(2j_i)} \left(\frac{\kappa_i^2 + X_i^2}{\kappa_{cm}^2 + X_i^2} \right)^{j_i}, \tag{B.5}$$

and

$$\kappa_i = \sqrt{\frac{(\omega_i^2 + M^2 + Q^2)^2}{4\omega_i^2} - M^2} \tag{B.6}$$

$$q_i = \sqrt{\frac{(\omega_i^2 + M^2 - m_\pi^2)^2}{4\omega_i^2} - M^2} \tag{B.7}$$

$$\kappa_{cm} = \sqrt{\frac{(W^2 + M^2 + Q^2)^2}{4W^2} - M^2} \tag{B.8}$$

$$q_{cm} = \sqrt{\frac{(W^2 + M^2 - m_\pi^2)^2}{4W^2} - M^2}. \tag{B.9}$$

X_i, l_i, and j_i is the same as Ref. [70]. In these BW resonances, a_i's are the amplitude, ω_i's are centroid, and g_i's are width of the peak. Optimal number of peak was three for A_1 and two for A_2, though A_2 had Δ resonance peak centroid fixed.

Appendix C

Data Tables

In the data tables, W is in the unit of GeV, and Q^2 is GeV^2. *stat* means statistical error and *syst* systematic error. Sometimes the first bin ($W \approx 1.095(GeV)$) was ignored in the plots of this thesis, due to the huge error bar.

Table C.1: Unpolarized structure functions used [25].

W	Q^2	x	F_1	F_2	R
1.096	2.048	0.865	0.0028	0.0025	0.1528
1.126	2.021	0.840	0.0137	0.0119	0.1536
1.156	1.990	0.814	0.0380	0.0328	0.1540
1.186	1.963	0.790	0.0806	0.0693	0.1535
1.215	1.942	0.766	0.1118	0.0955	0.1510
1.245	1.926	0.743	0.1041	0.0883	0.1466
1.275	1.912	0.720	0.0907	0.0764	0.1437
1.305	1.898	0.698	0.0877	0.0736	0.1453
1.335	1.884	0.677	0.0919	0.0771	0.1504
1.365	1.869	0.656	0.0994	0.0834	0.1572
1.395	1.854	0.636	0.1091	0.0916	0.1668
1.425	1.837	0.616	0.1242	0.1048	0.1840
1.455	1.819	0.596	0.1538	0.1320	0.2159
1.485	1.797	0.576	0.2110	0.1852	0.2578
1.515	1.776	0.557	0.2307	0.2009	0.2627
1.545	1.752	0.538	0.2030	0.1699	0.2310
1.575	1.718	0.518	0.1980	0.1606	0.2145
1.605	1.673	0.497	0.2143	0.1706	0.2172
1.634	1.624	0.476	0.2500	0.1969	0.2341

Table C.2: Parallel asymmetry A_{180} and near-perpendicular asymmetry A_{80} after all corrections applied.

W	Q^2	x	$A_{180} \pm stat \pm syst$	$A_{80} \pm stat \pm syst$
1.096	2.048	0.865	0.324 ± 1.5388 ± 0.0466	-0.171 ± 1.5538 ± 0.0348
1.126	2.021	0.840	0.011 ± 0.2815 ± 0.0077	-0.229 ± 0.3208 ± 0.0136
1.156	1.990	0.814	0.018 ± 0.0951 ± 0.0069	-0.247 ± 0.1254 ± 0.0198
1.186	1.963	0.790	-0.039 ± 0.0489 ± 0.0087	0.055 ± 0.0695 ± 0.0077
1.215	1.942	0.766	0.030 ± 0.0383 ± 0.0147	-0.130 ± 0.0514 ± 0.0145
1.245	1.926	0.743	0.003 ± 0.0359 ± 0.0073	-0.055 ± 0.0565 ± 0.0064
1.275	1.912	0.720	0.012 ± 0.0394 ± 0.0084	-0.088 ± 0.0587 ± 0.0081
1.305	1.898	0.698	0.038 ± 0.0401 ± 0.0207	-0.171 ± 0.0611 ± 0.0201
1.335	1.884	0.677	0.084 ± 0.0401 ± 0.0160	-0.182 ± 0.0574 ± 0.0155
1.365	1.869	0.656	0.262 ± 0.0368 ± 0.0194	-0.256 ± 0.0575 ± 0.0160
1.395	1.854	0.636	0.252 ± 0.0372 ± 0.0160	-0.268 ± 0.0573 ± 0.0162
1.425	1.837	0.616	0.228 ± 0.0334 ± 0.0140	-0.117 ± 0.0512 ± 0.0086
1.455	1.819	0.596	0.246 ± 0.0287 ± 0.0127	-0.181 ± 0.0461 ± 0.0094
1.485	1.797	0.576	0.279 ± 0.0241 ± 0.0275	-0.118 ± 0.0365 ± 0.0120
1.515	1.776	0.557	0.320 ± 0.0221 ± 0.0172	-0.197 ± 0.0347 ± 0.0107
1.545	1.752	0.538	0.365 ± 0.0233 ± 0.0197	-0.157 ± 0.0383 ± 0.0093
1.575	1.718	0.518	0.293 ± 0.0255 ± 0.0136	-0.135 ± 0.0421 ± 0.0066
1.605	1.673	0.497	0.240 ± 0.0277 ± 0.0121	-0.054 ± 0.0399 ± 0.0035
1.634	1.624	0.476	0.269 ± 0.0288 ± 0.0151	-0.096 ± 0.0451 ± 0.0063

Table C.3: Virtual photon absorption asymmetries A_1 and A_2 after all corrections applied.

W	Q^2	x	$A_1 \pm stat \pm syst$	$A_2 \pm stat \pm syst$
1.096	2.048	0.865	0.889 ± 4.8738 ± 0.1214	0.178 ± 4.7040 ± 0.1214
1.126	2.021	0.840	0.509 ± 0.9630 ± 0.0377	-0.612 ± 0.9272 ± 0.0352
1.156	1.990	0.814	0.544 ± 0.3581 ± 0.0514	-0.640 ± 0.3452 ± 0.0481
1.186	1.963	0.790	-0.176 ± 0.1917 ± 0.0245	0.070 ± 0.1865 ± 0.0244
1.215	1.942	0.766	0.305 ± 0.1408 ± 0.0437	-0.291 ± 0.1389 ± 0.0434
1.245	1.926	0.743	0.109 ± 0.1464 ± 0.0199	-0.141 ± 0.1460 ± 0.0199
1.275	1.912	0.720	0.180 ± 0.1501 ± 0.0238	-0.209 ± 0.1519 ± 0.0239
1.305	1.898	0.698	0.366 ± 0.1525 ± 0.0580	-0.381 ± 0.1566 ± 0.0585
1.335	1.884	0.677	0.454 ± 0.1429 ± 0.0442	-0.328 ± 0.1483 ± 0.0448
1.365	1.869	0.656	0.876 ± 0.1379 ± 0.0489	-0.210 ± 0.1459 ± 0.0489
1.395	1.854	0.636	0.871 ± 0.1356 ± 0.0444	-0.268 ± 0.1454 ± 0.0456
1.425	1.837	0.616	0.588 ± 0.1204 ± 0.0315	0.081 ± 0.1309 ± 0.0301
1.455	1.819	0.596	0.726 ± 0.1071 ± 0.0308	-0.065 ± 0.1187 ± 0.0302
1.485	1.797	0.576	0.704 ± 0.0871 ± 0.0595	0.153 ± 0.0971 ± 0.0529
1.515	1.776	0.557	0.891 ± 0.0804 ± 0.0399	-0.004 ± 0.0915 ± 0.0374
1.545	1.752	0.538	0.886 ± 0.0838 ± 0.0417	0.162 ± 0.0974 ± 0.0365
1.575	1.718	0.518	0.709 ± 0.0889 ± 0.0284	0.099 ± 0.1050 ± 0.0247
1.605	1.673	0.497	0.506 ± 0.0870 ± 0.0240	0.221 ± 0.1011 ± 0.0187
1.634	1.624	0.476	0.620 ± 0.0951 ± 0.0313	0.149 ± 0.1143 ± 0.0255

Table C.4: Spin structure functions g_1 and g_2 after all corrections applied.

W	Q^2	x	$g_1 \pm stat \pm syst$	$g_2 \pm stat \pm syst$
1.096	2.048	0.865	0.001 ± 0.0089 ± 0.0002	-0.001 ± 0.0079 ± 0.0002
1.126	2.021	0.840	-0.001 ± 0.0086 ± 0.0002	-0.007 ± 0.0078 ± 0.0004
1.156	1.990	0.814	-0.003 ± 0.0090 ± 0.0006	-0.020 ± 0.0084 ± 0.0016
1.186	1.963	0.790	-0.004 ± 0.0105 ± 0.0013	0.009 ± 0.0099 ± 0.0013
1.215	1.942	0.766	0.000 ± 0.0109 ± 0.0030	-0.032 ± 0.0106 ± 0.0036
1.245	1.926	0.743	-0.002 ± 0.0107 ± 0.0014	-0.013 ± 0.0107 ± 0.0015
1.275	1.912	0.720	-0.001 ± 0.0098 ± 0.0014	-0.018 ± 0.0100 ± 0.0017
1.305	1.898	0.698	0.000 ± 0.0098 ± 0.0034	-0.035 ± 0.0103 ± 0.0042
1.335	1.884	0.677	0.007 ± 0.0098 ± 0.0028	-0.040 ± 0.0106 ± 0.0035
1.365	1.869	0.656	0.038 ± 0.0105 ± 0.0036	-0.061 ± 0.0117 ± 0.0040
1.395	1.854	0.636	0.039 ± 0.0115 ± 0.0033	-0.073 ± 0.0132 ± 0.0046
1.425	1.837	0.616	0.047 ± 0.0118 ± 0.0033	-0.035 ± 0.0140 ± 0.0029
1.455	1.819	0.596	0.061 ± 0.0133 ± 0.0038	-0.073 ± 0.0163 ± 0.0041
1.485	1.797	0.576	0.106 ± 0.0150 ± 0.0115	-0.066 ± 0.0190 ± 0.0076
1.515	1.776	0.557	0.127 ± 0.0154 ± 0.0079	-0.128 ± 0.0202 ± 0.0076
1.545	1.752	0.538	0.130 ± 0.0144 ± 0.0077	-0.086 ± 0.0196 ± 0.0059
1.575	1.718	0.518	0.100 ± 0.0151 ± 0.0052	-0.074 ± 0.0213 ± 0.0041
1.605	1.673	0.497	0.094 ± 0.0160 ± 0.0050	-0.028 ± 0.0232 ± 0.0025
1.634	1.624	0.476	0.121 ± 0.0208 ± 0.0074	-0.068 ± 0.0316 ± 0.0054

Table C.5: A_1 and A_2 before and after radiative correction(r.c.).

W	Q^2	x	$A_1 \pm stat$ before r.c.	$A_1 \pm stat$ after r.c.	$A_2 \pm stat$ before r.c.	$A_2 \pm stat$ after r.c.
1.096	2.048	0.865	5.629 ± 2.3803	0.889 ± 4.8738	4.049 ± 2.3057	0.178 ± 4.7040
1.126	2.021	0.840	0.926 ± 0.5023	0.509 ± 0.9630	-0.270 ± 0.4849	-0.612 ± 0.9272
1.156	1.990	0.814	0.557 ± 0.1944	0.544 ± 0.3581	-0.332 ± 0.1878	-0.640 ± 0.3452
1.186	1.963	0.790	0.030 ± 0.1080	-0.176 ± 0.1917	0.146 ± 0.1052	0.070 ± 0.1865
1.215	1.942	0.766	0.224 ± 0.0854	0.305 ± 0.1408	-0.096 ± 0.0843	-0.291 ± 0.1389
1.245	1.926	0.743	0.094 ± 0.0990	0.109 ± 0.1464	-0.018 ± 0.0988	-0.141 ± 0.1460
1.275	1.912	0.720	0.164 ± 0.1107	0.180 ± 0.1501	-0.097 ± 0.1119	-0.209 ± 0.1519
1.305	1.898	0.698	0.321 ± 0.1163	0.366 ± 0.1525	-0.170 ± 0.1193	-0.381 ± 0.1566
1.335	1.884	0.677	0.360 ± 0.1099	0.454 ± 0.1429	-0.156 ± 0.1138	-0.328 ± 0.1483
1.365	1.869	0.656	0.582 ± 0.1063	0.876 ± 0.1379	-0.143 ± 0.1122	-0.210 ± 0.1459
1.395	1.854	0.636	0.642 ± 0.1048	0.871 ± 0.1356	-0.197 ± 0.1120	-0.268 ± 0.1454
1.425	1.837	0.616	0.489 ± 0.0922	0.588 ± 0.1204	0.088 ± 0.0999	0.081 ± 0.1309
1.455	1.819	0.596	0.562 ± 0.0794	0.726 ± 0.1071	-0.030 ± 0.0876	-0.065 ± 0.1187
1.485	1.797	0.576	0.491 ± 0.0618	0.704 ± 0.0871	0.133 ± 0.0686	0.153 ± 0.0971
1.515	1.776	0.557	0.646 ± 0.0600	0.891 ± 0.0804	0.025 ± 0.0679	-0.004 ± 0.0915
1.545	1.752	0.538	0.726 ± 0.0693	0.886 ± 0.0838	0.175 ± 0.0801	0.162 ± 0.0974
1.575	1.718	0.518	0.633 ± 0.0764	0.709 ± 0.0889	0.121 ± 0.0896	0.099 ± 0.1050
1.605	1.673	0.497	0.482 ± 0.0747	0.506 ± 0.0870	0.226 ± 0.0861	0.221 ± 0.1011
1.634	1.624	0.476	0.590 ± 0.0796	0.620 ± 0.0951	0.158 ± 0.0948	0.149 ± 0.1143

Bibliography

[1] S. Kuhn, J.-P. Chen, and E. Leader, Prog. Part .Nucl. Phys. **63**, 1 (2009), arXiv:0812.3535 [hep-ph] .

[2] J. Beringer *et al.* (Particle Data Group), Phys.Rev. **D86**, 010001 (2012).

[3] P. L. Anthony *et al.* (E155 Collaboration), Phys. Lett. B **553**, 18 (2003).

[4] M. Stratmann, Zeitschrift für Physik C Particles and Fields **60**, 763 (1993).

[5] F. R. Wesselmann *et al.* (RSS Collaboration), Phys. Rev. Lett. **98**, 132003 (2007).

[6] X. Song, Phys. Rev. D **54**, 1955 (1996).

[7] X. Ji and P. Unrau, Phys. Lett. B **333**, 228 (1994), hep-ph/9308263 .

[8] E. Stein, P. Górnicki, L. Mankiewicz, A. Schäfer, and W. Greiner, Phys. Lett. B **343**, 369 (1995).

[9] I. Balitsky, V. Braun, and A. Kolesnichenko, Phys. Lett. B **242**, 245 (1990).

[10] B. Ehrnsperger and A. Schäfer, Phys. Rev. D **52**, 2709 (1995).

[11] M. Göckeler, R. Horsley, W. Kürzinger, H. Oelrich, D. Pleiter, P. E. L. Rakow, A. Schäfer, and G. Schierholz, Phys. Rev. D **63**, 074506 (2001).

[12] H. Weigel and L. Gamberg, Nucl. Phys. A **680**, 48 (2001), quark Nuclear Physics 2000.

[13] M. Wakamatsu, Phys. Lett. B **487**, 118 (2000).

[14] A. Airapetian *et al.*, Eur. Phys. J. C **72**, 1921 (2012).

[15] J. Jourdan *et al.*, *Update to TJNAF E-03-109: Spin Asymmetries on the Nucleon Experiment-SANE*, Tech. Rep. (2006).

[16] C. Leemann, D. Douglas, and G. Krafft, Annu. Rev. Nucl. Part. Sci. **51**, 413 (2001).

[17] J. D. Maxwell, *Probing proton spin structure: a measurement of g_2 at four-momentum transfer of 2 to 6 GeV^2*, Ph.D. thesis, University of Virginia (2011).

[18] Jefferson Lab, "Jefferson lab," (2014).

[19] A. Liyanage, *Proton form factor ratio, $\mu_p G_E^P/G_M^P$ from double spin asymmtry*, Ph.D. thesis, Hampton University (2013).

[20] K. V. Dharmawardane *et al.* (CLAS Collaboration), Phys. Lett. B **641**, 11 (2006).

[21] F. Lee, T. Mart, C. Bennhold, and L. Wright, Nucl. Phys. **A695**, 237 (2001), arXiv:nucl-th/9907119 .

[22] Y. Goto *et al.* (Asymmetry Analysis Collaboration), Phys. Rev. D **62**, 034017 (2000).

[23] R. G. J. Fersch, *Measurement of Inclusive Proton Double-Spin Asymmetries and Polarized Structure Functions*, Ph.D. thesis, The College of William and Mary (2008).

[24] M. Anselmino, M. Boglione, and F. Murgia, Phys. Lett. B **362**, 164 (1995).

[25] P. E. Bosted and M. E. Christy, Phys. Rev. C **77**, 065206 (2008).

[26] J. Ashman *et al.* (EMC Collaboration), Phys. Lett. B **206**, 364 (1988).

[27] K. Abe *et al.* (E143 Collaboration), Phys. Rev. D **58**, 112003 (1998).

[28] E. S. Ageev *et al.* (COMPASS Collaboration), Phys. Lett. B **612**, 154 (2005).

[29] K. Ackerstaff *et al.* (HERMES Collaboration), Phys. Lett. B **404**, 383 (1997).

[30] J. Soffer and O. V. Teryaev, (1999), hep-ph/9906455 .

[31] R. L. Jaffe and X. Ji, Phys. Rev. D **43**, 724 (1991).

[32] R. Feynman, *Photon-hadron Interactions*, Advanced Book Program Series (Addison-Wesley, 1998).

[33] R. L. Jaffe, (1996), hep-ph/9602236 .

[34] S. Wandzura and F. Wilczek, Phys. Lett. B **72**, 195 (1977).

[35] H. Burkhardt and W. Cottingham, Ann. of Phys. **56**, 453 (1970).

[36] L. Mankiewicz and Z. Ryzak, Phys. Rev. D **43**, 733 (1991).

[37] B. Ehrnsperger, L. Mankiewicz, and A. Schäfer, Phys. Lett. B **323**, 439 (1994), hep-ph/9311285 .

[38] R. Robert, *The Structure of the Proton* (Cambridge University Press, 1990).

[39] Leader, *Spin in Particle Physics* (Cambridge University Press, 2001).

[40] A. Hosaka and H. Toki, *Quark, Baryons and Chiral Symmetry* (World Scientific, 2001).

[41] A. Thomas and W. Weise, *The Structure of the Nucleon* (Wiley-VCH, 2001).

[42] N. Isgur, Phys. Rev. D **59**, 034013 (1999), hep-ph/9809255 .

[43] A. Thomas, Prog. Part. Nucl. Phys. **61**, 219 (2008).

[44] S. J. Brodsky, M. Burkardt, and I. Schmidt, Nucl. Phys. B **441**, 197 (1995), hep-ph/9401328 .

[45] P. L. Anthony *et al.* (E155 Collaboration), Phys. Lett. B **458**, 529 (1999).

[46] J. Kodaira, S. Matsuda, K. Sasaki, and T. Uematsu, Nucl. Phys. B **159**, 99 (1979).

[47] R. Jaffe, Comments Nucl. Part. Phys. **19**, 239 (1990).

[48] K. Slifer *et al.* (RSS Collaboration), Phys. Rev. Lett. **105**, 101601 (2010).

[49] C. Hernandez-Garcia, M. L. Stutzman, and P. G. O'Shea, Physics Today **61**, 44 (2008).

[50] S. R. Mane, Y. M. Shatunov, and K. Yokoya, Rep. Prog. Phys. **68**, 1997 (2005).

[51] C. Yan and R. Carlini, AIP Conf. Proc. **269**, 571 (1992).

[52] P. Gueye, *Status of the actual beam position monitors in the Hall C beamline*, Tech. Rep. (Jefferson Lab, 1995).

[53] J. R. L. Mulholland, *SANE's measurement of the proton's virtual photon spin asymmtry, A_1^p at large Bjorken x*, Ph.D. thesis, University of Virginia (2012).

[54] K. B. Unser, AIP Conf. Proc. **252**, 266 (1992).

[55] C. Yan *et al.*, Nucl. Inst. Meth. Phys. Res. Sec. A **365**, 261 (1995).

[56] C. Yan, R. Carlini, and D. Neuffer, "Beam energy measurement using the arc beam line as a spectrometer," (1993), prepared for 1993 IEEE Particle Accelerator Conference (PAC 93).

[57] M. Hauger *et al.*, Nucl. Instrum. Meth. **A462**, 382 (2001), arXiv:nucl-ex/9910013 [nucl-ex] .

[58] J. M. Grames *et al.*, Phys. Rev. ST Accel. Beams **7**, 042802 (2004).

[59] D. Crabb and D. Day, Nucl. Instrum. Methods Phys. Res. Sect. A **356**, 9 (1995).

[60] J. Cobb and J. Muray, Nuclear Instruments and Methods **46**, 99 (1967).

[61] M. Berz, *COSY Infinity Version 7 Reference Manual*, Tech. Rep. (Michigan State University, 1995).

[62] O. Baker *et al.*, Nucl. Inst. Meth. Phys. Res. Sec. A **367**, 92 (1995), proceedings of the 7th International Wire Chamber Conference.

[63] J. Arrington, *Inclusive Electron Scattering From Nuclei at $x > 1$ and High Q^2*, Ph.D. thesis, California Institute of Technology (1998).

[64] C. E. B. A. Facility, *CODA - CEBAF On-line Data Acquisition User's Manual*, 1st ed. (1995).

[65] O. Couet, *PAW (Physics Analysis Workstation) Users Guide*, CERN (2001).

[66] O. A. Rondón, *The Packing Fraction and Dilution Factor in RSS*, Tech. Rep. (2006).

[67] S. Kulagin and R. Petti, Nucl. Phys. A **765**, 126 (2006).

[68] O. A. Rondón, Phys. Rev. C **60**, 035201 (1999).

[69] I. Akushevich, A. Ilyichev, N. Shumeiko, A. Soroko, and A. Tolkachev, Acta Phys. Polon. B **28**, 563 (1997).

[70] S. Stein *et al.*, Phys. Rev. D **12**, 1884 (1975).

[71] F. James, *MINUIT Function Minimization and Error Analysis Version 94.1* (2000).

[72] D. Drechsel, O. Hanstein, S. Kamalov, and L. Tiator, Nucl. Phys. A **645**, 145 (1999).

[73] H. Y. Lu *et al.* (CLAS Collaboration), Phys. Rev. C **88**, 045202 (2013).

[74] M. Jones and O. A. Rondon, *The 15N correction to the measured asymmetries*, Tech. Rep. (TNJAF and INPP - UVA, 2011).

[75] M. E. Christy *et al.*, Phys. Rev. C **70**, 015206 (2004).

요약(국문초록)

양성자의 스핀 구조를 높은 브조르켄(Bjorken) x와 낮은 운동량 전달 Q^2 영역에서 탐구하였다. 우리는 제퍼슨 연구소의 편극된 전자 빔, 편극된 표적, 분석계를 사용하여 평행과 수직 스핀 비대칭성 $A_{\parallel}$과 $A_{\perp}$를 모두 구하였다. 이 비대칭성을 이용하여 물리적 비대칭성인 A_1과 A_2, 스핀 구조 함수 g_1과 g_2를 구하였다. 이를 통해 공명 영역에서 비대칭성의 Q^2 의존성과 높은 꼬임(twist) 효과를 발견하였다. 이 결과는 양성자 스핀 구조에 대한 새로운 데이터를 특히 낮은 Q^2의 공명 영역에서 제공한다. 게다가, RSS와 SANE-BETA 실험 결과와의 비교를 통해 볼 때, A_2와 g_2 데이터는 Q^2에 따른 중대한 변화를 보여준다. 일부 공명 영역에서 음수로 나온 A_2 데이터는 이론적으로 검토해야 할 필요가 있다. 이는 매우 강한 음의 방향으로의 수직-평행 간섭이 $W \approx 1.3$ GeV 근처에서 일어나고 있다는 암시일 수 있다. 비록 더 낮은 Q^2의 RSS 데이터에서보다는 덜 분명하지만, 높은 꼬임(twist) 효과가 1.9 GeV^2라는 낮은 Q^2에서 나타났다. 꼬임수(twist) 3의 행렬 요소 d_2도 우리의 비대칭성에 대한 적합함수를 $Q^2 = 1.9$ GeV^2에서 구함으로써 계산하였다. $0.47 \leq x \leq 0.87$ 사이에서 적분하여, $\overline{d_2} = -0.0087 \pm 0.0014$를 얻었다.

주요어 : 이중 스핀 비대칭성, 양성자 스핀 구조, 연산자 곱 전개, 핵자 공명, 전자-양성자 산란, 제퍼슨 연구소
학 번 : 2006-20313

Acknowledgement

I would like to express my deepest appreciation to my collaborators:
To SANE co-spokespersons, Professor Seonho Choi, Doctor Mark Jones, Professor Zein-Eddine Meziani, and Doctor Oscar A. Rondon, for their leadership in the collaboration and kind advices on the analysis,
To Doctor Narbe Kalantarians, Doctor Hovhannes Baghdasaryan, and Doctor Cornel Butuceanu, for their help and contribution on the experiment,
To Doctor James Maxwell, Doctor Jonathan Mulholland, Whitney Armstrong, Doctor Anusha Liyanage, and Luwani Z. Ndukum, for their friendship and wonderful work in both experiment and analysis.

Especially, it would have been impossible to finish this work, without SANE analysis meetings with Oscar and Mark. I owe them really much. And I thank Anusha for her great work on HMS system.

I also thank Professor Peter Bosted, Professor Mahbub Khandaker, and Professor Karl Slifer, for their kind feedback and comments.

I cannot thank enough to the members of SANE collaboration and Jefferson Lab Hall C collaboration for their great work. Jefferson Lab was a great place to study physics, every time I visited. It was my honor to research with Jefferson Lab staffs and users.

감사의 글

저의 인생을 인도하시는 하나님께 감사와 영광을 드립니다. 그 분은 이 모든 일의 시작(A)과 끝(Ω)이 되십니다.

부족한 제가 논문을 완성하기까지 지도하시고 도와주신 최선호 교수님께 감사드립니다. 좋은 실험을 할 수 있도록 도와주시고 끝까지 인내하며 저를 가르쳐주셨습니다. 바쁘신 중에 논문 심사를 맡아 주신 김수봉 교수님, 김형도 교수님, 양운기 교수님, 천명기 교수님께 감사드립니다. 세미나와 수업 시간에 많은 가르침을 주신 방형찬 교수님, 김선기 교수님, Tanida 교수님, Sato 교수님께도 감사드립니다. 물리천문학부 교수님들의 명강의는 제게 물리 하는 즐거움과 많은 깨달음을 주었습니다. 해외 실험과 학회 참석을 재정적으로 지원해 주신 BK21 사업단과 WCU 사업단에도 감사합니다.

연구와 대학원 생활 가운데 크고 작은 도움을 받은 분들이 많아 다 열거할 수 없습니다. 특별히, 김도균 박사님, 추경호 박사님, 이병욱 박사님, 류수 박사님, 오유민 박사님께 감사합니다. 혜구 형, 정석, 명진, 영록, 융희, 종원, 새한슬, 현우, 정수, 원국, 봉호 (박사님), 선지, 성배, 창우, 상화에게 감사합니다. 연구실 특성상 외국에 나가 있을 때가 많고 같이 연구를 할 기회가 적었지만, 좋은 연구실 선후배님들과 동료들이 많아서 항상 든든했습니다. 혜구 형, 유민이 형과 함께 JLab에서 함께 생활하며 같은 식탁에 둘러앉았던 추억은 오랫동안 기억날 것 같습니다. JLab에서 몇 명 안 되는 한국인이라고 친절하게 도와주신 박기준 박사님, 이정한 박사님, 신일경 박사님께도 감사드립니다. 또한 학부 시절 저의 무리한 프로젝트 구상에 함께 하다가 많이 당한 흥식이에게도 고마움을 전합니다(다시 한 번 결혼 축하한다).

항상 기도해주시며 도와주신 정아브라함, 은주 목자님, 인금철, 정훈 목자님, 한베드로, 수지 목자님께 깊이 감사합니다. 특별히 김이삭, 레베카 목자님께는 도저히 갚을 수 없는 사랑의 빚을 졌습니다. 두란노 요회의 종현 목자, 세웅 목자, 승대, 태진, 기영, 예인, 지인 형제자매님의 기도와 사랑에

감사합니다. 특별히 물리학부 후배이자 장차 고체물리를 이끌어 갈 정종현 목자에게 응원과 기도를 보냅니다. 부족한 저와 함께 성경 공부한 윤우, 한솔, 요셉 형제님들에게도 고마움의 마음을 전합니다. 저희 가정의 기쁨이 된 요안나, 지인 자매님에게도 감사합니다. 또한 MBF 형제자매들이 위대한 하나님의 사람으로 성장하기를 기도합니다. 같은 팀에서 동고동락한 바울, 요셉, 태용 목자님, 늘 좋은 친구가 되어 준 진우, 대경, 문수 목자님에게도 감사합니다. 관악5부 동역자님들의 기도 덕분에 무사히 졸업하게 되었습니다. I give my thanks to S. Chris and Christine Kelly, M. David and Dr. Sarah Won, Dr. Mark and Esther Yoo, and M. Samuel and Joy Kim, and their families. I also thank M. Wesley and Esther Yun, Dr. Abraham (Jr.) and Sarah Jeong, Dr. James and Mary Yoo, S. Don and M. Pauline Lipsey for their hospitality and love while visiting them.

큰아버지, 큰어머니, 둘째 큰아버지, 큰어머니, 이모부, 이모, 여러 친척 분들의 지원과 사랑에 감사드립니다. 못난 자식을 헌신적으로 사랑해주신 아버지, 어머니, 부족한 사위를 믿고 아껴주신 장인, 장모님께 말로 다 할 수 없는 감사를 드립니다. 처제와 처남, 동생 의영이도 늘 큰 힘이 되었습니다. 지금은 하늘나라에 있는 이정이 누나에게도 깊은 감사와 사랑을 전합니다.

제 인생 최고의 선물인 아내 혜란의 내조와 사랑에 깊이 감사합니다. 부족한 남편을 믿고 헌신적으로 사랑해준 아내에게 이 논문을 바칩니다.